Universitá degli Studi di Torino

DIPARTIMENTO DI FISICA

PhD thesis

Development of Resistive Silicon Detectors for 4D tracking

Author: Luca Menzio
Supervisor: Prof. Marco Costa
Supervisor: Dott. Nicoló Cartiglia

Academic Year: 2022 - 2023

Contents

Acknowledgements

This work would not have been possible without the help and support of the whole team of the UFSD project. In particular, I would like to express my gratitude to my supervisor Prof. Marco Costa for always saying the right words at the right time and for guiding me to walk the first steps as a scientist. Without his guidance and persistent help, this dissertation would not have been possible. The scientific mentorship of my supervisor Nicoló Cartiglia was fundamental in every step of my work on silicon devices. I am deeply grateful to having had the chance to pursue the development of new detectors with such an expert and kind mind. I would like to thank express my sincere gratitude for the counsel of Roberta Arcidiacono and her ability to introduce well thought deadlines to each step of my progress towards the realization of this thesis.
A special mention is owed to my colleagues Federico Siviero, Marta Tornago, Marco Ferrero, Giulia Gioachin, Leonardo Lanteri, Valentina Sola and Roberto Mulargia. They are capable of creating an ideal work environment, both creative and constructive. I must express my very profound gratitude to Sara for providing me with unfailing support and continuous encouragement throughout my years of study. This accomplishment would not have been possible without her. Another mention is due to all my friends who endured this stressful year with me. Now I'll come out of my isolation, I promise.

This work was supported by INFN - Gruppo V UFSD and RSD projects, INFN – FBK agreement on sensor production (convenzione INFN-FBK), Horizon 2020 grant UFSD669529, Dipartimenti di Eccellenza dell'Universiá di Torino, Ministero della Ricerca projects 2017L2XKTJ – 4DinSiDe and R165xr8frt_fare. The measurements reported in Sections 4.6 have been performed at the Test Beam Facility at DESY Hamburg (Germany), a member of the Helmholtz Association (HGF).

All the nice drawings at the beginning of the Chapters were made by Marta Tornago.

Introduction

The research in High-Energy Physics (HEP) relies on large-scale collider facilities and the operation of general-purpose experiments they are equipped with. Their tracking systems play a fundamental role in these experiments. Future facilities will be characterized by enhanced luminosity and higher particle energies. The urgency for trackers with even better position and time resolutions, high radiation hardness, very low material budget, and low power consumption is becoming increasingly evident. Pixelated or strip silicon detectors have been traditionally employed inside tracking systems, but their performances do not suffice for future accelerator facilities. Therefore, a paradigm shift is required to continue the scientific research conducted so far and to advance in the search for new physics and discoveries. With the advent of the Low-Gain Avalanche Diodes (LGAD) technology, measuring time precisely with silicon detectors down to some tens of picoseconds became possible. The Turin group has always played a central role in developing silicon devices able to measure time and recently proposed a new type of sensor: the Resistive Silicon Detector (RSD). Based on the LGAD technology, it is characterized by a moderate internal gain (10-20) combined with a resistive surface that allows charge sharing among adjacent pads, either AC- or DC-coupled to the read-out electronics. This design reduces the number of read-out channels without decreasing the performance levels; it has a 100 % fill factor and maintains the excellent time resolution german to LGADs.

The present thesis focuses on the experimental results obtained with the latest RSD production by Fondazione Bruno Kessler and it illustrates, from the perspective of future applications, the methods exploited to achieve excellent spatial and temporal resolution using a single silicon device. The first chapter introduces the concept of 4D-tracking and describes the requirements of future experiments, illustrating how state-of-the art silicon sensors cannot meet these requests. The second chapter contains an overview of the UFSD principle of operations, while a detailed description of the RSD design and productions can be found in Chapter 3. Chapter 4 reports the experimental techniques being employed to characterize the sensors. The fifth chapter describes the analysis methodology used to process the data acquired on the RSD2 production and presents the experimental results obtained. These measurements demonstrate the validity of the RSD design, resulting in a few micron space resolution and confirming the LGAD-like time resolution. Chapter 6 illustrates an innovative two-prong simulation, based on Spice and TCAD, that allows for much faster identification of the most promising sensor parameters. Such a method was applied to develop

the latest evolution of resistive silicon detectors: the DC-RSD. DC-RSD are based on charge-sharing sensors, as standard RSD, but use a DC-coupled read-out scheme. Chapter 7 presents an outlook on the DC-RSD production with a brief description of some of the technical challenges encountered while designing this new sensor batch. The second part of Chapter 7 summarizes the conclusions of this work.

Chapter 0

4D Tracking for Present and Future Facilities

A fundamental component of modern-day physics research relies on large-scale experiments that explore nature's rules. Among these, High-Energy Physics (HEP) facilities and general-purpose systems play a central role in exploring new processes and allowed probing of our understanding of elemental forces. The study of these properties relies on the analysis of particle interactions from the product of their collision at high energy. Outgoing particles are identified as they have emitted from the interaction vertex thanks to the interplay of different detectors. Such identification greatly relies on the measurement of particle location to a specified accuracy and the ability to deal with a specific rate of particle hits. In recent decades, the silicon sensor has become the ideal tool for making such measurements. Allowing a very high density of pixels with a relatively low manufacturing cost, it is present in all modern high-energy physics detectors [1]. With the advent of future high luminosity experiments, such as Compact Linear Collider (CLIC) [2, 3], Future Circular Collider (FCC) [4], and High Luminosity phase of the Large Hadron Collider (HL-LHC) upgrades [5], the need of timing information added to the more traditional 3D tracking has become evident. Hence, the necessity for 4D tracking detectors to whose development this thesis is dedicated.

This chapter highlights the motivations for 4D tracking devices development, their requirements and the possible solutions in terms of sensors.

0.1 Silicon Tracking Detectors in HEP

High-energy physics experiments probe the laws of physics with a range of different detectors, among which the tracker plays a central role. Tracking systems are composed of sensors with excellent spatial resolution and aim at reconstructing the trajectory of the impinging charged particles. To do so, they are usually placed as close to the interaction point as possible, and they should be thin in order not to alter the particle kinematics. Ultimately, the charged particle tracks are then reconstructed and used to extract the positions of the primary and secondary vertexes. The better the tracks are

measured, the smaller the uncertainty on the particles' moment σ_p. Since particles composed of heavy quarks have a very small lifetime, the ability of the tracker to localize secondary vertexes is vital. Its figure of merit is called impact parameter resolution σ_{d_0}, where d_0 is the minimum distance over which the primary and secondary vertexes can be disjointed. Both σ_p and σ_{d_0} depend on

1. The hit position resolution σ_{hit}, i.e. how precisely the impinging position is located on the sensor surface.

2. The multiple scattering position resolution σ_{MS}, namely the influence of the tracker material on its precision.

These two contribute to the precision with which the vertexes' positions are estimated, σ_{pos}. Only detectors with very small σ_{hit} and σ_{MS} can reach the performances required by the next generation of colliders (see Table 1).
These terms σ_{hit} and σ_{MS} highly depend on the type of architecture on which the system is based. On the one hand, **single pixel read-out** (represented in Figure 1 (A)) have hit a resolution equal to the standard deviation of a uniform random variable distributed over the pixel pitch $\sigma_{hit} = k \cdot pitch/\sqrt{12}$, where k $\sim$ 0.5-1. Therefore, the pixel dimension determines its spatial resolution. Pixels with lateral dimensions of 25x25 µm^2 are needed to obtain resolutions in the order of 5 µm, and it is practically impossible to achieve smaller pixels. Another approach consists in **multi-**

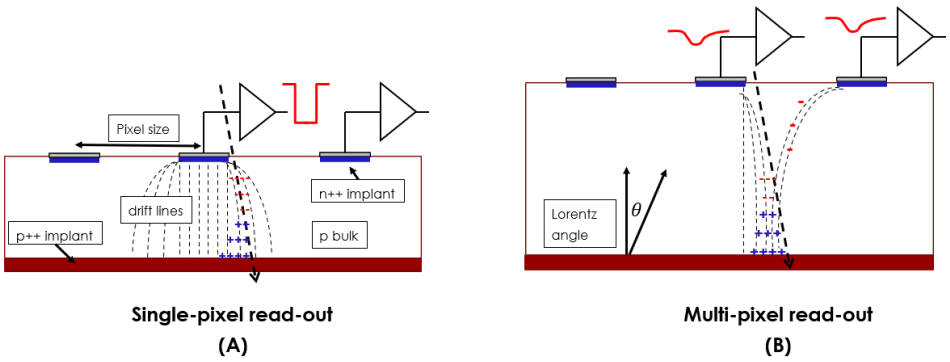

Figure 1: Single- (A) and Multi- (B) pixel read-out schemes for silicon sensors. When a magnetic field is present, the drift lines are modified by adding a Lorentz angle that induces charge sharing between two neighbouring pixels.

pixel read-out, where the signal is split between multiple pixels, and the position of a hit can be calculated using the centroids of the pixels coordinates (see Figure 1 (B)). However, sharing requires large signals to maintain the same efficiency level as a single-pixel sensor. This traditionally leads to thick sensors (200-300 µm) both to provide large-enough signals and to allow sufficient bending of the drift lines. For example, the Compact Muon Solenoid (CMS) collaboration at CERN has chosen a large multi-pixel read-out combined with a high magnetic field (100x150 µm ^{2} and 4 Tesla magnet, $\sigma_x \sim 5$ µm and $\sigma_y \sim 5$ µm) [6].

It is essential to notice how the two abovementioned parameters are strictly correlated: for example, the thickening of the sensors improves σ_{hit} while worsening σ_{MS}.

0.2 4D Tracking

The inclusion of timing information in a single collision has the ability to improve event reconstruction drastically. Points overlapping in a traditional tracking system (Figure 2, left) can be associated with hits that have a similar time stamp in the pattern recognition phase. On the other hand, the ones with a time difference above a certain threshold are discarded. This feature dramatically improves the reconstruction efficiency, bringing benefits to facilities where the instantaneous luminosity is particularly high. Depending on the collider type, sensors with different characteristics can be employed: from a dedicated timing layer in addition to a standard tracker to the timing information associated with each point of the track.

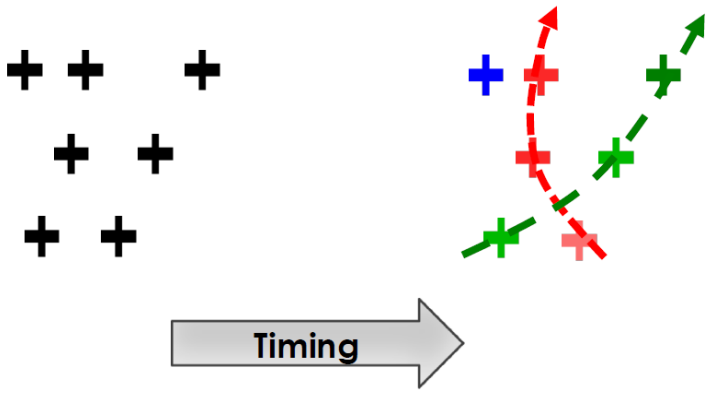

Figure 2: Representation of the improvement brought by 4D tracking in tracks reconstruction. On the left, ambiguous points with traditional 3D tracking. On the right, track points are associated using their timestamp (4D tracking).

Another option consists in associating time to just some points along the tracks. This solution would reduce the greater power consumption due to the electronics coupled with the sensors with timing information while maintaining the same level of precision. 4D tracking would also allow the separation of vertexes that would otherwise be indistinguishable. Figure 3 represents tracks that would be associated with the same collision event if timing information was not added.

0.3 Future Facilities

Essential to the development of a novel detector is the environment it will be placed into and the parameters they require. For this reason, the 2021 ECFA Detector R&D Roadmap [7] defines a list of facilities and areas towards which the research on detectors should be pointed. Some of the most relevant for this work are:

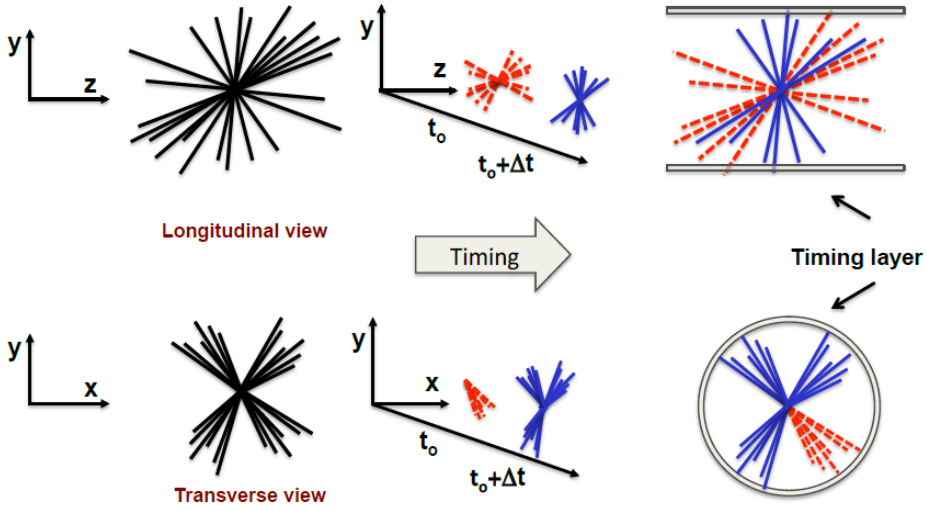

Figure 3: Intuitive depiction of the benefits brought by the addition of timing information to collision vertex reconstruction. Two different situations are reported: one consists of two distinct events with multiple outgoing tracks (*top*) and the second is based on a single shower of secondary particles that would be associated to another event. Both these examples are correctly resolved with the addition of the time information.

- High Luminosity LHC (HL-LHC)
- e^+e^- Higgs-EW-Top factories (CLIC)
- A future 100 TeV hadron collider (FCC)
- Muon colliders

It should be noted that one experiment has been reported for each experiment type since detector R&D is usually aligned for other possible facilities. For example, there are significant overlaps between the requirements for the proposed CEPC in China and FCC-ee and, in some cases, between ILC and CLIC. Approximate requirements are reported in Table 1.

Facility	σ_{pos} (µm)	σ_t (ps)	Power (mW/cm^2)	Si Thickness (µm)
HL-LHC	≤ 15	$\simeq 50$		
CLIC	≤ 3	$\simeq 5$	$\simeq 50$	$\simeq 100$
FCC-hh	$\simeq 7$	≤ 20		$\simeq 100$
FCC-ee	≤ 3	$\simeq 25$	$\simeq 20$	$\simeq 100$
Muon colliders	≤ 5	≤ 20		

Table 1: Selection of relevant requirements for the cited future experiments vertex detector. The last column (material budget) is reported as a percentage per layer. Quantities taken and adapted from the ECFA R&D Roadmap [7].

Requirements for these experiments set the target for detector R&D. Furthermore, the timeline of Figure 4 outlines approximate deadlines for

this process step. The High Luminosity upgrade at the Large Hadron Collider (HL-LHC) [5] is not included in this image. Two major general-purpose experiments, the CMS and ATLAS (A Toroidal LHC ApparatuS) collaborations at CERN, decided to equip their tracker with an additional timing detector given this upgrade. More information on this matter can be found in Section 0.5. Another parameter of central importance is the ratio between the sensor area able to measure the passage of a charged particle and the total surface, i.e. $fill\ factor = \frac{active\_area}{total\_area}$. For trackers, a typical minimum specification is a fill factor 95 %. Such requirement can be met with large pixels, while where the dimensions are smaller (some tens of µm), it becomes an additional challenge. Detectors in new hadron colliders like FCC-hh will face unprecedented radiation hardness. The highest levels are reached in the forward calorimeters where the total ionising dose and the 1-MeV equivalent neutron fluence rise to values of 5000 MGray and 5 $\cdot$ 10^{18} n_{eq} cm^{-2}. Even in the innermost layer of the barrel vertex detectors, the fluences approach 10^{18} neq cm^{-2} after an integrated luminosity of 30 ab^{-1}. Finally, the read-out electronics play another vital role and highly impact how much material is placed around the detector. The front end consumes energy and produces heat, so it needs service cables and cooling. In traditional silicon trackers, both are directly proportional to the number of pixels (or channels). This number is vast in traditional trackers and dramatically influences the multiple scattering. For this reason, in the previously mentioned Table 1 are reported the maximum power consumption and the maximum silicon thickness allowed.

Although research and development in tracking and timing sensors are very active in different fields [8], **currently no particle detector can achieve the performances listed in Table 1**.

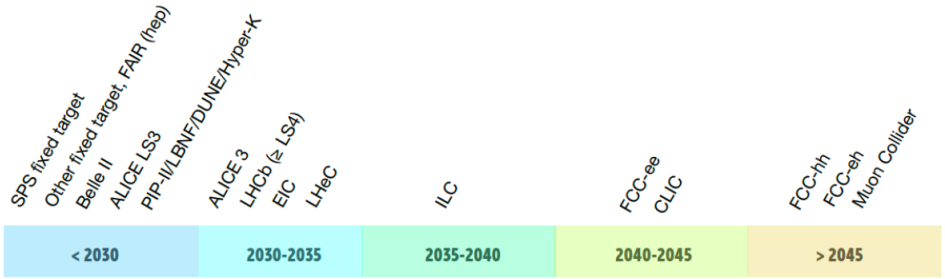

Figure 4: Large accelerator-based facility/experiment earliest feasible start dates. Image taken from [7].

0.4 Solid State sensors for 4D tracking

Solid State detectors (SSD) based on semiconductors, particularly silicon detectors, are used in almost all particle physics experiments. They provide superior position resolution, thanks to the fine segmentation obtained through commercially available lithographic processes at relatively low pro-

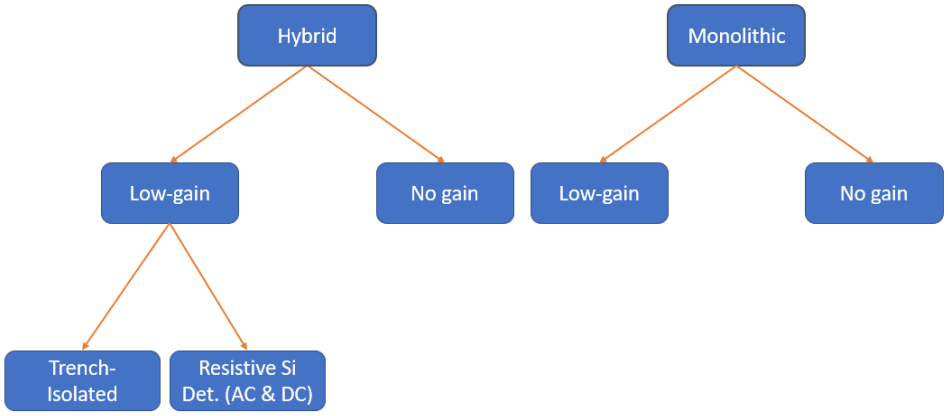

Figure 5: Scheme of a possible classification for the different types of silicon detectors capable of timing measurements.

duction costs.

Driven by the recent HEP challenging requirements, last two of decades saw an increasing interest in researching silicon devices capable of measuring both time and position in the same device with increasing precision. In this Section it is reported a very brief summary of the technology currently recognized as most promising in this rapidly expanding field. One can classify the different types of devices as a function of the output signal provided, either analog or digital. In the first category fall the devices coupled externally with electronics that processes the analog signals and produces digital outputs (*hybrid* detectors), while the second corresponds to devices with such electronics included in the same silicon die and are able to directly produce digital signals. As visible in Figure 5), among both these are found sensors which exploit intrinsic moderate gain to achieve a fast signal with large charge and the ones that adopt geometrical means or CMOS technology to increase the signal output charge.

0.4.1 Sensors with no internal gain

The timing resolution of standard planar silicon sensors with no internal gain is limited by their thickness, which causes the output signal amplitude to be small ($\sim$ 1.7 fC in 300 µm-thick devices). Since the peak signal current is not dependent on the sensor thickness (see Chapter 1), its rise time solely depends on the front-end electronics. Therefore, the timing characteristics of a system with no internal gain depend on the electronics slew rate and noise. To adapt to these conditions, both monolithic and hybrid systems were developed.

- *Monolithic Systems*
  Developed with CMOS and SiGe technologies, monolithic systems have proven to be capable of precise position reconstruction and moderately good time tagging capabilities. An example of a functioning device in this field is the CMOS 180 nm-based FASTpix chip [9], whose

demonstrator has proven to be able to achieve 120-180 ps time resolution in test beam campaigns on pixels with pitch spanning from 8.66 µm up to 20 µm. On the other hand, the MonPicoAD project [10] produced a monolithic detector exploiting the SiGe SG13G2 130 nm node technology, allowing to reduce the noise and increase the slew rate of the signal. The detector consists in a matrix of hexagonal pixels with a pitch of 100 µm and a power consumption of about 40 W/cm^2, with a measured time resolution of 35 ps.

- *Hybrid Systems*
  In the family of silicon devices with no gain, one can find planar sensors and 3D sensors with columns or trenches. In the first category falls the NA62 GigaTracker [11] coupled with the TDCPix ASIC, which achieves a single hit time resolution of 130 ps among 18000 pixels of 300x300 µm^2 area. Another very interesting type of hybrid system consists of 3D detectors coupled with their electronics. These sensors are known for their radiation resistance [12] and are currently used in the ATLAS inner pixel layer. Unlike traditional sensors, the 3D geometry of these sensors reduces local ionization fluctuation and allows for a very short drift time. While the standard implementation of 3D sensors degrades temporal resolution due to position-dependent signal shapes, recent modifications, such as using trenches instead of columns, have improved the uniformity of electric and weighting fields. For example, TimeSpot ASIC [13], designed for trenched 3D detectors, reaches a temporal resolution of about 30 ps with a power budget of 2–3 W/cm^2 over pixels with 50x50 µm^2 active area. The 3D geometry is also being explored in diamond detectors, which currently achieve a precision just below 100 ps and an efficiency larger than 99%.

0.4.2 Sensors with low internal gain

Another approach to silicon detectors for timing measurements consists of the Low-Gain Silicon Diode (LGAD) technology [14]. It is based on the multiplication of the charge produced by the passage of a particle through a high and localized electric field. Multiplying the signal amplifies the sensor noise to a greater extent than the signal amplitude. Nevertheless, due to the predominant influence of electronic noise on the total noise, this ultimately leads to a significant reduction in jitter. This work is dedicated to a particular development of this technology, therefore more detailed information regarding their capabilities, internal structure and the most recent results in this field are given in Chapter 1.

- *Monolithic Systems*
  In addition to the aforementioned SiGe pixels (Section 0.4.1), the Monolith project [15] is currently developing devices with internal gain. Thanks to a gain layer placed some micrometres from the sensor backside and a very thin layout (5 µm), it was able to achieve an averaged 17 ps time resolution within a 100 µm-pitch hexagonal pixel.

- *Hybrid Systems*
  The optimization of LGADs for timing measurements gave birth to the Ultra Fast Silicon Detectors (UFSDs) described in the following Chapters. In order to reduce the contribution of the Landau noise to the time resolution, they are usually manufactured as thin ($\sim$ 50 m) devices with moderate gain (20-30). Coupled with their front-end electronics, UFSDs are able to deliver a combined single hit time resolution below 50 ps [16, 17]. Although their excellent timing capabilities, one relevant limitation in the application of UFSDs as tracking detectors consists of no-gain distance of about 70-80 µm in between pads. This dead area makes it impossible to effectively cover large areas with small-pitch devices. A possible solution resides in the introduction of shallow and narrow ($\sim$ 1 µm) trenches [18] to reduce this dead area. Recent studies [19, 20] have shown that these devices maintain the properties characteristic of standard LGADs, while drastically improving their fill factor. Finally, another promising design consists of the Resistive Silicon Detector (RSD). It consists of an LGAD with a continuous gain layer where the segmentation is provided by electrodes coupled with the resistive layer and the charge produced by the multiplication is shared among the electrodes to achieve unique spatial resolutions. The focus of this work is on the novel results and methodologies adopted to develop and characterize such sensors. More information on this topic can be found in the next Chapters.

0.5 The impact of timing in the CMS experiment

The Large Hadron Collider (LHC) accelerator was commissioned in 2010 for high-energy proton-proton collisions and currently operates with a centre-of-mass of 13 TeV and peak instantaneous luminosity of $1.8\text{x}10^{34}$ $\text{cm}^{-2}\text{s}^{-1}$. Since 2020, the statistics gain has become marginal without increasing luminosity. To increment the sensitivity to processes beyond the standard model (BSM), a High Luminosity phase [5] is scheduled to begin in 2029. The target peak instantaneous luminosity is $5\text{x}10^{34}$ $\text{cm}^{-2}\text{s}^{-1}$, with a ultimate operational scenario of $7.5\text{x}10^{34}$ $\text{cm}^{-2}\text{s}^{-1}$. With the advent of HL-LHC, its experiments will face new challenges due to (i) the large number of concurrent interactions occurring at each bunch crossing due to the higher luminosity and (ii) the radiation damage to the components of the detectors. In particular, nowadays each beam bunch is spatially distributed with an RMS of $\sim 5cm$, which crosses with the opposite direction bunch at a rate of 40 MHz. The average number of interactions (i.e. pileup) in this scenario amounts to $\sim$ 40, while in HL-LHC the nominal value for pileup will rise to 140-200. The detectors in LHC will be upgraded for the event reconstruction performances not to degrade. A brief summary of the introduction of a timing detector in the CMS experiment for the HL-LHC upgrade is laid out in this section. Further information on the physics motivation of HL-LHC can be found in [21, 22].

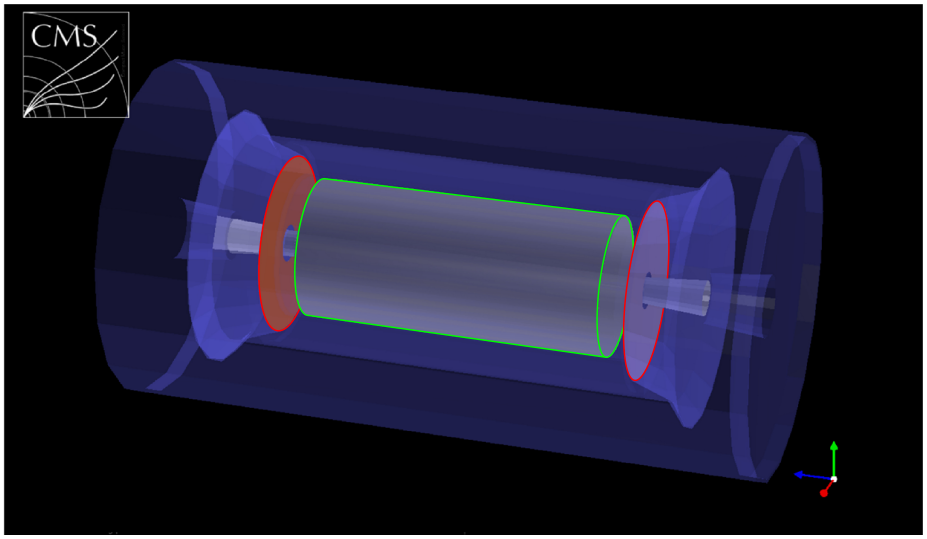

Figure 6: Representation of the MTD of CMS. Highlighted in red are the two endcaps of ETL, and in green is the BTL

0.5.1 The CMS MIP Timing Detector

The CMS collaboration has foreseen the instrumentation of its detector with a MIP timing detector (MTD), providing timing information on the tracks of the impinging particles with a time resolution of about 40 ps during most of the HL-LHC lifetime and covering hermetically up to $|\eta| = 3$. The MTD Technical Design Report [23] provides a comprehensive description of the detector's details. Pileup mitigation in CMS is achieved by particle-flow reconstruction, i.e. an estimation of a list of possible particle candidates obtained by combining the information provided by different sub-detectors. It eliminates tracks or energy depositions inconsistent with the ones originating from the primary vertex of interaction, based on statistical inference techniques [24, 25]. Consequently to HL-LHC, the probability of spatial overlap of primary vertexes at 200 pileup is so high that the particle-flow reconstruction begins to fail at a significant rate [23]. This issue can be addressed with the addition of a timing layer: since primary vertexes RMS spread will be 180-200 ps and broadly uncorrelated to the spatial distribution, the addition of timing to the event reconstruction allows 30-40 ps slicing of the bunch crossing and the consequent unravel of spatially close vertexes. The addition of MTD will provide an enhancement to the CMS physics analysis sensitivity equivalent to a 30% increase to the integrated luminosity over the ten-year lifespan of HL-LHC currently foreseen

The MTD (see Figure 6) consists of a thin layer between the Tracker and the calorimeters and will be divided into two subsections due to different radiation exposure and cost reasons. The Barrel Timing Layer (BTL) will cover the angular region of $|\eta| < 1.45$; it is characterized by a surface area of approximately 2.5 times that of ETL, and its radiation exposure during the whole HL-LHC phase is expected to be moderate ($\sim 2 \cdot 10^{14}$ n_{eq}/cm^2). On the other hand, the Endcap Timing Layer (ETL) will cover the remaining angular region ($1.45 < |\eta| < 3$) and it will be characterized by a large

amount of dose imparted, especially to its inner region (up to $\sim 1.5 \cdot 10^{15}$ n_{eq}/cm^2). BTL can be equipped with crystal scintillators read out by Silicon Photo-Multipliers (SiPMs) [26], whereas, in the case of ETL, the UFSD one is the best available technology [14]. BTL and ETL will not be instrumented with identical detectors because the SiPMs are not sufficiently radiation tolerant for the ETL need, and the cost of covering the barrel with UFSDs would be prohibitive. The silicon sensors that compose the ETL subsystem are of particular interest for the following chapters. Although its 1.3x1.3 mm^2 pixels are too big to represent a solid option for a single 4D tracking layer, this is one of the first examples of utilization of silicon sensors with moderate gain to estimate both a signal arrival time and the impinging spatial coordinates.

UFSD for 4D tracking is the foundation of this work, and their latest developments are described in the following chapters.

In the next chapter is presented a new innovative approach to silicon detectors. A technology based on the LGAD one, consisting in sensors based on charge sharing among multiple pads and with internal gain. The Resistive Silicon Detectors layout and previous production (RSD1) are reported in Chapter 2, while the new results on the more recent RSD2 production are illustrated in Chapter 4. The future development of these type of detectors is documented in Chapter 5, both with the results of the simulation that lead to the new production, foreseen for the next future, whose layout is presented in the last part of the same Chapter.

It is important to note how the current status of R&D does not take into account radiation-resistant sensors in this particular innovation. The objective of the current designs consists in obtaining a product capable of combining optimal timing and spacial performances. On a parallel line, different projects are contributing to the evolution of LGAD designs adequate for extreme fluences [27, 28].

Chapter 1

Ultra Fast Silicon Detectors

Time measurements with silicon devices have become possible in the last ten years as a result of the intensive R&D on Ultra Fast Silicon Detectors (UFSDs) [14]. UFSDs are based on Low-Gain Avalanche Detectors (LGAD) technology and are proven to reach time resolutions 30-40 ps with radiation damage up to $1.5{\cdot}10^{15}$ neq cm^{-2}. They would represent an optimal 4D tracking sensor when timing performances are coupled with an optimised layout to measure the impinging particle hit position on the sensor surface.

This chapter describes the UFSDs, while a more detailed overview of the experimental techniques employed to characterise the sensors is given in Chapter 3.

The first section of this chapter briefly summarises the silicon detector's operation principles. The LGAD technology and its implementation in the UFSD design are then presented, followed by a short description of the future upgrade in HL-LHC. Based on this technology, the candidates' architecture for 4D tracking sensors is then described. Finally, ongoing studies on future development are reported.

1.1 Silicon Detectors for Particle Physics

Silicon detectors traditionally employed in particle physics are referred to as "PiN diodes", i.e. intrinsic (undoped) or very lightly doped silicon between a p-doped and an n-doped region. The two extremes are called electrodes, while the median region bulk. To deplete the sensor volume from mobile charge carriers, the pn junction is negatively polarised by providing a negative voltage to the p^{++} electrode and grounding the n^{++} one. When charged particle impinges on the sensor, an electron-hole pair has a certain probability of being created. These charges then migrate towards the electrodes, driven by the electric field permeating the sensor. Due to this movement, charges are induced on the electrodes, creating a detectable signal in the form of an electric current, which extinguishes when the last charges are collected. However, the motion of the created pairs is obstructed by the interstitial mobile charge carriers of the silicon. To deplete the sensor from these charges, an electric field is provided in the form of the abovementioned

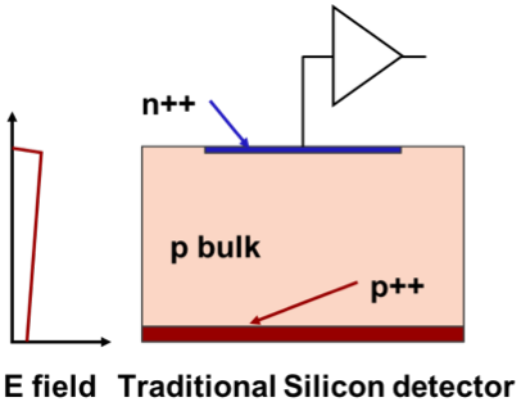

Figure 1.1: Transverse view of a p-doped PiN silicon detector with its Electric field profile.

bias: The bias voltage required to deplete the sensor is fully

$$V_{FD} = \frac{N_{a,eff} e d^2}{2\epsilon_{Si}} \tag{1.1}$$

where $N_{a,eff}$ is the effective acceptor density, e the elementary charge, d the sensor thickness, and ϵ_{Si} the silicon permettivity.

When a charged particle impinges on the silicon bulk, it starts losing energy by *(i)* ionisation and *(ii)* atomic excitation. The average energy loss by a particle per unit length, *stopping power*, can be approximated with the Bethe-Block formula (see [29]. A particle with energy loss at the minimum of this formula is called a Minimum Ionizing Particle (MIP). The energy loss is a stochastic process and follows the Landau distribution, typical of energy loss in materials by ionisation, asymmetric and with a long tail at high energy owing to the δ-rays, i.e. electrons produced by ionisation which have enough energy to cause secondary ionisation. To produce a single electron-hole (e-h) pair in silicon is 3.6 eV, three times higher than its band gap since part of the energy is released as thermal energy in the lattice.

1.2 Signal Formation

The shape of the signal on an individual electrode can be computed employing the Shockley-Ramo [30, 31] theorem:

$$i(t) = -q\vec{v_d} \cdot \vec{E_w}. \tag{1.2}$$

The induced $i(t)$ current by a carrier with charge q is proportional to the drift velocity $\vec{v_d}$ and the weighting field $\vec{E_w}$. The drift velocity depends upon the external bias and the sensor temperature. The signal length and shape are defined by this parameter, where a sharp and short signal is due to a high v_d. At room temperature, the electrons drift velocity saturates for electric fields of about 30 kV/cm. In contrast, the holes velocity does not saturate but reaches an almost constant value above 50-100 kV/cm (shown in Fig. 1.2. The weighting field describes the coupling of the charge with the

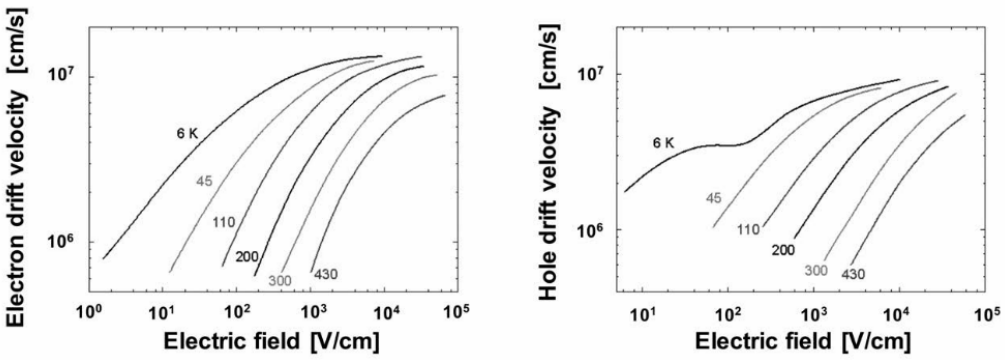

Figure 1.2: Electrons (left) and holes (right) drift velocity v_d as a function of the electric field. Different temperatures are reported. Taken from [32].

electrode. Numerically, it matches the value of an electric field calculated setting at 1 V for the read-out electrode and all the others to 0 V. Therefore, its dependence upon the sensor geometry is the same as the electric field. For example, it is constant between two large electrodes and decreases as $1/d$ if the electrode is a line, being d the distance from it.

1.3 Low-Gain Avalanche Diodes

Central to the evolution of recent silicon sensors is the Low-Gain Avalance Diode (LGAD) technology, making the use of silicon in timing measurements possible. It is based on controlled internal multiplication of charge carriers, increasing the output signal and drastically improving the signal-to-noise ratio. Fine-tuning this technology gave rise to the Ultra-Fast Silicon Detectors (UFSD), i.e. LGADs, whose design is optimised for time measurements. In silicon sensors, the multiplication is obtained if the carriers drift through an electric field greater than circa 300 kV/cm. Above this threshold, the electrons acquire a kinetic energy high enough to produce new *e-h* pairs by impact ionisation [33]. In LGADs, the localised high electric field region is obtained by depleting an additional narrow $p+$ doped layer close to the $n++$ electrode. A representation of a *n-in-p* PIN diode and LGAD are shown in Fig. 1.3. A such additional layer is often called *gain layer* and is obtained implanting a density of acceptors $N_A \sim 10^6$ atoms/cm^3 of boron or gallium with an implant 0.5-1 µm wide at a depth of about 0.5-2 µm.

1.3.1 Charge multiplication and Gain

The gain G is defined as the ratio between the total number N_{h-e} of *e-h* holes collected over the same number obtained in the absence of multiplication $N_{0;h-e}$, i.e.

$$G = \frac{N_{e-h}}{N_{0;e-h}}. \tag{1.3}$$

Under the assumption that (i) hole multiplication does not occur, (ii) the mean free path λ_n necessary for an electron to acquire enough energy to

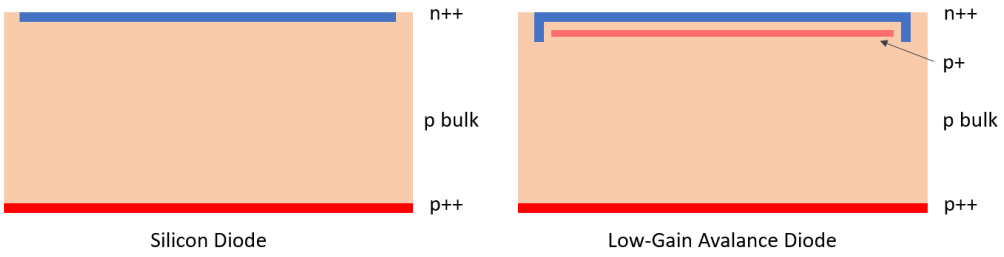

Figure 1.3: Silicon diode with no internal gain (left) and LGAD with p+ gain layer (right).

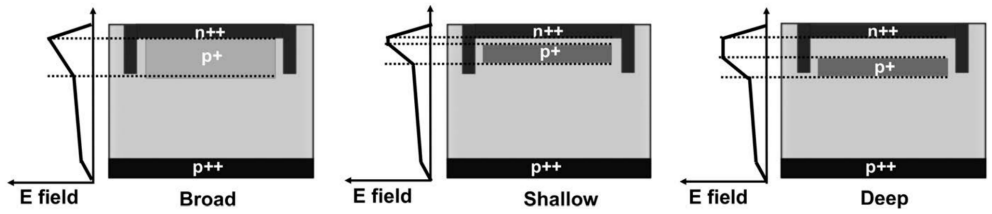

Figure 1.4: Representation of different gain layer designs: broad (*left*), shallow (*centre*) and deep (*right*).

achieve charge multiplication is constant through the high field region and (iii) the generation of secondary or higher term particles is neglected, then equation 1.4 holds

$$N_{e-h}(d, E, T, \Phi) = N_{0;e-h} \cdot e^{\alpha_n(E,T,\Phi)\cdot d}, \tag{1.4}$$

being d the distance travelled inside the high field region, $\alpha_n = (\lambda_n)^{-1}$ the impact ionization coefficient for the electrons, E the electric field, T the temperature and Φ the irradiation fluence. Therefore the final gain becomes $G = e^{\alpha_n \cdot d_{drift}}$, if the entire drift region d_{drift} is crossed (in the case of a path perpendicular to the sensor surface). This last parameter depends on the depth of the gain layer. As shown in Fig. 1.4, different approaches have been attempted in the UFSD design: one with a broad $p+$ implant contacting the $n++$ electrode; one with a narrow gain layer, but fairly close to the $n++$ electrode; one with a narrow and deep implant. In the same figure can be seen an approximation of the electric field associated with each geometry. Since one wants to obtain the same gain in all variants, the gain layer must be doped less if its depth is increased to maintain the electric field integral constant. On the one hand, the broad design is the most delicate: being the implant closest to the *pn* small process variations could lead to very different gain values. On the other hand, the shallow and deep versions are less sensitive to process differences as multiplication mostly occurs in the flat electric field region.

1.4 UFSD signal formation

The UFSD signal can be extrapolated once the signal generation in a PiN diode is understood. Being the pixel lateral size much larger than its thick-

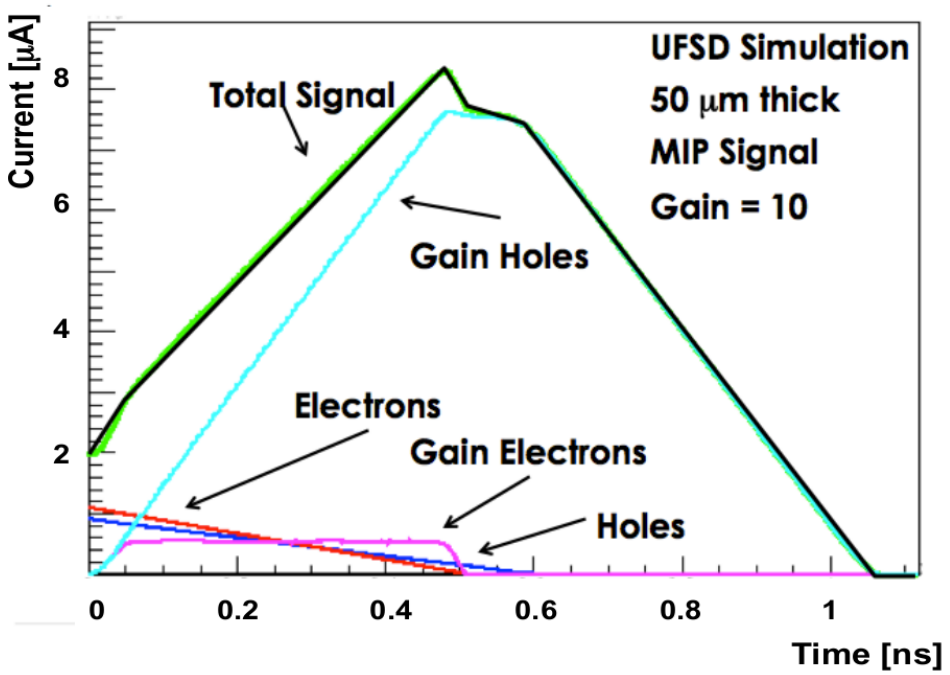

Figure 1.5: UFSD signal formation example. The contributions of primary and electrons and holes are visible. The simulated sensor consists of a 50 µm-thick UFSD performed in Weightfield 2 [34].

ness, it is possible to assume that the weighting field is a constant and $E_w \propto 1/d$. Assuming that a high-enough electric field saturates the drift velocity, the current generated in a PiN can be calculated using Ramo-Shockley's theorem (Eq. 1.2). Therefore one obtains

$$I_max \propto Nq\frac{1}{d}v_{sat} = (n_{e-h} \cdot d)q\frac{1}{d}v_{sat} = n_{e-h}qv_{sat}, \tag{1.5}$$

where q is the elementary charge, v_{sat} is the abovementioned drift velocity, N is the number of charges created by the ionizing particle, equal to $n_{e-h} \cdot d$ if one assumes uniform ionization, being d the sensor thickness and n_{e-h} the number of e-h pairs generated per unit length. From Eq. 1.5 emerges how the current does not depend on the sensor thickness, with the current saturating as the drift velocity saturates. In particular, in PiNs, a current higher than $\sim$ 1.5 µA cannot be achieved since the weighting field E_w decreases at the same rate as the thickness d (and the number of charges) increases. Therefore, PiN diodes have minimum reachable time resolution.

UFSD signals benefit from the gain mechanism. The primary electrons and holes drift from the point they're generated towards the $n{+}{+}$ and $p{+}{+}$ electrodes, respectively, as in a PiN diode. When the primary electrons enter the gain layer, secondary $e-h$ pairs are produced, and the avalanche mechanism is triggered, giving rise to gain electrons and holes. The multiplication takes place close to the $n{+}{+}$ electrode, so electrons and gain electrons are collected first and contribute to the earliest part of the signal (see Fig. 1.5). On the contrary, gain holes must travel through the bulk before being collected on the anode, generating most of the induced signal.

The time characteristics of the UFSD signals differ from those of a PiN diode. The length of a PiN diode signal is only due to the holes drift time, while in UFSDs both electrons and holes contribute to it. Similarly, the rise time of a UFSD is more prolonged because in PiNs it is equal to the time it takes to the *e-h* to reach their drift velocity, while in UFSDs it is equal to the electrons drift time. It is possible to estimate the current generated by the multiplication mechanism assuming several primary electrons N_e enter the gain layer in the time interval dt, assuming a constant and saturated drift velocity v_{sat}. Therefore, the number of primary electrons is $N_e = n_{e,h} v_{sat} dt$, and if the gain is G the number of secondary electrons is proportional to

$$dN_{gain} \propto n_{e,h}(v_{sat}dt)G_i. \tag{1.6}$$

Using Ramo-Shockley's theorem and assuming a pixel size much larger than the thickness d of the sensor, i.e. $E_w \propto 1/d$, the current variation dI is

$$dI = dN_{gain} q v_{sat} \frac{1}{d} \propto n_{e,h}(v_{sat}dt)G_i \cdot q v_{sat} \frac{1}{d}, \tag{1.7}$$

which leads to

$$\frac{dI}{dt} \sim \frac{dV}{dt} \propto \frac{G_i}{d}. \tag{1.8}$$

This final result (Eq. 1.8 and Fig. 1.6) shows how the UFSD slewrate dI/dt is proportional to the ratio of the sensor gain and thickness G_i/d. Thus, the optimal sensor for timing applications has a high gain and is thin. It should be noted that the gain used in the last passages G_i differs from the gain defined in equation 1.3. The gain G does not take into account charges that are trapped by defects, which are prevented from undergoing multiplication. On the other hand, the current gain G_i is an effective gain obtained from the leakage current measurements, which takes a long time to generate and contains also the contribution from untrapped charges. From this point forward the signal gain G will be employed, if not otherwise specified. Finally, it is possible to compute the maximum current that can be generated in a UFSD:

$$I_{max} \propto N_{max} q \frac{1}{d} v_{sat} = (n_{e,h} G d) q \frac{1}{d} v_{sat} = q(n_{e,h} G) v_{sat}, \tag{1.9}$$

analogous to eq. 1.5 and meaning that the maximum current does not depend on the sensor thickness, but rather on the value of the gain and the drift velocity.

It is important to notice how the gain mechanism also introduces additional noise. In every silicon sensor, the flow of electrons over the *pn* junction introduces a current fluctuation called shot noise. The variance of this noise is equal to the square root of the surface and bulk generation leakage currents ($I_{surface}$ and I_{bulk} in a given bandwidth interval Δf

$$\sigma^2_{shot} = 2q\Delta f(I_{surface} + I_{bulk}), \tag{1.10}$$

being q the fundamental charge. This contribution to the noise does not constitute a relevant source of noise in PiN diodes, whereas in irradiated UFSD this noise can become relevant due to the increase in leakage current.

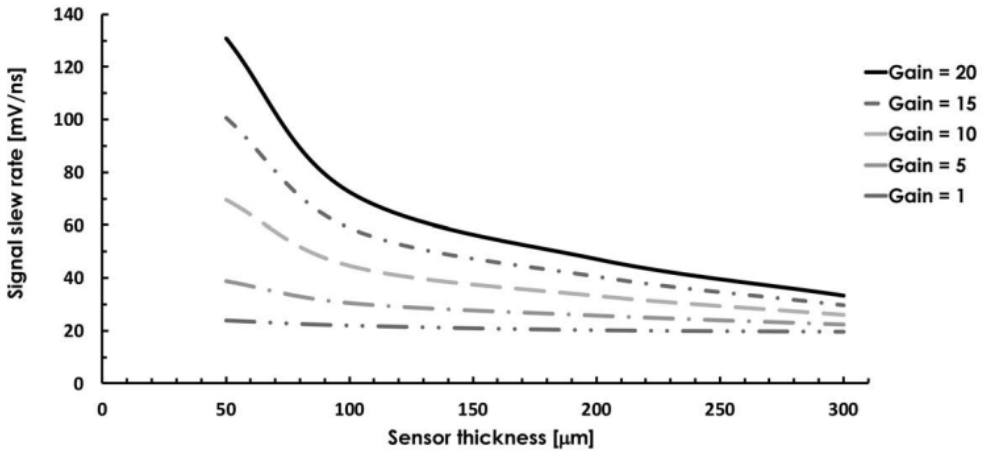

Figure 1.6: Signal slew rate as a function of the sensor thickness. Different gain values are considered.

A second effect contributes to the shot noise and makes it larger in sensors with gain [35]. The so-called excess noise generates from the statistical fluctuations in the multiplication of primary electrons. In fact, the gain value G is equal to the number of secondary charges on average only, while a primary electron could generate a number of secondary carriers that is not exactly G. This variability increases the shot noise by a factor F called the excess factor. In [36] an empirical fit of F as a function of G is found:

$$F = Gk + (2 - \frac{1}{G})(1 - k) \sim G^x \tag{1.11}$$

where k is the ratio of the impact ionization coefficients of holes and electrons, and x is the excess noise index. Therefore eq. 1.10 for UFSD should include the excess noise factor F and the gain G

$$\sigma^2_{shot} = 2q\Delta f(I_{surface} + I_{bulk}G^2F). \tag{1.12}$$

It becomes evident that the gain factor F should be kept low to reduce the shot noise. This can be achieved by using the *n-in-p* design employed for UFSDs, reducing the holes impact ionization coefficient (and k). The signal-to-noise ratio (SNR) then becomes

$$SNR = \frac{IG}{\sqrt{2q\Delta f(I_{surface} + I_{bulk}G^2F)}} \propto \frac{1}{\sqrt{F}}. \tag{1.13}$$

From eq. 1.13 it is possible to extrapolate how internal multiplication can degrade the sensor SNR. This result does not consider the contribution of the read-out electronics, which is the dominant factor in degrading the detector's performance. As shown in Figure 1.7, the shot noise starts playing a dominant role for gain values greater than 10; this is why UFSDs are engineered to be operated at gain values of about 10-30.

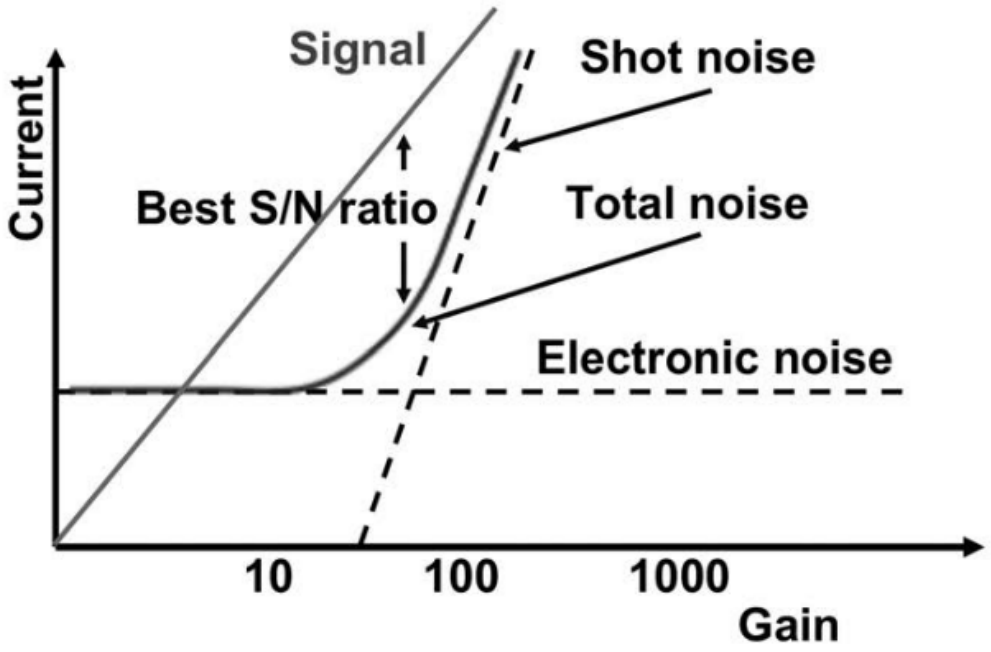

Figure 1.7: Current and shot noise as a function of gain in a UFSD sensor. Partial contributions to the noise are shown as a function of gain.

1.4.1 UFSD: a timing detector

Timing measurements of a particle hit on a silicon sensor can be achieved only if the readout electronics closely match the sensor characteristics. The detector must provide current signals proportional to the energy deposited by the impinging particle with the best possible consistency. At the same time, the electronics should be able to provide information on the point of signal with minimum uncertainty. In Fig. 1.8, the sensor is simplified with current generator I_{det} in parallel with a capacitor C_{det} read out by a current shaper pre-amplifier. A comparator receives the output signal from the pre-amplifier and produces a logic signal when a certain voltage threshold V_{thr} is exceeded. a Time to Digital Converter then converts the output of the comparator into a digitized signal. Effects on the signals near the voltage threshold, i.e. change in the signal shape, can smear the determination of the hit time.

The most important factors that affect the temporal resolution of a silicon sensor are

$$\sigma_t^2 = \sigma_{jitter}^2 + \sigma_{Ionization}^2 + \sigma_{Distortion}^2 + \sigma_{TDC}^2. \tag{1.14}$$

- σ_{jitter} is due to the electronic noise that might cause the comparator to fire sooner or later than the expected time (see Fig. 1.9). This is caused by the sensor itself and every other component of the readout chain until the comparator. Since the jitter depends on the noise N and the slew rate dV/dt of the signal,

$$\sigma_{jitter} = \frac{N}{dV/dt} \approx \frac{t_{rise}}{S/N} \tag{1.15}$$

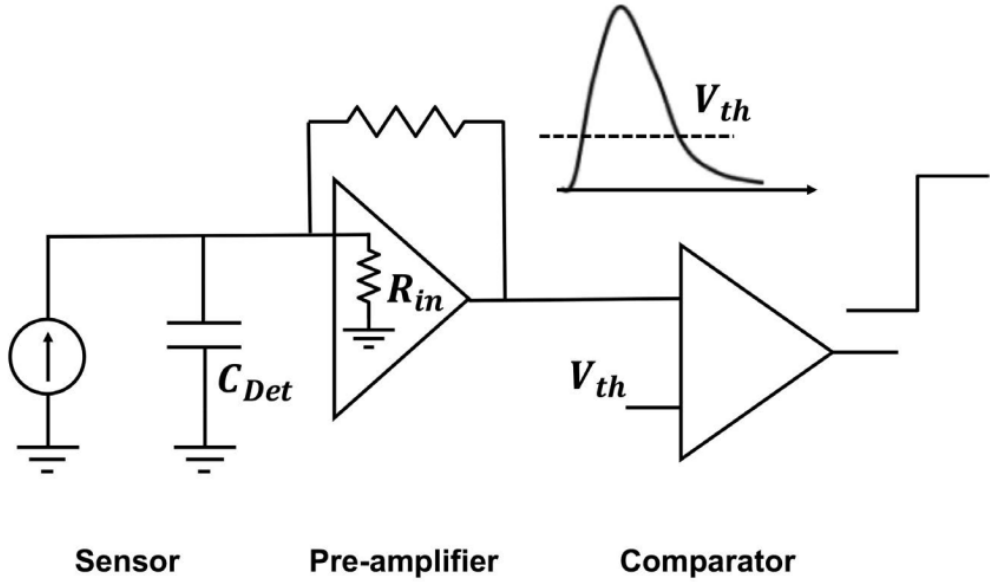

Figure 1.8: Schematic representation of a timing sensor and its readout electronics.

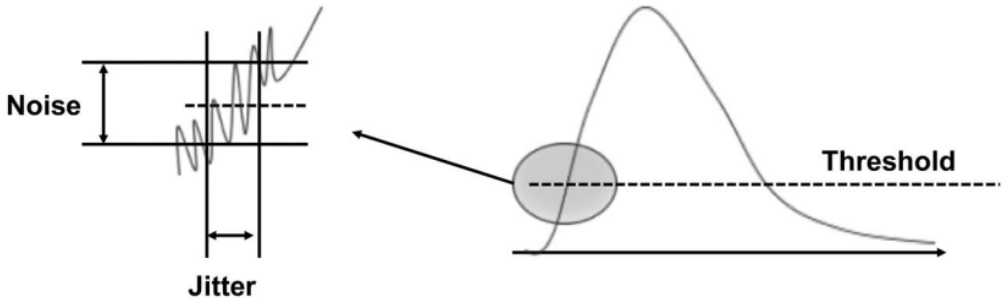

Figure 1.9: Jitter uncertainty introduced by the noise on the rising edge of the signal.

where the slew rate can be approximated to a A/t_{rise} assuming a linear rising edge of the signal, being S the signal amplitude and t_{rise} its rising time. To minimize the jitter, two opposing aspects of the electronics design come to collide: a high slew rate necessitates a large bandwidth, while low noise calls for a small electronics bandwidth.

- $\sigma_{Ionization}$ derives from the stochastic nature of the ionization caused by a charged particle impinging on the sensor. The *e-h* pairs density varies on an event-by-event basis, producing two effects interconnected between each other: (i) Landau noise and (ii) time walk.

  (i) The energy released by a particle crossing a thin layer of material follows a Landau distribution, characterized by being non-symmetrical with long tails at values of high energy deposition. The term σ_{Landau} accounts for this non-uniformity. Since events with high average deposited energy possess a broader distribution, a way to reduce the contribution of this term consists in

having thin sensors $\sigma_{Landau} = 25ps$ for 50 µm thick UFSDs). In a well-designed system, the Landau term dominates the total time resolution.

(ii) As visible in Fig. 1.10 (left), large signals cross fixed thresholds sooner than signals with lower amplitude. This effect is called time walk and cannot be avoided in a system employing a fixed discriminator threshold. However, it can be almost completely eliminated using a Constant Fraction Discriminator (CFD), i.e. a variable threshold equal to a certain fraction of the total signal amplitude.

- $\sigma_{Distortion}$ corresponds to the uncertainty brought by the non-uniformities of the drift velocity and weighting field. These two quantities are the fundamental blocks of Shockley-Ramo's theorem ($i \propto qv_{drift}E_w$, Eq. 1.2) and need to be as constant as possible to generate a very uniform current across the sensor and achieve small temporal resolution. Regarding the drift velocity, it should be maintained uniformly across the active volume of the sensor. The simplest way to do so consists of having an electric field high enough to saturate it, i.e. greater than 30 kV/cm in the hole detector. The weighting field E_w depends on the dimensions of the electrodes with respect to one another and the rest of the active volume. As shown in Figure 1.11, if the electrodes are almost the same size and are much larger than the thickness, the weighting field is constant. Finally, delays due to the propagation of the signal along the $n{+}{+}$ electrode can affect the timing performances. After forming inside the $n{+}{+}$ electrode, the signal travels from the particle hit point towards the read-out electronics. The resistivity of the $n{+}{+}$ layer can introduce a non-zero delay ($\sim 0.5ps/\mu m$). To avoid this, traditional UFSD employs a metalization layer on top along with the signal can travel. In the newest designs of UFSD for 4-D tracking, the delay is accounted for since the hit position is extracted.

- σ_{TDC} is due to the aforementioned Time to Digital converter. It records the time in which the discriminator fires in bins of a finite width ΔT. Consequently, the uncertainty associated with this component is $\Delta T/\sqrt{12}$. Thanks to fine binning of modern High Precision TDCs, $\sigma_{TDC} \sim 10ps$ and it is negligible with respect to the other terms.

From what is said above, the optimal sensor geometry resembles a parallel plate capacitor, with the electrodes much larger than the detector thickness. Under these assumptions, the weighting field and the drift velocity are as uniform as possible, meaning that the distortion term is negligible. Therefore, the σ_{Landau} and σ_{jitter} are dominant in determining the sensor timing capabilities, meaning that

$$\sigma_t = \sqrt{\sigma^2_{Landau} + \sigma^2_{jitter}} \tag{1.16}$$

is a good approximation of the total UFSD time resolution, given that these two terms are uncorrelated. Of these two, the jitter can be minimized,

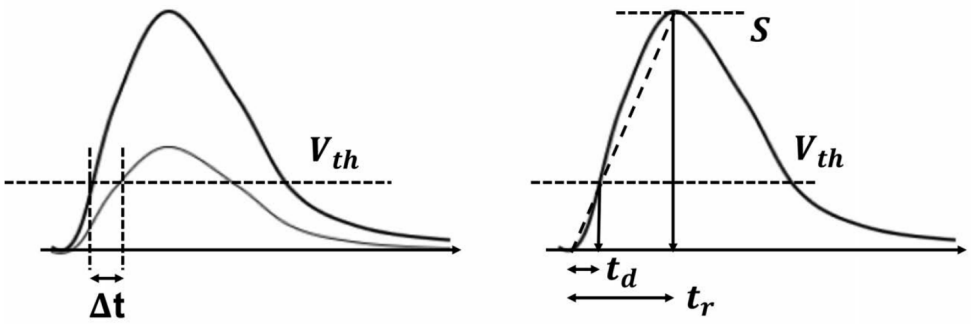

Figure 1.10: On the left, two concurrent signals cross the threshold at different times. This effect is known as *time walk*. On the right a representation of the linear approximation of the rising edge of a signal.

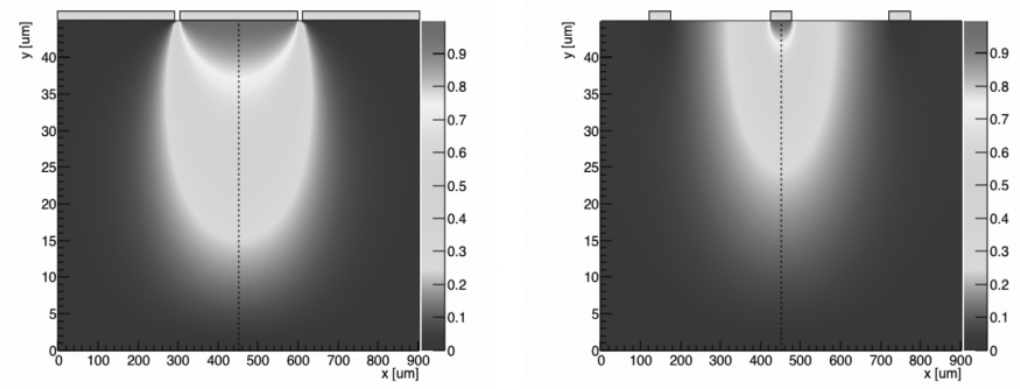

Figure 1.11: Weightfield map of two different sensors simulated with Weightfield 2. 300 µm pitch sensor with an electrode/gain width of 290 µm *right* and 50 µm *left*. In the one with the narrower implant base, the weighting field and the collected current are not constant along the x-axis, increasing the temporal uncertainty.

leaving the Landau term for a given sensor thickness as the predominant contribution to the total sensor resolution.

UFSD read-out electronics

A key aspect of obtaining an optimal time tagging sensor resides in matching the UFSD and the read-out electronics, maintaining the system's jitter as low as possible. A vital aspect of the design of electronics is the amount of power available. Read-out chips designed for timing applications, as ATLAS ALTIROC [37] and CMS ETROC [17], consume $\sim 2-3$ mW per channel and reach a jitter term lower than 30 ps for pads with 2-6 pF capacitance. Overall, it is evident that systems with small-pitch sensors are disadvantaged whilst traditionally employed in tracking systems. For this reason, a new paradigm for 4D tracking has to be found, especially in experiments with a low power budget. Finally, the bandwidth of a current-mode amplifier reading a 50 µm thick UFSD should be 400-800 MHz.

Multi-Pad UFSD

Traditional are employed in multi-pads arrays that cover a certain amount of space. For example, the Endcap Timing Layer of CMS will be equipped with modules composed of a 16x16 array with 1.3x1.3 mm^2 pads. These large dimensions, at least compared to nowadays tracking systems, are due to the distance from the primary collision vertexes, the experiment power budget, the vast area to be covered and the cooling system requirements. Moreover, in Figure 1.12 is visible a region in between the pads where no gain layer is present. If a particle hits the space in between the pads the signal is then not multiplied; for this reason, this region is called the no-gain region. The signals coming from this region are not amplified, therefore the signals in these regions are well below the thresholds in the electronics. Multiple layouts of the inter-pad area have been developed [22], where the most aggressive have a no-gain distance in between pads of about 60 µm. It is important to highlight how this value represents a low limit with the current UFSD paradigm. The fill factor F estimates the amount the sensor volume is sensitive to the passage of particles with respect to the total volume $F = V_{gain}/V_{tot}$. Being that HEP experiments requirement for trackers is $F \geq 95\%$, it is immediately evident that a sensor with a pitch in the order of tens of micrometres would not satisfy this constraint.

1.5 Radiation damage in silicon detectors

High-energy physics trackers are exposed to high levels of particle fluence during their lifetime. A particle's repeated loss of energy within a silicon device can cause its properties to degrade (see 1.5.1. This phenomenon plays a central role in the device choice: an ideal detector should be able to withstand the damages while maintaining performances above the required ones. The so-called *radiation damage* can be divided into two distinct categories, depending on where the damage occurred: surface and bulk damage.

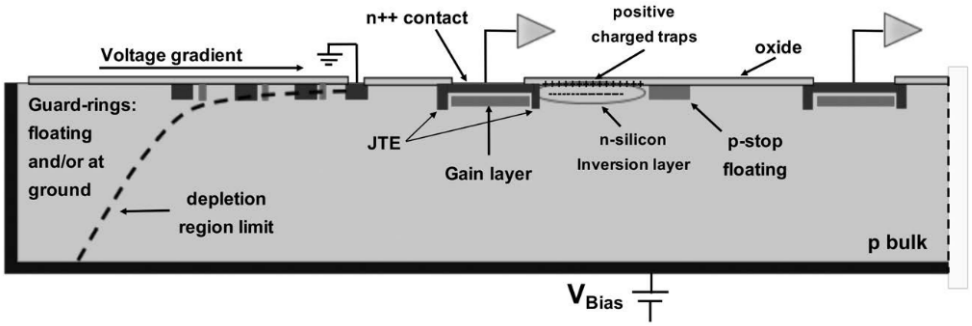

Figure 1.12: Cross section of a multi-pad UFSD. Circled in between two pads are the positive charges that are trapped in the no-gain region.

- **Surface damage** is due to ionisation processes in the interface between the silicon oxide that covers the sensor surface and the silicon. This cause several positive charges to be trapped in the lattice and the creation of the so-called inversion layer. It is of particular importance in the case of pixeled detectors: the trapped charges short the n++ electrodes and it is the reason why p-doped structures (p-stop) are needed in between pads, decreasing the fill-factor value.
- **Bulk damage** derives from non-ionising processes due to hadrons interacting with the lattice. Consequently, silicon atoms are displaced from the lattice and produce silicon interstitials and vacancies. After migrating, they can create defects or clusters of defects.

The convention introduced in [38] is traditionally employed to quantify the amount of damage dealt to the silicon lattice by different particles. One refers to Non Ionizing Energy Loss (NIEL) as the fraction of energy not spent in ionisation. The standardised value to which all particles and energies are normalised is 1 MeV neutrons.

1.5.1 Impact of radiation damage silicon detectors

Defects produced by the migration of interstitials, vacancies and clusters through the silicon lattice create macroscopical effects in silicon sensors. The main consequences are:

- *Leakage current:* The increase of leakage current is an unavoidable effect of radiation damage which can cause the power consumption to grow. Since in LGADs the leakage current is proportional to the gain, the increase in leakage current is significantly greater than in PiN sensors. Its value is proportional to the depleted volume V_d, the intrinsic carried density n_i, the generation lifetime τ_g and the gain G:

$$I_{bulk} = GI_{no\,gain} = G\frac{V_d q_0 n_i}{\tau_g}, \tag{1.17}$$

being q_0 the elementary charge. When irradiated, the leakage current increases by a factor $\delta I(\Phi_{eq}) = GV_d\alpha\Phi_{eq}$, proportional to the 1-MeV

equivalent fluence Φ_{eq} and the damage constant α. In LGADs, it is possible to cope with this increase in current by thinning the sensors or lowering the operating temperature T, since $I_{leak}^{no\ gain} \propto T^2 e^{\frac{1.2eV}{2k_bT}}$, where k_B corresponds to the Boltzmann constant.

- *Charge collection efficiency (CCE):* a fraction of the charge carriers are trapped in the lattice deep defects created by radiation damage. Since more charge is collected at higher drift velocity, this effect depends on the drift duration and not on the drift length. The current signal $i(t)$ follows an exponential decrease in an irradiated sensor, with time constant $\tau_{CCE} \propto \Phi_{eq}^{-1}$.

- *Doping concentration:* Three different mechanisms concur in changing the doping concentration of silicon sensors: acceptor creation, donor and acceptor removal. Eq. 1.18 shows how the density of effective dopants N_{eff} varies as a function of the equivalent fluence Φ_{eq} and the initial values of donor/acceptor concentrations, N_{D_0/A_0}

$$N_{eff} = N_{D_0} e^{-c_D \Phi_{eq}} - N_{A_0} e^{-C_a \Phi_{eq}} - g_{eff} \Phi_{eq}, \tag{1.18}$$

  where c_D/A are the donor/acceptor removal coefficients and the last term represents the acceptor-like defects creation, proportional to the coefficient g_{eff} and the fluence. In UFSDs this translates into a lowering of the doping concentration in the gain layer, with consequent increase in the bias needed to collect a certain amount of charge. At a sufficiently high fluence ($\Phi_{eq} > 1 \cdot 10^{16} n_{eq}/cm^2$, the gain layer acceptor doping density matches the one of the bulk and the sensor does not present gain. Different techniques to mitigate this effect have been attempted, see [39] for reference.

- *Decreased mobility:* when the fluence increases, the number of scattering centres grows and the mobility μ of the electrons end holes decreases. Lover mobility in the medium implies lower kinetic energy, lower collected charge and lower multiplication in gain-based detectors.

Though essential in timing sensors R&D, radiation damage is not central for the purpose of this work discussion. For more detailed information on this matter see [39].

The characteristics of the UFSD sensors are the foundation on which bases the development of the Resistive Silicon Detectors described in the next Chapter.

Chapter 2

Resistive Silicon Detectors

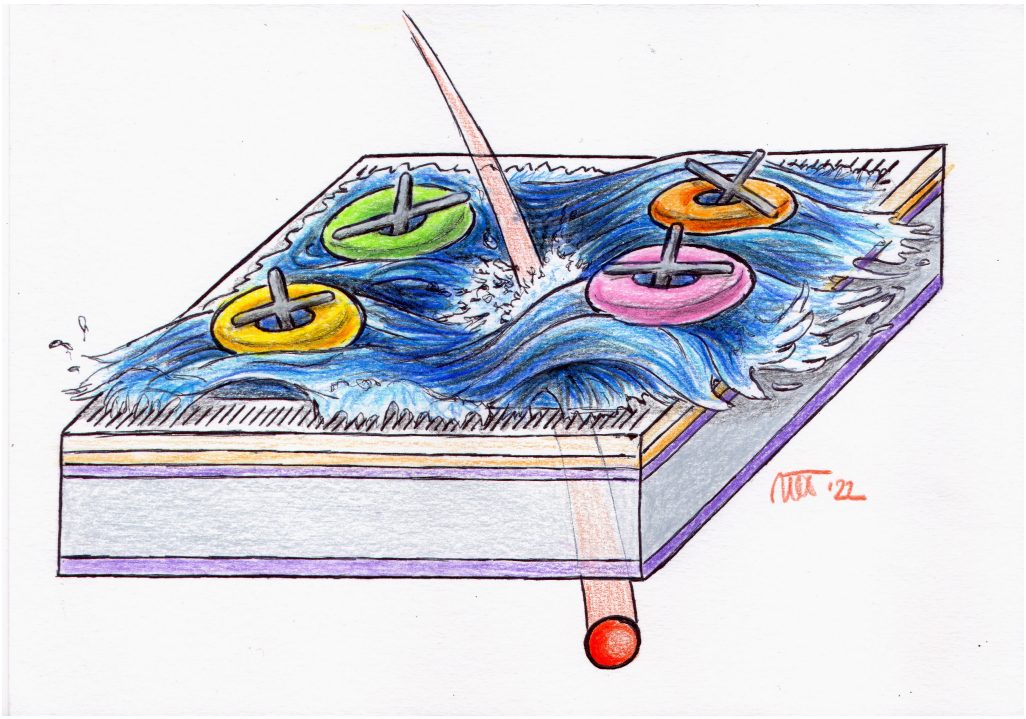

Figure 2.1: Artistic representation of an RSD detector by Marta Tornago.

The results of Chapter 1 assess that a 4D tracking system with traditional UFSD would not achieve accurate-enough spatial and temporal resolution for a 4D tracking system. Different strategies must be implemented in UFSDs to achieve a precise estimate of the hit position and a high fill factor, combined with their usual timing performances. This chapter illustrates a promising approach to solving these difficulties: the Resistive Silicon Detector (RSD) technology. Based on the UFSD design and the LGAD technology, it changes the paradigm of traditional silicon sensors for tracking by the implementation of charge sharing over a resistive surface with the addition of the timing performances typical of UFSDs. In this Chapter, the two productions of RSD by Fondazione Bruno Kessler are described: RSD1 and RSD2. While RSD1 is not the main topic of this thesis, the results obtained on these sensors laid the ground for the second RSD

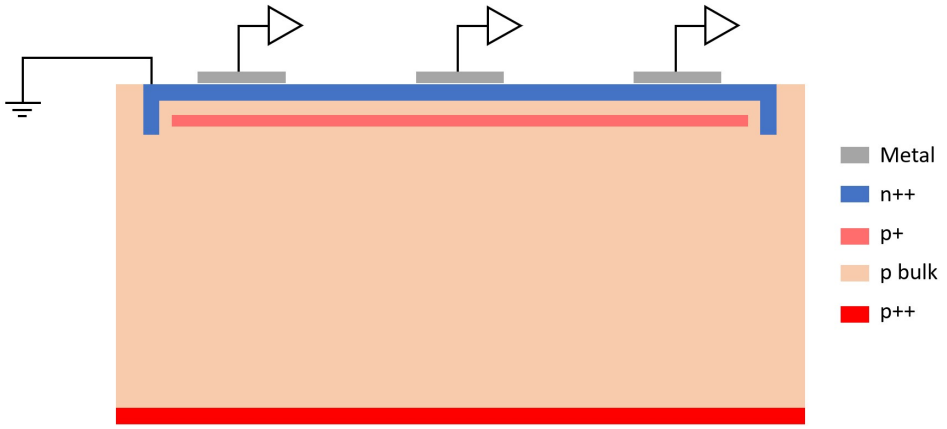

Figure 2.2: Cross-sectional layout of a generic RSD. From top to bottom: metallic read-out pads, resistive layer ($n{+}{+}$), gain layer $p+$, slightly p-doped bulk and $p{+}{+}$ electrode.

batch, RSD2. The RSD2 characteristics were tuned to match the information gained and are illustrated in Chapter 4. Further R&D efforts are being brought out to give life to a third production with additional improvements, which is described in Chapter 5.

While the expectations and performances of this design are excellent, it should be noted that the R&D on the RSDs is ongoing. Currently, no solution is provided to the problem of LGAD radiation hardness up to the scale of doses that will be delivered in future experiments (see Chapter 0).

2.1 Resistive Silicon Detectors design

In RSDs, the operation principle of traditional trackers for which the pixel size is determined by the desired position resolution is changed. Instead, their pitch can be chosen based on the occupancy of the detector only. In this design, the particle density determines the pixel size and even large pixels are able to achieve the required position resolution.

RSDs are possible thanks to a different sensor layout shown in Figure 2.2: when a particle impinges on the detector, the charges multiply and travel towards their respective electrodes like in traditional UFSDs. The internal gain creates a high electric field in the volume underneath the $n{+}{+}$ resistive sheet. Moreover, since the $n{+}{+}$ layer lateral dimensions are much larger than the sensor depth, the weighting and electric fields are uniform over the detector depth, requisites for good temporal resolution.

The difference with standard UFSDs resides in how the signal is picked up, where small metallic pads are present instead of a singular large one. This geometry allows the charges to be shared between pads: the key feature of the resistive readout is that the current caused by the impinging charged particle is shared between nearby pads analogously to a current divider. The i-pad reads a fraction of the total current I, which depends on the

impedance Z_i between the impact point and the pad itself, i.e.

$$I_i = I \frac{1/Z_i}{\sum 1/Z_i}. \tag{2.1}$$

Thanks to the signal splitting, a point on the RSD surface can be uniquely identified by the amplitudes collected by the pads. The hit position is then reconstructed by combining the information from multiple pixels with simple analytical or more advanced algorithms, making it possible to achieve spatial resolution smaller than the one obtainable with traditional single-pixel read-out ($\sigma_x << pitch/\sqrt{12}$). Because of the RSD design, single-pad segmentation is not needed. The gain layer is then not segmented like in multi-pad LGADs which require a Junction Termination Extension (JTE), but the definition of the pixels is derived by the AC-pads only. Therefore, RSDs have an intrinsic fill factor equal to 100 % with the additional advantage of drastically decreasing the number of readout channels and corresponding electronics. Moreover, the relatively simple geometry and structures make this design cheaper to produce on a large scale compared to an equivalent pixelated sensor. A possible drawback of this design may be represented by the charge sharing between adjacent pads. In fact, the occupancy might be limited due to the large area covered by a limited set of electrodes and the signal-to-noise ratio worsens when more than the desired amount of pads are involved in the reconstruction. The area where a single pad is sensitive has to be finely tuned through the doping profiles of both the $p+$ gain layer and the resistive electrode. Another important role is played by the capacitance of the metal pads, which collect the signal and, if present, the coupling resistance of the pad with the resistive sheet. Both these parameters should match the readout electronics.

Two versions of RSD have been conceived depending on the coupling between the $n++$ electrode and the metallic read-out pads: AC-coupled and DC-coupled RSDs.

2.1.1 AC-coupled RSD

The AC-coupled RSD (in short, AC-RSD) presents read-out pads coupled AC with the resistive $n++$ electrode thanks to a thin layer of silicon oxide positioned between them. When a charged particle impinges on the detector, a signal is induced on the $n++$ (see Chapter 1). The collected charges start to drift from the generation point to the contact to ground positioned to the edge of the sensor, also called *DC contact*, flowing under the metal pads as shown in Fig. 2.3. Therefore a bipolar signal is induced on the metal pads whose amplitude depends on the distance between the read-out pad and the particle impact position. Typical characteristics of the AC-RSDs signals are:

- their total integer is equal to zero since they are induced thanks to the coupling with the AC-pads;
- the positive lobe of the signal discharges with an RC time constant due to the $n++$ layer resistivity and the AC-pad capacitance. This

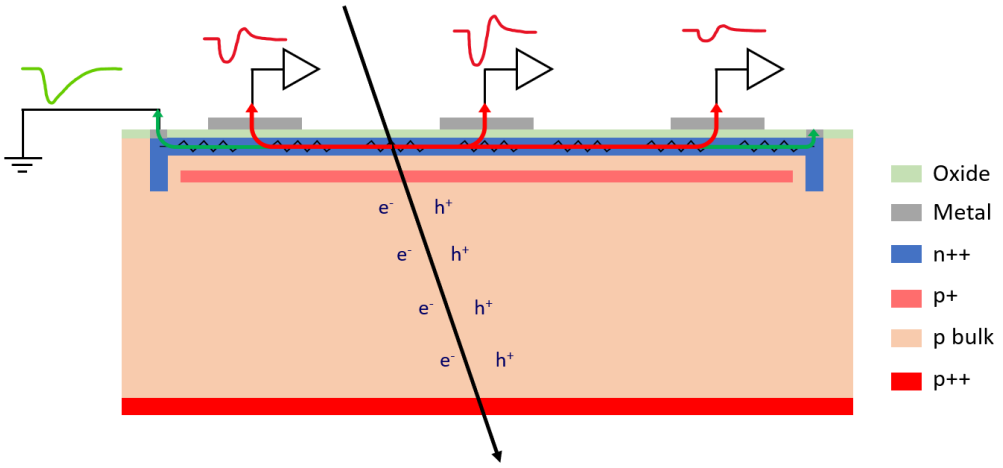

Figure 2.3: Cross-sectional representation of an AC-RSD.

value should be kept small enough to avoid signals pile-up and allow a prompt return to the baseline. At the same time, the RC constant has to be tuned to be longer than the signal formation time ($\sim$ 1-2 ns) to avoid ballistic effects;

- the negative amplitude is proportional to the distance between the point of the $n{+}{+}$ in which the signal is collected and the read-out pad. It also depends on the RC constant and, therefore, on the $n{+}{+}$ resistivity and pad capacitance. Another actor in the signal spitting process is the number of pads that collect it: RSDs are based on the signal sharing between more pads and the relative distance between the electrodes determines the shape of the signals for a certain hit position. Finally, the gain value at which the sensor is operated plays an important role: the temporal performances greatly depend on this parameter (see Section 1.4.1) and the signals are split between the AC-pads, therefore the gain plays a greater role than in traditional UFSDs.

The $n{+}{+}$ layer, the coupling oxide, the dimensions of the metal pads and the gain value have to be carefully tuned to match the desired performances. For this reason, a thorough campaign of simulations has been carried out employing 2D/3D Technological Computer-Aided Design (TCAD) simulations. Firstly, 1D preliminary TCAD simulations have been carried out to extract output waveforms [40]. Such output was then implemented into Spice [41] to simulate a full sensor's electrical behaviour and extract the electrode resistivity, the oxide thickness, the pad capacitance and its size and pitch. Subsequently, more detailed

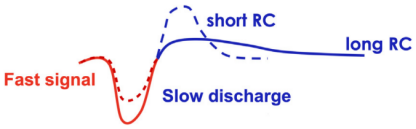

Figure 2.4: Typical signal generated by an AC-RSD. A fast negative lobe is followed by a slow discharge whose time constant depends on the characteristics of the system.

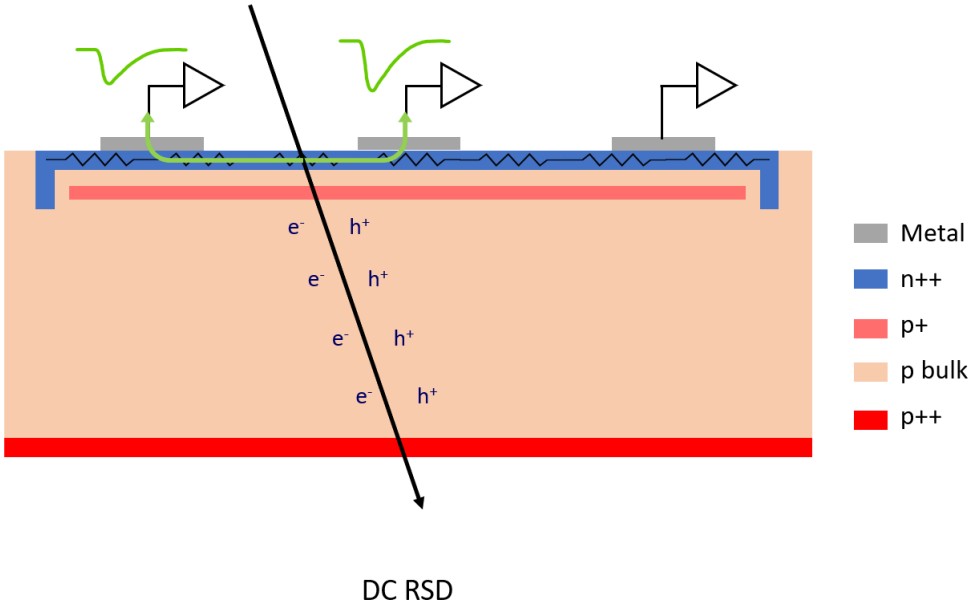

Figure 2.5: Representation of a DC-RSD.

simulations have been performed [42] with a TCAD tool to characterize the AC-RSD in terms of charge multiplication and its electrical properties, such as charge sharing and signal coupling. Such procedure allowed to define the layout of the first batch of AC-Coupled RSD produced by Fondazione Bruno Kessler (FBK), called RSD 1 and described in Section 2.2. The full characterization of the RSD1 devices led to a second production of AC-RSD in which various geometrical dispositions and layouts of the AC-pads were explored (see Section 2.3).

2.1.2 DC-RSD

The DC-coupled Resistive Silicon Detector (DC-RSD in short) consists of a UFSD with resistive read-out where the electrodes are DC coupled to the $n{+}{+}$ electrode. This design aims at reducing the number of pads involved in the charge sharing to achieve better spatial and temporal resolution, as will be described in Section 4.2, combined with better behaviour in high-occupancy applications due to the confinement of the signal among a more limited number of pads, therefore limiting the cross-talk. Contrarily to AC-RSDs, DC-RSDs would solve a few issues of the AC-RSDs as the dependence of the number of pads that collect the signals on the hit position, the bipolarity of the signal and the oscillation of the baseline in large and/or irradiated sensors. Moreover, the coupling oxide component would be eliminated, leaving one less free parameter of the system. An in-depth description of the future DC-RSD production and the simulations that were made to achieve its full layout are the subject of the last chapter of this work, Chapter 5.

Wafer #	type	n^+ dose	p^+ dose	diel. thickness
1	FZ	A	0.92	L
2	FZ	A	0.94	L
3	Epi	A	0.94	L
4	FZ	A	0.94	H
5	FZ	A	0.96	L
6	Epi	B	0.92	L
7	FZ	B	0.94	L
8	FZ	B	0.94	L
9	FZ	B	0.96	L
10	FZ	B	0.96	H
11	FZ	C	0.92	L
12	Epi	C	0.94	L
13	FZ	C	0.94	L
14	Epi	C	0.96	H
15	FZ	C	0.96	H

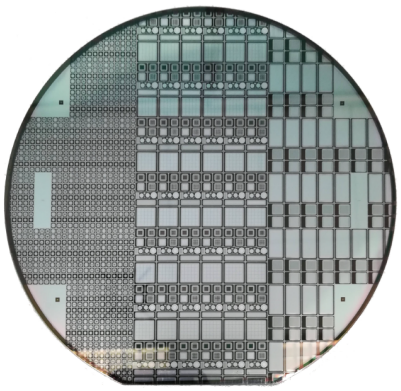

Figure 2.6: Split table of the process parameters for the RSD 1 production (*left*) and picture of one wafer after the manufacture (*right*). Since the RSD 1 production is based on FBK proprietary technologies, the manufacturer is not able to disclose some details about the RSD production process.

2.2 The First RSD Production

The RSD 1 production was released in June 2019. It was designed with the aim of exploring the manufacturing technology and various parameters of the sensors such as gain, the resistivity of the $n+$ layer and the disposition of the pads. It consists of 15 6" wafers fabricated through the step-by-step (stepper) technology on Epitaxial (Epi) and Float Zone (FZ) substrates, both with 50 µm-thick active region. The difference between the two resides in the bulk resistivity, respectively > 3 kΩ and > 1 Ω. Different splits of $n+$ dose have been implemented, as well as the $p+$ dose of the gain layer. The table on the left of Fig. 2.6 reports a summary of the different parameters employed for this production, where the incrementing letters in the $n+$ column correspond to an increment in dose, and the $p+$ dose is expressed as a function of a nominal dose. Finally, the last column describes the thickness of the oxide, which has been tried in two different versions to explore the pads coupling capacitance: high (H) and low (L) thickness.

The RSD 1 wafer has been split into three regions with different layouts, as visible in Figure 2.6 (right). The leftmost region was dedicated to the study of small devices with squared metal pad matrices, each with a pitch varying from 50 to 300 µm and various pad sizes. In the central sector, have been placed larger devices with pitch equal to 500 µm and 1.3 mm, and a strip sensor with long rectangular pads. Finally, the rightmost part includes other strip sensors suitable for the MoveIt project and a 64x64 pixel matrix with 50 µm-pitch designed to match the CHIPX65 [43]. The quality of the production was tested with both static and dynamic measurements (see Chapter 3 for a description of the methodologies and setups employed).

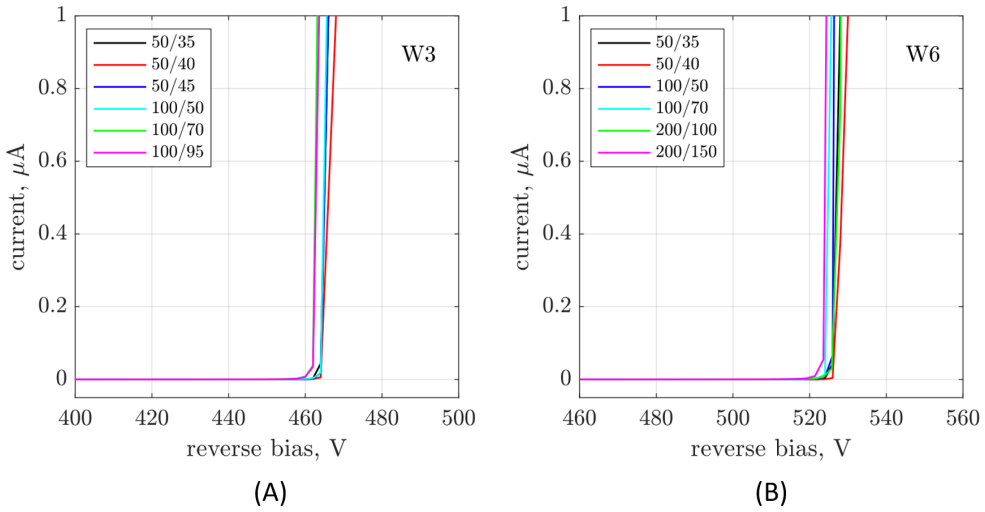

Figure 2.7: Examples of *I(V)* curves of wafer 3 (A) and wafer 6 (B) measured on RSD1 devices. The devices tested have different dispositions of the pads, with the pitch/side shown on the label. The devices come from various positions on the wafer, proving a great homogeneity of the breakdown voltage V_{bd} and, therefore, of the gain layer implant within the wafer. The Figure was taken from [44].

2.2.1 Static characterization

When the RSD1 production was released, intensive tests were performed on a large subset of devices from all 15 wafers. Current-Voltage (*I(V)* and Capacitance-Voltage (*C(V)*) measurements were carried out both on-wafer in the FBK quality assessment department and in the Turin Laboratory after the devices singularization.

The *I(V)* curves provide useful information on the leakage current characteristics of the devices, such as the gain implant uniformity and the bias regions where these devices are operable. In Figure 2.7 are illustrated two examples of the current-voltage data collected on the devices coming from various random positions of two different wafers. All the tested sensors show a breakdown voltage V_{bd} with a spread of a few volts and, therefore, indicate a very good uniformity of the gain implant across each wafer. Moreover, these results prove the independency of the V_{bd} on the geometrical layout of the sensors. The *C(V)* measurements are used to inspect the diode implants. Other capacitance measurements performed include the AC pad and the AC-AC interpad capacitances, to evaluate the RC characteristics of the RSD1 devices tested. In Figure 2.8 (A) are reported the *C(V)* curves measured on W13 various devices. The curves arrange themself in three families that reflect the dimensions of the active volume, as expected. It should be noted that the value of bias voltage for which the curves reach the low-capacitance plateau is very uniform and indicates once again a high level of homogeneity in the gain implant among the same wafer. Uniformity between wafers with the same gain implant is explored in Fig. 2.8, whose *C(V)* were measured on devices with the same pitch coming from wafers 2 and 3 and prove the uniformity of the gain implant in between wafers. The current-voltage characteristics of the wafers 11, 12, 13 and 15 were tested

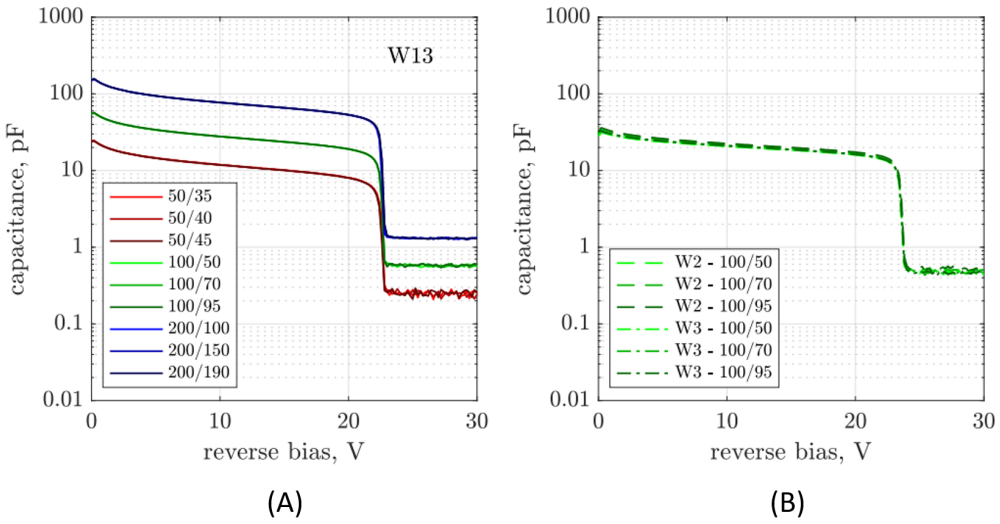

Figure 2.8: *C(V)* characteristics of various devices with different pad pitch/lateral dimensions coming from random positions on wafers 13 (A), W2 and W3 (B). The Figure was taken from [44].

with the same procedure, leading to results similar to what has already been reported. Further measurements include the AC-pads capacitance, measured in full depletion conditions and resulting to be in the capacitance interval between 3.4 pF and 14.25 pF, depending on the pad area and the dielectric thickness. Finally, it was measured the pad-to-pad capacitance (AC-AC) in two wafers with different dielectric thicknesses (W3 and W4) on devices with 300x300 μm^2 active area and as a function of the distances between the AC-pads. Also in this case the measurements are performed on depleted sensors and lead to values in the order of 0.1-2 pF. The interpad capacitance increases with the decrease of the interpad distance and is almost double in the case of the low dielectric thickness. For more information on these matters, see [44].

In the following sections, the dynamic characterization of the RSD1 devices is described. The information on these tests and their analysis was taken from [45, 46, 47].

2.2.2 Reconstruction Models

The dynamic characterization was first performed in the Turin Laboratory with a TCT setup to study the signal propagation on the resistive layer and establish the correct way to model the spatial and temporal resolutions of the RSD. Three approaches have been implemented: the Logarithmic Attenuation (LogA) model, the Linear attenuation (LinA) model and the Discretized Positioning Circuit (DPC).

- **Logarithmic attenuation model**
  It is obtained by comparing the RSD signal division as the one of a current divider of Eq. 2.1 and taking into consideration the spatial extension of the AC-pads. The situation is shown in Figure 2.9, where

an external stimulus travels to the electrodes splitting according to the relative impedances to the various pads. Therefore one obtains that the resistance R_i seen by the signal does not scale linearly with the distance r, but it depends also on the angle of view as

$$R(r) \propto \rho_{n^+} \frac{dr}{r\alpha}, \tag{2.2}$$

being ρ the $n+$ resistivity in Ω/m. This expression is then integrated over the distance obtaining that the fraction f_i of the total signal amplitude that reaches a certain pad i is

$$f_i(\alpha_i, d_i) = \frac{\frac{\alpha_i}{ln(d_i/d_0)}}{\sum_1^N \frac{\alpha_i}{ln(d_i/d_0)}}, \tag{2.3}$$

where d_i is the distance to the pad, $d_0 = 1$ µm is set considering the lateral extent of delta rays and ionization, d_i is the distance between the centre of the pad and the hit point and N is the number of the pads. Furthermore, the signal delay due to the resistivity has the same dependence on the impedance and capacitance of the system. The delay then depends on the distance between the pad and the impact point d and the angle of view α

$$t(t, \alpha) = t_0 + \gamma \frac{ln(d/d_0)}{\alpha} \tag{2.4}$$

where t_0 is the hit time and γ a delay factor that can be extracted from the experimental data.

- **Linear attenuation model**:
  The second model is based on a linear attenuation of the signal with the distance between the hit position and pad d_i and increases with the angle of view α_i. hence

$$f_i(d_i, \alpha_i) = \frac{\alpha_i[1 - \beta d_i]}{\sum_i^N (1 - \beta d_i)}, \tag{2.5}$$

  where f_i is the fraction of the signal amplitude collected by the pad i, N is the total number of the pads and the factor β is a tunable parameter determined experimentally to fit the data. As before, also the time delay depends linearly on the impact position,

$$t(d) = t_0 + \eta d \tag{2.6}$$

  being η a delay factor obtained from the data.

- **Discredized Positioning Circuit**:
  commonly used in Silicon Photo-Multiplier arrays (SiPM), is based on the assumption that the RSD interpad region acts as a resistive sheet with four pick-up nodes, the electrodes. It reconstructs the hit position employing a charge imbalance equation through which is possible to obtain the single coordinates with no prior assumptions on the sharing law. Further description of this model is given in 4.4.

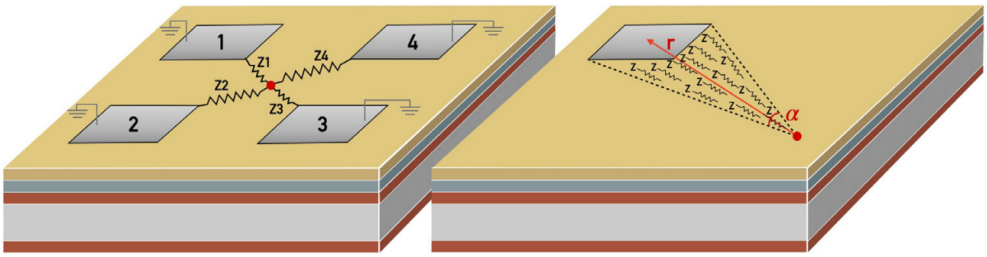

Figure 2.9: Depiction of the signal propagating on the resistive layer of an RSD detector.

These three models can then be applied to the data gathered and tuned on the specific sensor design. To do so, the fractions of the total amplitude $(f_i)_{exp} = A_i/A_{tot}$, with $A_{tot} = \sum_i A_i$ and the single A_i greater than a certain threshold, are compared with the ones predicted. The final coordinate prediction is obtained through the minimization of the following chi-square

$$\chi^2 = \sum_i [(f_i)_{exp} - (f_i)_{pred}]^2 \tag{2.7}$$

2.2.3 Dynamic Characterization

The RSD1 dynamic characterization took place both in the Turin Laboratory on a picosecond TCT setup, and in Fermi National Accelerator Laboratories (FNAL) with 120 GeV/c protons and an accurate tracking system. In Turin, it was possible to test a broader set of devices, confront the reconstruction techniques and measure the time jitter of the system. The best-performing devices were then brought to FNAL to be tested with particles and their performances were measured in a scenario closer to their final target. A thorough description of these tests can be found in [45].

2.2.4 TCT Measurements

The Transient Current Technique (TCT) by Particulars described in Section 3.4 was used to conduct the first studies on the properties of RSD 1 sensors. The intensity of the laser was adjusted to replicate the ionization produced by 1 MIP in a PiN sensor of similar thickness. The measurements were only taken with wafers with the highest resistivity and coupling capacitance to reduce the ballistic deficit. Various matrices were tested, with different pitches and lateral sizes, biased at reverse voltages spanning between a corresponding gain of 8 and 25. The laser was shot in multiple coordinates among the pads and the signals of the four closest pads were collected and registered with a 40 GS/s, 4 GHz bandwidth oscilloscope. Finally, the spatial resolution results from a gaussian fit of the differences between the reconstructed positions and the ones recorded by the moving stages. It should be noted that only the positions in between the four AC-pads, i.e. inside the blue square in Figure 2.10, were taken into consideration since only in these cases at least four electrodes are involved in the reconstruction.

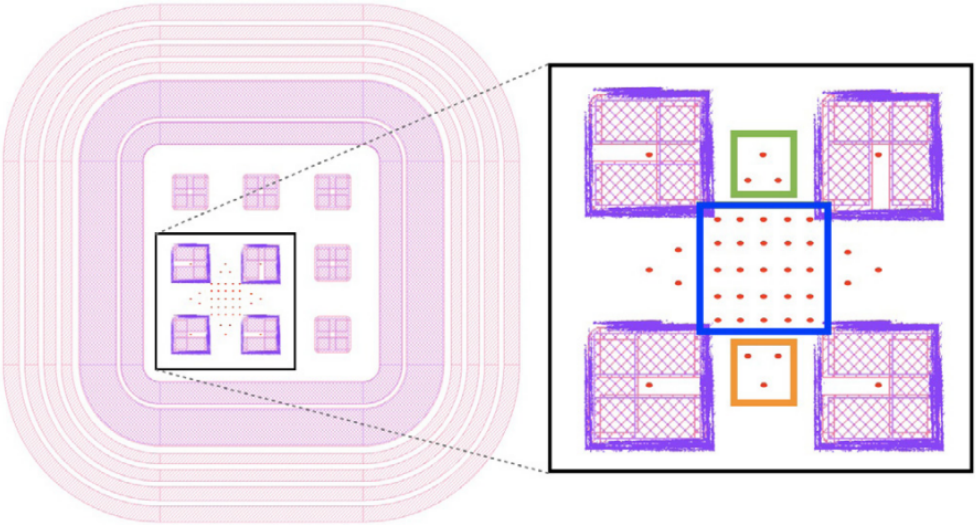

Figure 2.10: Laser positions (red dots) on the RSD1 100-200 pad measured in the TCT set-up.

TCT Spatial Resolution

The results of the TCT data analysis allowed for calibrating the models' parameters. Both the free parameters β from Equation 2.5 and η from Equation 2.6 result in having a logarithmic dependence on the interpad distance when optimised. This demonstrates that the attenuation is logarithmic with distance, as implemented in the LogA model. The resolution improves with higher amplitudes, in particular in larger devices with larger pitch. For small geometries, the resolution remains almost constant in a large range of amplitudes, showing that the performances are excellent even for low RSD gain. All three models achieve similar results in terms of spatial resolution over small distances, while the LinA and DPC method performs better over longer propagation surfaces. The poorer LogA resolution in these instances suggests that its assumption for which the area over which the signal propagates is triangular does not hold over long distances, as visible in Figure 2.11. The unprecedented spatial resolution for devices with these pitches is reported in this Figure, less than 5 µm for the devices for the smaller interpad distances. A complete description of the spatial resolution parametrization can be found in Section 4.2 and it holds for the RSD1 production.

Temporal Jitter

In a TCT setup, the Landau term of the temporal resolution is not present (see Section 4.4.5). For this reason, the time resolution reported in this paragraph equals to the time jitter of the device. The measurement of the time coordinate consists of a two-step procedure:

- first, the time measured in each pad is corrected for the propagation delay employing Equation 2.4 from the hit position to the metal

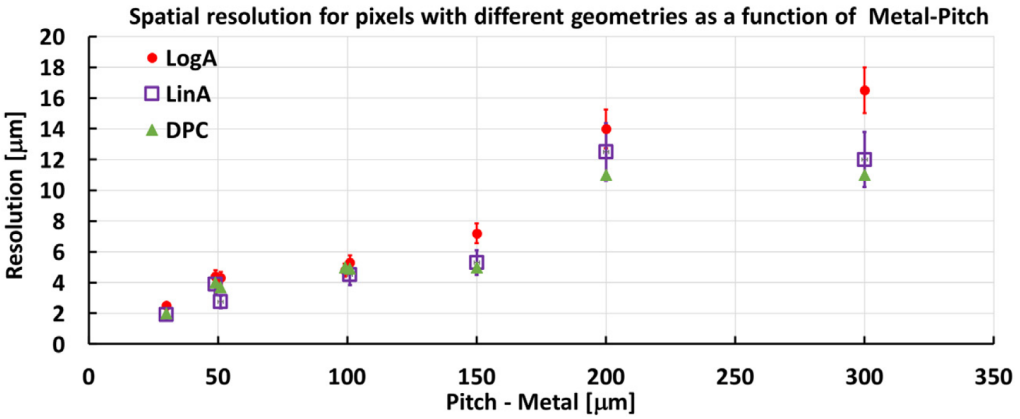

Figure 2.11: spatial resolution obtained with the three different models as a function of the pitch of the devices. The Figure was taken from [45].

edge. The delay parameter contained in this equation was estimated on sensors from the same wafer by varying it and by minimizing the obtained time resolution for different ratios of metal pad extension and sensor pitch. An optimized delay parameter depends linearly on the $(metal/pitch)^2$ ratio, confirming that the geometrical layout of the system plays a role in the delay, and not just the $n+$ resistivity.

- secondly, the time of the event is obtained as the amplitude-weighted average of the single read-out pads.

The temporal resolution is then acquired from a gaussian fit of the $t_{reconstructed} - t_{trigger}$ distribution. The single channels achieve a time resolution of $\sim$ 45 ps, while the combination of multiple pads allows reaching $\sim$ 22 ps, as expected assuming the channels are uncorrelated (45 ps/$\sqrt{4} \sim$ 22 ps). Figure 2.12 shows the results obtained for wafer 2 as a function of the metal pitch (interpad distance). The time resolution increases from the $\sim$ 15 ps of the smaller pitch devices up to $\sim$ ps for the larger ones, showing how the LGAD timing capabilities are maintained in these devices.

A summary of both spatial and temporal resolutions obtained with the TCT setup is reported in Table 2.1.

Test Beam at FNAL

Two matrices from wafer 2 with 100-200 and 190-200 metal pad-pitch were tested at the MTest Beam Facility at FNAL with high-energy protons. This facility is equipped with a tracking system [48] capable of measuring the track position with $\sim$ 45 µm resolution at the time of the data acquisition. The beam is composed of 120 GeV/c protons supplied every minute in 4 s spills, each containing 50-100k particles. The RSD Devices Under Test (DUTs) were wire-bonded on 16-ch Fermilab readout board described in Section 3.5 with a double-stage amplifier based on the GALI-66+ integrated circuit. The boards were mounted on cooling blocks able to maintain a stable temperature equal to (22 $\pm$ 0.1) °C and kept inside an box to maintain a low level of background light. Additionally, the setup was instrumented

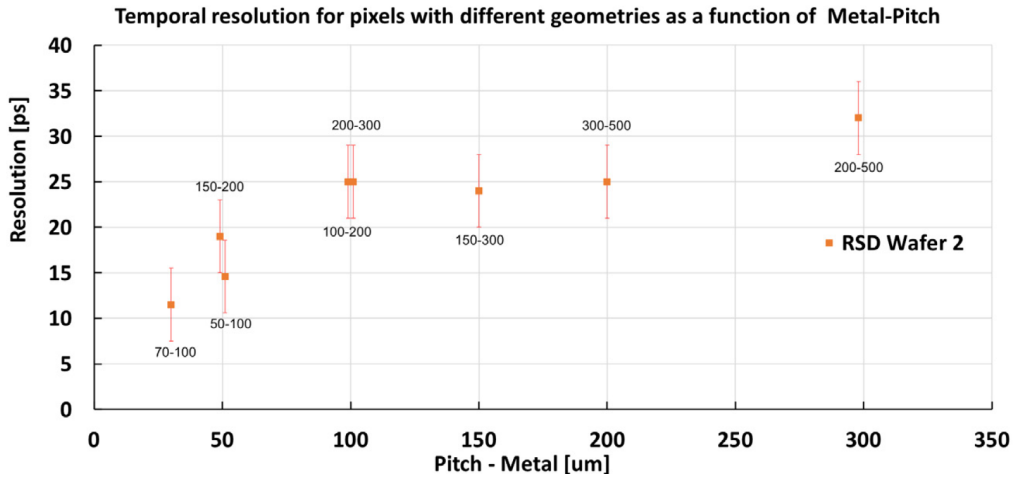

Figure 2.12: TCT time resolution of the devices from RSD1 wafer 2 as a function of the interpad distance.

Pad-pitch geometry	Spatial Resolution [µm]	Temporal jitter [ps]
50-100	4.3	14.7
70-100	2.5	11.5
100-200	4.8	25
150-200	4.4	19
150-300	7.2	24
200-300	5.3	25
50-500	16.5	32
50-500	14	25

Table 2.1: Spatial and temporal resolutions measured with the Turin TCT setup for various RSD1 geometries. The pad-pitch column refers to the metal pad extension and the pitch, i.e. the distance between the centres of two neighbouring pads (both in µm). The results are obtained in the interpad region shown in blue in Figure 2.10.

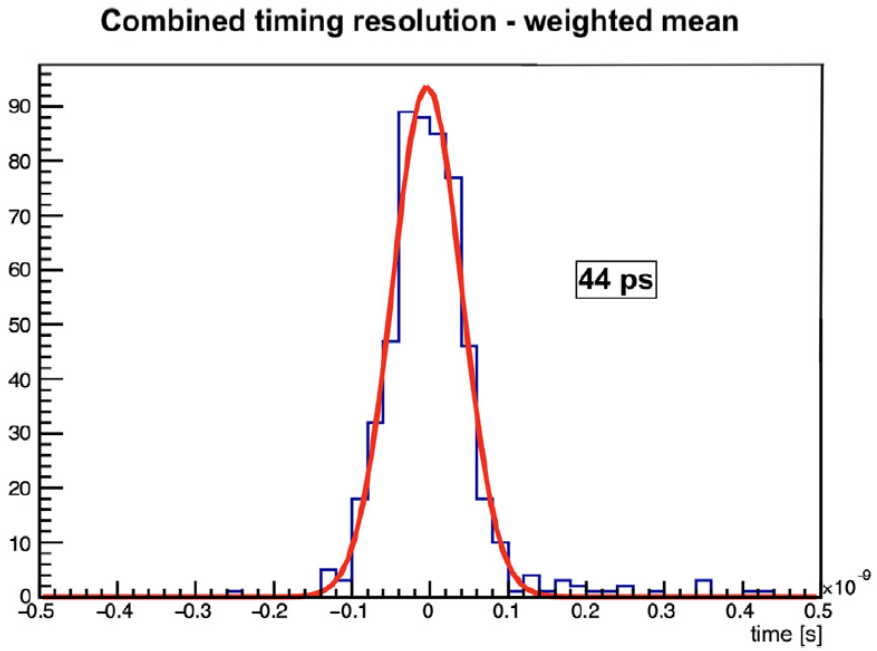

Figure 2.13: Time resolution obtained with the amplitude-weighted mean on 3 pads of a 100-200 detector from wafer 2 at the Fermilab Test Beam Facility. The plot was taken from [50]

with a Photek 240 micro-channel plate device with time resolution ¡ 10 ps [49]. All data was acquired with a Keysight MSOX92004 A 4-channels digital oscilloscope with 40 GS/s and 20 GHz analog bandwidth, limited to 2 GHz for this data acquisition. Given the limited number of channels, three different configurations were chosen to explore (i) the spatial resolution with 4 AC-pads recorded, (ii) the timing resolution where 3 AC-pads and the Photek were measured by the scope, and (iii) two AC-pads, the Photek and the DC-pad to perform studies of the DC signal. Since the total resolution of the tracker+RSD system is dominated by the tracker resolution, it was difficult to infer the RSD spatial capabilities from the runs with the AC-pads read-out. Nonetheless, the position reconstruction was in line with what expected and both the reconstructed x and y were in agreement with the tracker measurements. The time resolution of the 100-200 device measured with 3 pads and the Photek reference yielded to an excellent $\sigma_t = (44 \pm 0.3)$ ps and visible in Figure 2.13, calculated with the amplitude-weighted mean described in the TCT paragraph 2.2.4. The results obtained by combining the signals from the three pads with an arithmetic mean produced worse results due to the correlation introduced by the Landau term. Reguarding the 190-200 device, it was demonstrated that the large metal pads worsen the RSD capabilities. Most of the signals are recorded by only one pad, leading to a more traditional spatial resolution of $metal\,size/\sqrt{12} \sim 55\,\mu$m, but with the benefit of the 100 % intrinsic fill factor proper of the resistive design and no pads segmentation. Its temporal resolution for the events that involve a single pad is $\sigma_t = (32 \pm 1)$ ps, and $\sigma_t = (42.1 \pm 0.6)$ ps if

the pads receiving a signal is greater than one. The studies on the DC-signal reported that it cannot be employed to do time measurements if the hit falls in between pads since its fast component is absorbed by the AC-pads. This behaviour was already observed in the Laboratory with the TCT setup measurements. It was also possible to extract the RC constant from the signal discharge. For more information on these topics see [45].

The results obtained with the TCT setup and with protons proved the RSD concept. Unprecedented time and space resolutions were achieved on large devices with low number of channels. At the same time, the impossibility to exploit the charge sharing over the whole device and the large metal pads studies showed areas of improvement that would be implemented in a future batch.

Machine Learning studies

Another possible approach to spatial reconstruction in RSDs consists in exploiting the capabilities of the nowadays broadly applied Machine Learning (ML) techniques. The reconstruction algorithm models described in the previous Section 2.2.4 use only amplitudes of the signals collected on the AC-pads, but they cannot employ extra signal features due to their inaccurate analytical dependence on the spatial coordinates. A multivariate analysis, on the other hand, can combine this information leading to more accurate results. The application of ML techniques to the RSD1 datasets is extensively described in [47], here is reported a summary of the techniques employed and the results obtained to allow a comparison with the analytical method and future work on the next RSD production. The reconstruction of the hit position was made possible by a Multi-Output Regressor algorithm [51], using a Gradient Boosting Regressor as an estimator, which was trained and applied to the data. Gradient Boosting (GB) [52] consists of a technique used in regression and classification tasks. A set of N variables are selected to define an input vector $\vec{x} = (x_1, x_2, ..., x_N)$ that identifies a given event i. For each set $\vec{x_i}$, an output scalar y_i is produced and the objective of the GB is to find a function $F(\vec{x_i})$ such that

$$F(\vec{x_i}) = y_i, \ \forall i \in [1, n]. \tag{2.8}$$

GB is also defined as a weak learning algorithm since it employs the residual function $h(\vec{x_i}) = y_i - F(\vec{x_i})$ and progressively reduces it to find the best estimate for F. In our case, the index i runs over the number of the event recorded and the algorithm can smooth the function F a certain m number of times (depth of the algorithm), i.e.

$$F_m(\vec{x_i}) = F_{m-1}(\vec{x_i}) + h_m(\vec{x_i}) = y_i. \tag{2.9}$$

The initial value F_0 is usually a constant, from which derives the equation

$$F_m(\vec{x_i}) = F_0 + \sum_{j=1}^{n} h_j(\vec{x_i}) = y_i \tag{2.10}$$

which manifests the sequential nature of the algorithm. In the case of the RSD dataset the scalars to be predicted are the two coordinates, so two

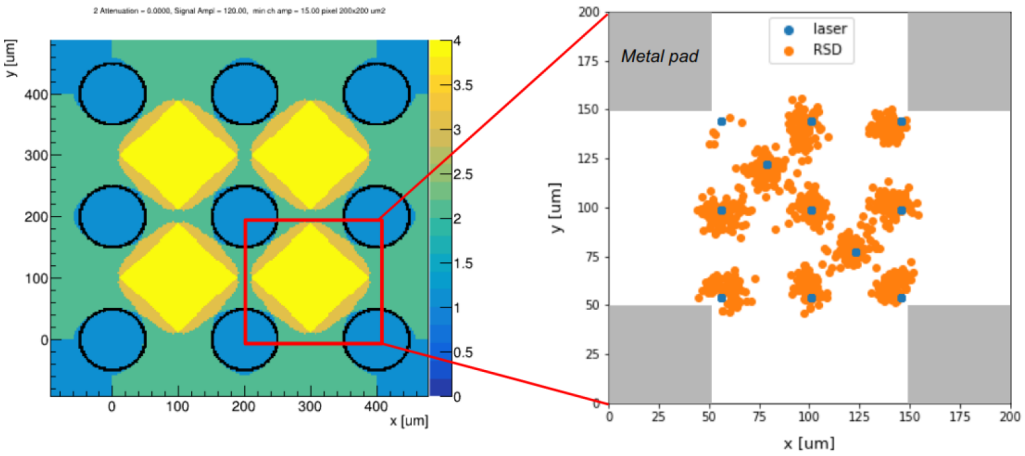

Figure 2.14: 2D map of the DUT pad arrengement (*left*) and the shot and reconstructed positions (*right*).

single predictive models are trained on the same datasets and their combination constitutes a bigger model able to predict the event location over a 2D surface. In the case of the RSD DUTs, the Multi-Output Regressor was trained with 8 input variables, the 4 amplitudes A_i of each pad i and their relative fraction with respect to the total amplitude A_{tot}, with 100 boosting stages. The maximum depth of the individual regressors was set to 8, with a learning rate of 0.1, whereas larger values would cause overfitting of the data. After a first tuning phase on simulation data, the model was trained on the TCT data described in the previous section of this chapter, since the tracker of the Fermilab Test Beam Facility had a resolution too poor for the RSD studies at the time of the measurements, while the laser position error is quite small ($\sim$ 2 µm). Multiple laser events were induced in the sensors in the positions shown in 2.14.

The final resolution reported in Figure 2.15 is obtained by subtracting in quadrature the uncertainty of the laser positioning $\sigma_{TCT} = 2$ µm

$$\sigma_{RSD} = \sqrt{\sigma^2_{meas} - \sigma^2_{TCT}}. \tag{2.11}$$

In order for the algorithm to be fully efficient, a fiducial region was defined in between the AC-pads similar to the one employed for the analytical approach (Figure 2.10). Furthermore, only events with at least 3 signals with amplitude over a certain threshold were taken into consideration. The final results are reported in Figure 2.15, showing a spatial resolution in the range 2 µm and 10 µm, depending on the sensor interpad. The Multi-Output Regressor achieves an overall better resolution than all analytical methods, even if it uses a limited set of input features. It should be noted that the training dataset is limited to certain points on the detector surface and the use of a more ample positions array would allow for validating of the results at a higher degree.

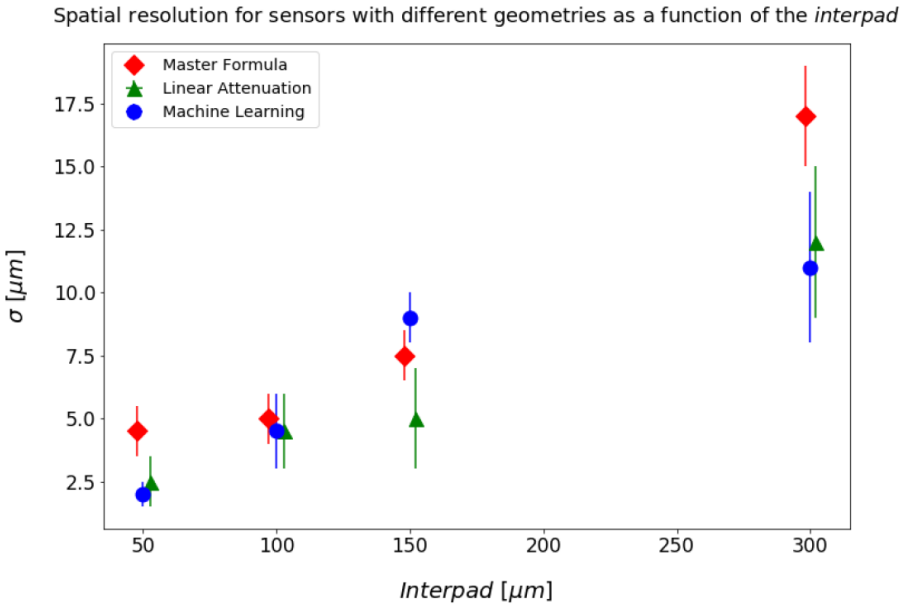

Figure 2.15: Comparison between the results obtained with the ML technique, the Master Formula (LogA) and the Linear Attenuation model (LinA).

2.2.5 Design Optimization

The simulations, and the results acquired both with the TCT and the FNAL proton beam indicate that the RSD1 production can be improved to yield better results over the whole surface of the devices. Optimising the signal sharing is fundamental in the development of RSDs: the geometrical layout of the metal pads defines how the signal splits among the different electrodes and determines if it is circumscribed in a determined region of space. An example is brought in Figure 2.16: the pads disposition typical of the RSD1 production yields a noticeable amount of regions of the area of the device in which the signal is split among two pads, worsening its spatial resolution capabilities. Moreover, the metal pad dimensions generate ambiguous readings between each other, where just two of them participate in the event reconstruction and make it impossible to infer both the x and y coordinates simultaneously (in green in Fig. 2.16, *left*). A possible design that addresses this issue is shown on the *right* of Figure 2.16 by arranging the pads differently and maintaining the angle of view of each hit large enough. Another drawback of large metal pads consists in the absence of sharing when a stimulus hits the metal pad, which renders that region of the sensor approximable to a traditional pixellated detector with resolution $\sigma_{pos} = (metal\ pitch)/\sqrt{12}$. The foreseen solution to this consists of eliminating the concept of a squared pad and trying different thin layouts in the next productions. From these considerations, a new RSD production was designed and manufactured by Fondazione Bruno Kessler (FBK): RSD2.

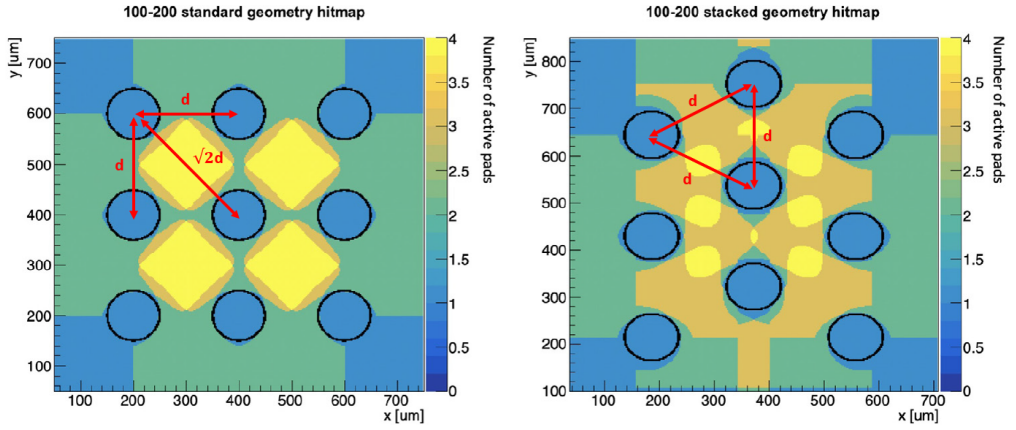

Figure 2.16: Heat maps representing how many AC-pads collect a significant signal for a given hit position. The 2D on the *left* depicts a typical RSD1 layout with 200 µm pitch and 100 µm large pads disposed at the vertexes of a grid. The modified layout (*right*) increases the area over which at least 3 pads are involved in the reconstruction.

2.3 The Second RSD Production

In the previous section 2.2, it was shown that choosing the right manufacturing parameters allowed producing a functioning Resistive Silicon Detector. Among these, of particular importance are the resistance of the resistive sheet R_{sheet}, directly dependant on the $n+$ dose, the coupling capacitance, determined by the dielectric oxide and the extension of the metal pads, and the p-gain implantation dose, which defines the gain of the LGAD device at a certain bias voltage. The optimization of these parameters brought to a second production of AC-coupled RSD, the RSD2 batch. It consists of 15 p-type 6" wafers processed in FBK with both epitaxial and float zone (Si-Si) substrates, 45 and 55 µm-thick respectively with improved pads geometry for signal sharing. Table 2.2 contains information on each wafer composition in terms of

- the substrate;
- the presence of Carbon in the gain implant;
- the dose of the $n+$ implant, where A < B < C, leading to higher resistivity values for the A wafers. Overall the RSD2 $n+$ resistivity is slightly lower than the one of the RSD1 batch;
- the p-gain dose, slightly increased with respect of the RSD1 production.

The dielectric thickness has been kept as the thin version of the RSD1 batch, which produced the best results. Fundamental in the RSD2 production is the advancement in the pad arrangement and geometries to improve signal sharing and, therefore, the performances in terms of spatial resolution

Wafer #	Type	Carbon	n^+ dose	p gain dose
1	FZ 55 µm	N	A	0.96
2	FZ 55 µm	N	A	0.96
3	FZ 55 µm	N	A	0.98
4	FZ 55 µm	N	A	1
5	FZ 55 µm	N	A	1
6	Epi 45 µm	N	B	1
7	FZ 55 µm	N	B	0.98
8	Epi 45 µm	N	B	0.96
9	Epi 45 µm	N	B	0.96
10	Epi 45 µm	Y (1)	B	0.96
11	Epi 45 µm	N	C	0.96
12	Epi 45 µm	Y (0.8)	C	0.96
13	FZ 55 µm	N	C	0.98
14	Epi 45 µm	N	C	0.98
15	FZ 55 µm	N	C	0.94

Table 2.2: RSD 2 split table. All units are arbitrary.

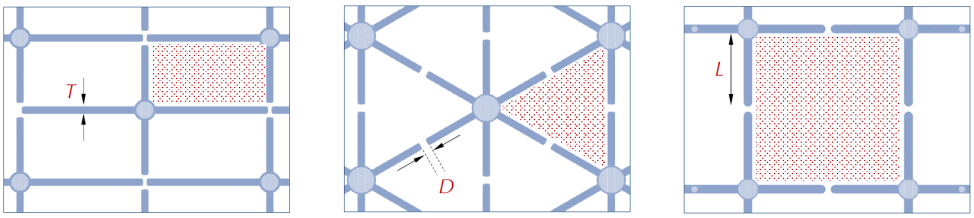

Figure 2.17: Layout of the geometries designed for the RSD2 production. T, L and D indicate the thickness, length and distance between the arms of the crosses, respectively. Various dispositions of the cross pads have been implemented: asymmetrical arms (*left*), star-pads (*centre*) and squared (*right*). Image is taken from [53].

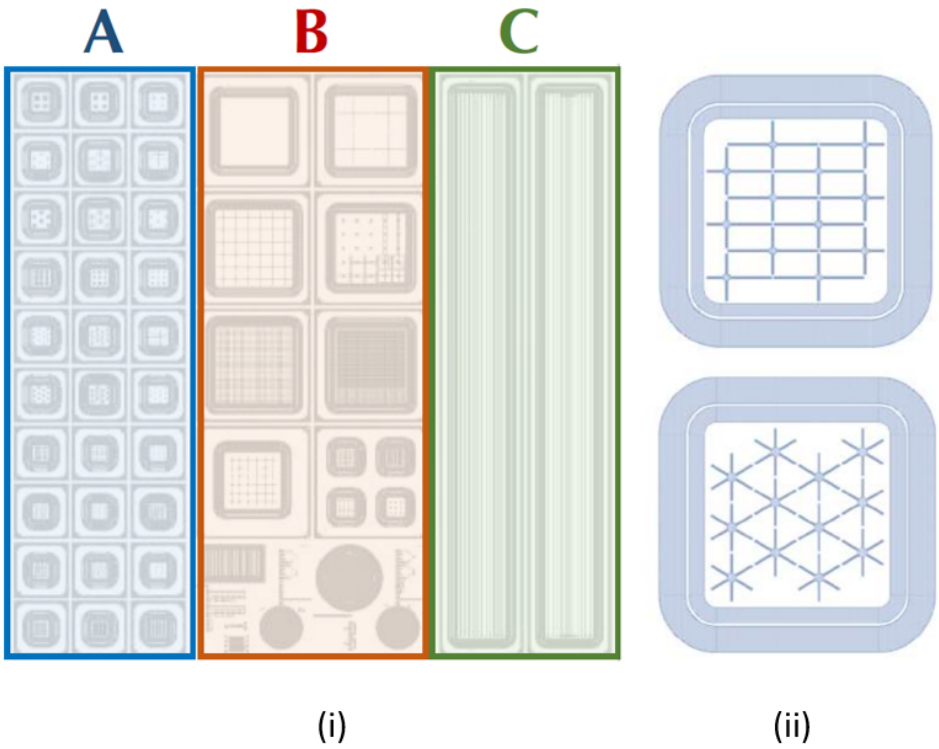

.

Figure 2.18: Depiction of the RSD2 wafer layout (*i*) divided into its three regions and two examples of full sensor layout (*ii*

over the sensor surface. One of the new pads dispositions aims at reaching the most homogeneous response throughout the sensor active area by arranging the pads at the vertexes of equilateral triangles (Figure 2.17, *centre*). Other layouts have been included to reproduce the effect of the squared pads in the RSD1 batch but with the prevention of the total absorption of the signal. In Figure 2.17 (*left* and *right*) are reported cross-shaped pads with orthogonal arms and, respectively, asymmetrical arms length and a simpler disposition that can compose an array. Other parameters that vary in this batch are the cross dimensions. As visible in the same Figure, the distance D between the crosses, the length of the arms L and their thickness T are tried in different variations. The RSD2 production is composed of three different regions on the wafer in which are present different devices and structures: (i) the region "A" is dedicated to the study of multiple variations in pad disposition, dimensions and geometry over small distances over 800x800 µm^2 active area, i.e. the area covered by the gain layer; (ii) in the "B" region the active area gets larger and covers 2.6x2.6 mm^2 and its devices are dedicated to studies of signal sharing among multiple pads among longer distances (and test structures, in the bottom); (iii) the last part of the wafer presents very large strip sensors, 20 x 1.7 mm^2 with 75 µm and 150 µm pitch. Examples of the structures are gathered in Figure 2.18.

This Chapter presented the first steps taken into the field of Resistive

Silicon Detectors and the difference between the two types of them that were devised in the last period: AC- and DC-coupled RSD. Furthermore, the results achieved with the first production of AC-coupled RSDs proved the validity of this concept and served as a stepping stone for the development of the second production of RSD detectors. The results of the static and dynamic characterization of the devices from this batch are reported in Chapter 4. The next Chapter describes the experimental methods employed to measure such characteristics. Finally, a future evolution of the RSD design is the DC-coupled RSD, which incorporates the expertise gained with the study of the RSD1 and RSD2 batches. The simulations and the layout of the future DC-RSD production is described in the last Chapter of this work, Chapter 5.

Chapter 3

Experimental Techniques

The experimental characterization of LGAD is a fundamental portion of innovative detector development. In this chapter, the most common experimental techniques employed to extrapolate the behaviour of silicon sensors are described. Particular focus is given to setups whose role is referred to in the following chapters.

3.1 Static Characterization

Static characterization of silicon sensors consists of measurement of the current-voltage *I(V)*, capacitance-voltage *C(V)*, and capacitance frequency *C(f)* in the absence of external particle (or particle-like) stimuli. The Torino Laboratory for Innovative Silicon Sensors (LISS) is equipped with two probe stations connected with a low-noise Keysight B1505 curve tracer analyzer visible on the right of Fig. 3.1. The Device-Under-Test (DUT) is positioned on a support, called chuck, on which it is kept still by a vacuum system. The metallic contacts on the sensor's surface are then located via an optical microscope equipped with different magnification lenses and a video camera able to project its field of view on a monitor. Once the DUT is correctly positioned on the chuck, the electrical contacts are provided by tungsten-rhenium needles placed in the correct position thanks to manipulators moved with micrometric screws, visible on the left of Fig. 3.1. Chuck and needles are connected to the different modules inside the Keysight device analyzer through triaxial cables to provide low noise measures. Since the sensors are n-in-p, they are biased by providing a negative voltage to the chuck, and the needles are set to zero voltage. The Keysight power device analyzers are equipped with different modules that provide various functionalities:

- the High Voltage Source Monitor Unit B1513C (HV-SMU) is able to provide voltage differences between 1 V and 3000 V, with a maximum current of 8 mA;

- the Medium Power Source Monitor B1511B (MP-SMU) has a range of 100 V/0.1 A and a minimum measurement resolution of 10 fA/0.5 µV;

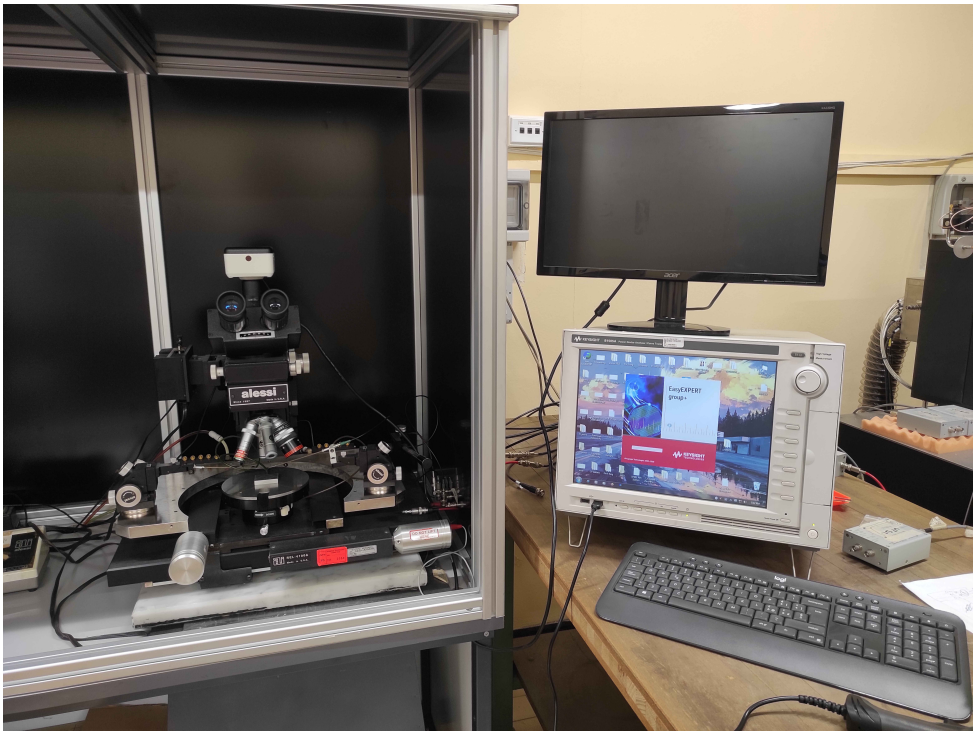

Figure 3.1: Picture of the setup employed in the static characterization of the DUTs composed of a Keysight B1505 analyser (*right*) and a probe station by Alessi (*left*).

- the Multi-Frequency Capacitance Measurement Unit (MF-CMU), able to issue different AC-signal amplitudes (0-250 mV) at different frequencies (1 kHz-5 MHz).

3.2 Current-Voltage *I(V)* Characteristics Measurement

A steady current flows through the device when a *pn* junction is biased reversely. Such *leakage* or *dark* current is present even in the absence of an external stimulus and can be employed to extract features of the device. This leakage current is measured by reverse biasing the sensor, applying a negative voltage to the chuck through the HV-SMU and grounding the pad and the guard-ring with the abovementioned needles as shown in Fig. 3.2. In the case of RSD 2 sensors (see 2.3), the pad contacted to ground corresponds to the one referred to as *DC-ring*. The pad under test is wired to the available MP-SMU since it has a higher current resolution than the HV-SMU. *I(V)* curves carry helpful information about the DUT. They can be exploited to ensure the correct functioning of a sensor since even minor manufacturing imperfections lead to noticeable differences between various sensors.

Figure 3.3 shows the typical shape of a *I(V)* characteristics of a PiN (dashed line) diode and of a UFSD (solid).

The UFSD curve presents a first knee at low bias voltage due to the depletion of its gain layer, related to the gain layer profile. Over this value,

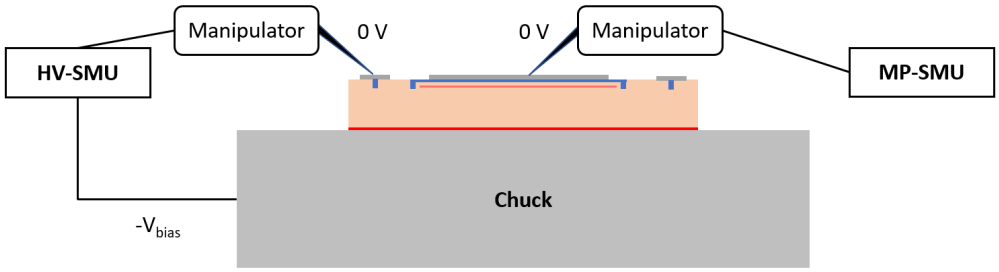

Figure 3.2: Schematic representation of the connections between probe station modules and the DUT for current-voltage characteristic measurement.

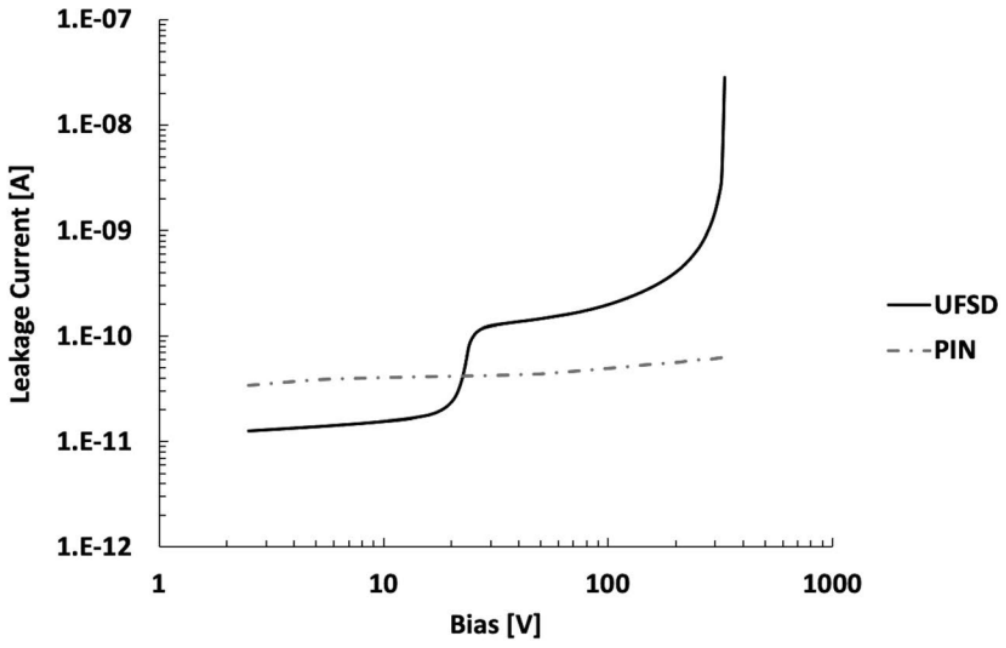

Figure 3.3: I(V) characteristics curve of a PiN (dotted) and an LGAD (solid) diodes.

gain-related effects start to be noticeable as an exponential trend in the plot due to the dependence of leakage current upon the gain. On the other hand, the PiN characteristic in reverse polarization shows an immediate rise to a temperature-dependent plateau value. It remains roughly constant until the eventual breakdown of the sensor.

3.3 Capacitance-Voltage *C(V)* and Capacitance-Frequency *C(f)* Characterization

The characterization of the DUT capacitance as a function of voltage *C(V)* and frequency *C(f)* is an important tool for measuring the features of multi-layer silicon sensors such as UFSDs. The capacitance extraction is carried out considering the sensor as the equivalent of an RC circuit with a resistor in series or in parallel with a capacitor. Both these models have proven good for pre-irradiation devices since the measured impedance Z is due almost exclusively to the sensor capacitance. However, high leakage current in irradiated devices implies that the parallel model resembles the system more accurately. Considering the *pn* junction capacitance as the one of a parallel plate capacitor, its value is inversely proportional to the square root of the bias voltage, i.e. $C \propto \sqrt{\frac{N_A}{V_{bias}}}$. The voltage capacitance extraction V_{depl} depends on the thickness d of the PiN and on the effective acceptors doping concentration $N_{A,eff}$

$$V_{FD} = \frac{qN_{A,eff}}{2\epsilon_{Si}} d^2, \tag{3.1}$$

being ϵ_{Si} the silicon permittivity. Therefore, a *C(V)* curve for a PiN shows the characteristic $\propto 1/\sqrt{V_{bias}}$, shown in black in Figure 3.4. After the depletion voltage, the capacitance becomes constant and can be expressed as $C = \epsilon_{Si}\frac{A}{d}$, as for parallel plate capacitors. The different shape of the LGAD curve (black in Fig. 3.4) can be explained given its multi-junction structure. Identifying two different inflexions corresponding to the full depletion of the sole gain implant and the bulk is possible. Full depletion is obtained when the bias voltage reaches V_{GI} and V_{FD} respectively, where

$$V_{GI} = \frac{qN_{A,eff}}{2\epsilon_{Si}} d_{GI}^2, \tag{3.2}$$

where d_{GL} is the gain layer thickness. Taking into consideration the gap of thickness d between the gain layer and the gain layer itself, the bias needed to fully deplete the sensor until the end of the gain layer V_{GL} becomes the sum of the voltage needed to deplete the gap V_{Gap} and V_{GI}, hence

$$\begin{aligned} V_{Gap} &= E_{Gap} d_{Gap} = 2\frac{qN_{A,eff}}{2\epsilon_{Si}} d_{GI} d_{Gap} \\ V_{GL} &= V_{GI} + V_{Gap} = V_{GI}(1 + 2\frac{d_{Gap}}{d_{GI}}) \end{aligned} \tag{3.3}$$

under the assumption that the doping density is constant where present and absent elsewhere. Therefore, measuring the characteristics of multiple

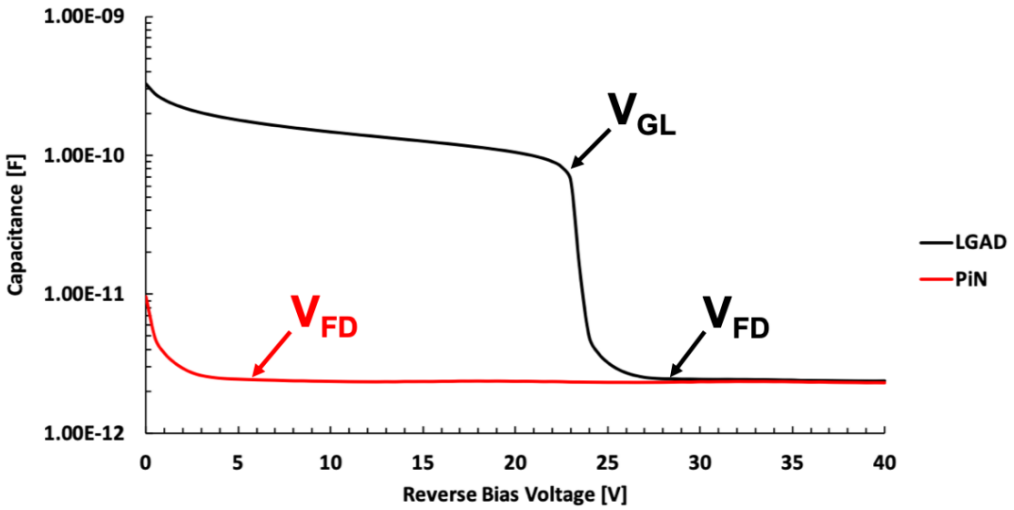

Figure 3.4: *C(V)* characteristic curves of a UFSD (black) and of a PiN sensor. The figure is taken from [39].

devices by measuring the *C(V)* characteristics is a reliable method to probe their gain layer and the differences within the same production batch. It is also possible to investigate the doping density with respect to the depth $d = \frac{A\epsilon_{Si}}{C}$, being C the measured capacitance and A the sensor active area. Then, the doping density profile as a function of depth can be computed with

$$N_A(d) = \frac{2}{q\epsilon_{Si}A^2} \frac{1}{\frac{\partial(1/C^2)}{\partial V}}. \tag{3.4}$$

Finally, the bulk thickness and doping can be extracted from the asymptotic value of the capacitance and Eq. 3.4, respectively.

The setup for *C(V)* measurements is reported in Fig. 3.6. An AC signal is injected on the sensor pad thanks to the MF-SMU module, while the guard ring is grounded (0 V) and the sensor is depleted with a variable bias provided by the HV-SMU module. A capacitance sweep vs frequency (*C(f) curve*) is performed to establish the optimal parameters of the Ac-signal since the sensor acts as a low-pass filter and has frequency-dependant behaviour. The devices are biased in the condition of partial gain layer depletion (V = -10 V) and at room temperature. An optimal test frequency is selected in the region of the curve where the capacitance measurement is constant, usually in the interval 1-5 kHz for UFSD sensors, as shown in Figure 3.5. This value might vary concerning the sensor bulk doping or due to the defects caused by irradiation.

3.4 Transient Current Technique Setup

The Transient Current Technique involves exploiting a laser system to induce a signal in the DUT simulating the passage of a particle [54]. It is widely employed to characterize Silicon detectors, including UFSDs since it allows to produce the signals in very precise locations on the device.

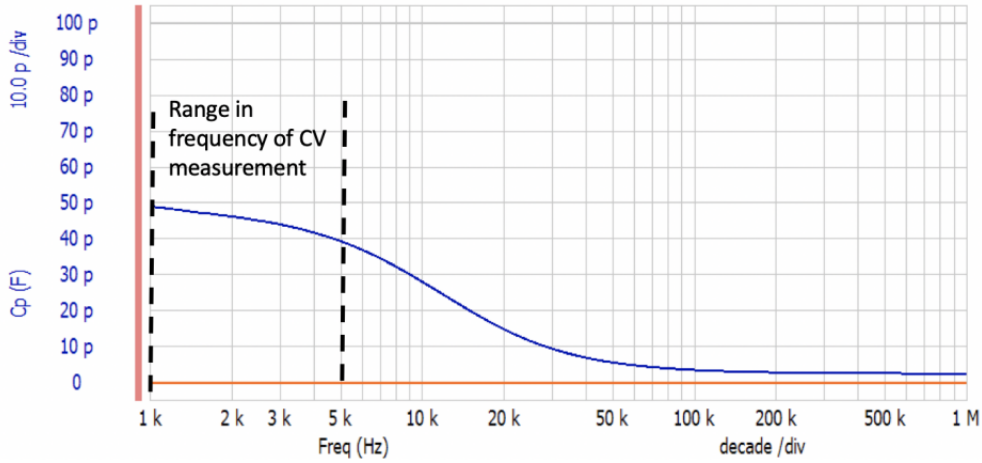

Figure 3.5: Example of a capacitance-frequency characteristics curve.

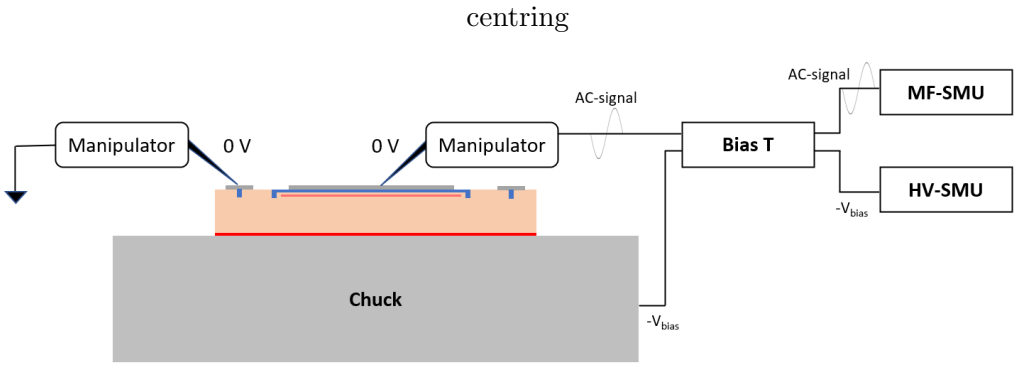

Figure 3.6: Schematic representation of the connections between probe station modules and the DUT for current-voltage characteristic measurement.

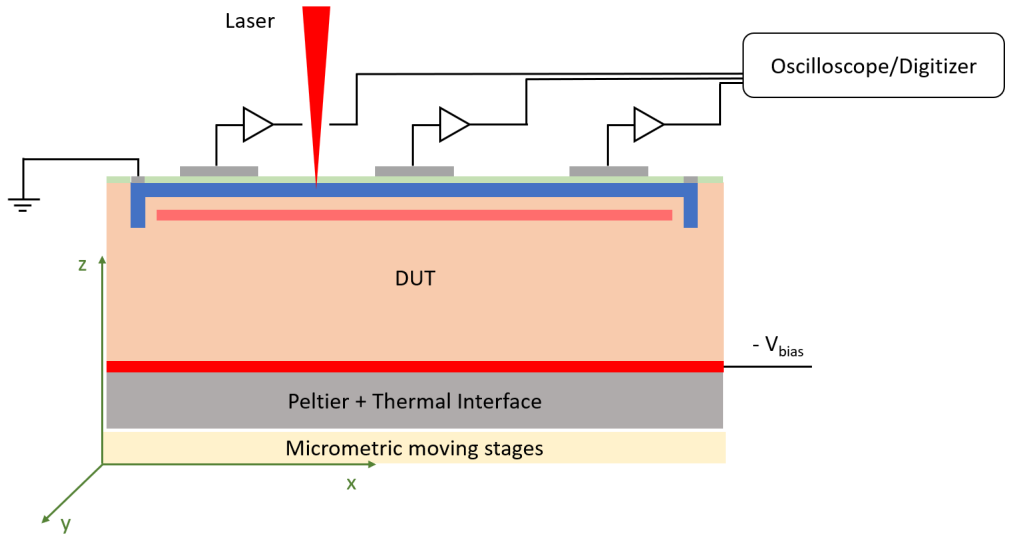

Figure 3.7: Schematic representation of a TCT setup.

The setup employed in this work is assembled by Particulars [55], whose general schematics are reported in Fig. 3.7. Such a measurement system is equipped with a laser that generates *e-h* when it impinges on the DUT, which then drifts towards the electrodes based on their polarities. The time analysis of the current signal that is induced from this flow of charges provides information about the DUT characteristics. The laser intensity can be tuned so that the induced signal produces an amount of charge equal to the most probable value of a MIP. It is important to keep in mind that some differences concerning actual particles are present: (i) the number of *e-h* generated inside the device is constant at a given laser intensity, while that of a MIP follows a Landau distribution; (ii) the laser creates pairs in a cylinder with diameter proportional to its focus on the sensor, while the MIP generates charges in a much smaller volume, resulting in screening effects; (iii) the density of *e-h* pairs is constant along the track when generated by the laser, while is non-uniform along a MIP track. The Turin Laboratory TCT setup was upgraded to host irradiated DUTs thanks to a dedicated cooling system. DUTs and their read-out board are positioned on a Peltier element further cooled by a block connected to a chiller. As a result, temperatures between -25 °C and +80 °C can be achieved consistently in time. The same Peltier controller (Belektronig BTC benchtop) is able to read a PT100 to automatically tune its current draw to keep the temperature at the desired level. Essential for the purpose of this work is this setup capability to accurately move and record the position of the device under the laser beam. The Newport M-ILS100PP translator stage makes it possible to translate the DUT with sub-micrometric precision over a range of ∼10x10 cm^2 along the directions parallel to the DUT plane (x,y). An additional stage controls the z position, i.e. moves the laser's optics in the vertical direction to optimise its focus on the DUT, as described in the next section. The optical system present in this setup allows reaching a laser beam spot size of about 10 µm in a standard scenario. Being most of the sensors tested 20 µm - 100 µm thick, an infrared (1060 nm) fibre-coupled laser with has been chosen taking into consideration the absorption depth in silicon of 1 mm.

Since the DUT under test in the Turin Laboratory are thin UFSDs, the TCT setup needs to be optimized for timing applications: (i) the laser shot duration needs to be ∼ 50-100 ps with repetition rate high enough to ensure a time-efficient data taking (50 Hz - 1 MHz), (ii) a precise time reference with low jitter (around 10 ps) as trigger, (iii) an ideal read-out board should be chosen, described in section 3.5, with high bandwidth (1-2 GHz) and selected gain coupled with (iv) a fast oscilloscope or digitizer with matching bandwidth and input impedance (50 Ω) and a high sampling rate (> 5 GS/s). The Turin TCT setup is provided with a Teledyne-Lecroy HDO9404 oscilloscope with a 20 GS/s sampling rate, 500 MHz-4 GHz bandwidth and 10-bit vertical resolution used to digitize the signals from the DUT and the Trigger [56]. A CAEN DT1471LET 4-channel high voltage able to supply voltages in the range 0 V - ± 5.5 kV and 300 µA maximum current [57] supplies the bias voltage to the boards that host the DUT.

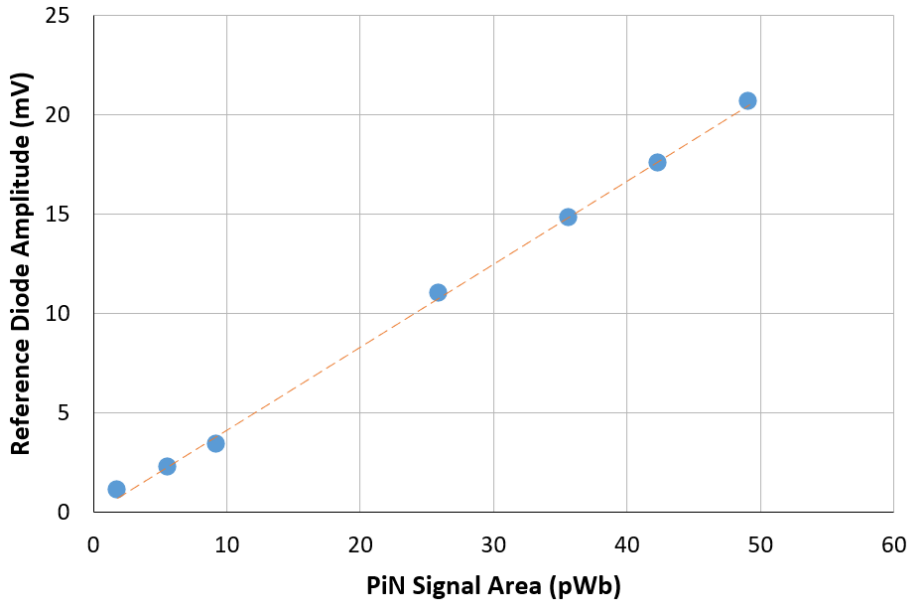

Figure 3.8: Example of a PiN-reference diode calibration curve.

Laser Calibration

It is important to notice that the laser intensity might vary during the measurement. For this reason, a 90 %-10 % optic fiber splitter sends 10 % of the beam to a reference InGaAs diode that monitors eventual fluctuations and allows corrections of the collected charge by a factor extrapolated from a calibration curve, In Figure 3.8 is visible an example of this curve, achieved measuring the collected charge on a 50 µm PiN diode versus the amplitude recorded on the reference diode at different laser intensities. Such is achieved by shooting the laser in a region of the sensor surface with no metalization, after performing the focusing procedure explained in the next section.

The values on the graph in Fig. 3.8 x-axis can be expressed as a multiple of the MPV charge induced in a PiN diode by a MIP. Since it has no internal gain, the amount of charge released inside the silicon only depends on the average number of *e-h* pairs generated by a MIP inside the medium per unit length N_{e-h}, the distance travelled by a particle (i.e. the device thickness) d. This quantity can then be used to obtain the area of a signal seen by the oscilloscope by knowing the amplifier trans-impedance $Z_{amplifier}$, assuming the impedance of the oscilloscope and the amplifier match.

$$A_{1MIP} = eZ_{scope}N_{e-h}d, \tag{3.5}$$

being e the elementary charge, Exploiting this result it is possible to obtain a counterpart to the PiN signal area in terms of "number of MIPs", i.e. multiples of the area generated by one MIP. Hence,

$$\#MIPs = \frac{A_{meas}}{A_{1MIP}} \tag{3.6}$$

In Chapter 4, the number of MIPs delivered to the DUT reported is extracted with this method.

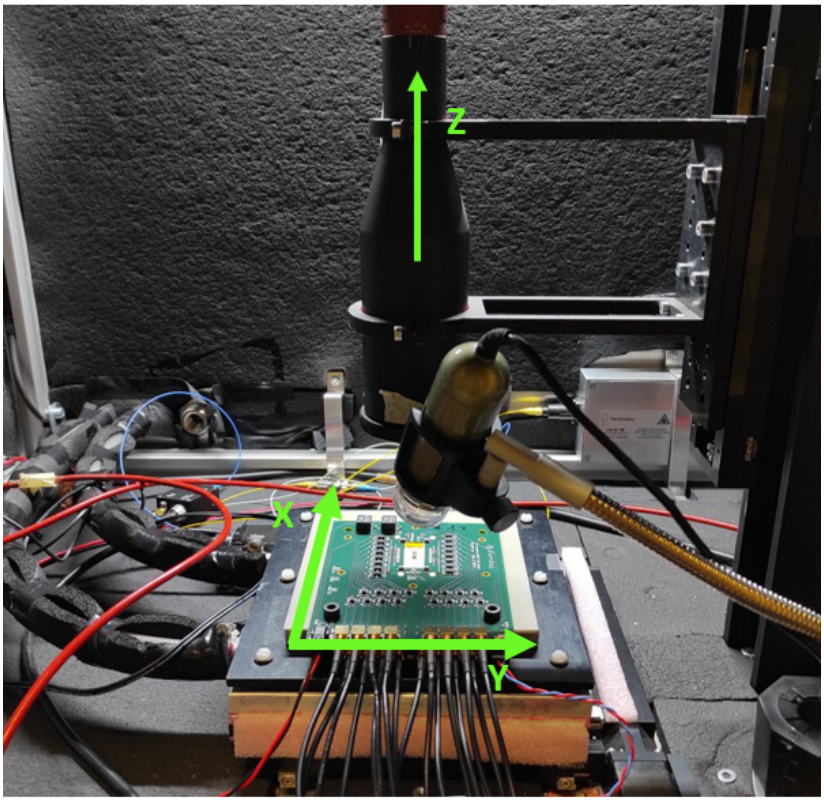

Figure 3.9: Photo of the Turin Laboratory TCT setup. In green is indicated the reference system whose coordinates are provided by the micrometric stages. It is visible the laser optics (vertical, under the z-axis), the infrared camera, and a DUT positioned on a FNAL board on its cooled basis.

Focus Optimization Procedure

The laser is connected using an optic fiber to an optical module, connected to the z-translator stage, composed of a Galilean beam expander, focusing lenses, and an iris which is exploited to correct the laser intensity. The optimization of the laser focus is essential to perform measurements with the TCT setup. A spot too wide could create inhomogeneities of the induced signal with respect to the position of shooting due to the presence of metalized sections or to charge screening effects [58]. Thus, the distance between the laser optics and the DUT is refined to achieve the narrowest possible laser spot at the surface of the DUT, as pictured in Figure 3.9. The Particulars setup is equipped with a $\sim$ 6 µm wide optic fiber and laser optics that allows reaching a minimum spot size of about 8 µm at the DUT level. To perform the focus finding procedure two regions are needed on the sensor: (i) one that would provide a signal compatible with zero even if hit by the laser, like areas with metalization or passive materials and (ii) a second region with close to no interference to the passage of the laser, normally called "optical window" for this reason. Then, a sweep is performed along a direction on the interface between these two regions (x) with 2-10 µm steps for different values of distances between optics and DUT (z) with larger steps, 10-50 µm. Such stages movement can be configured through a

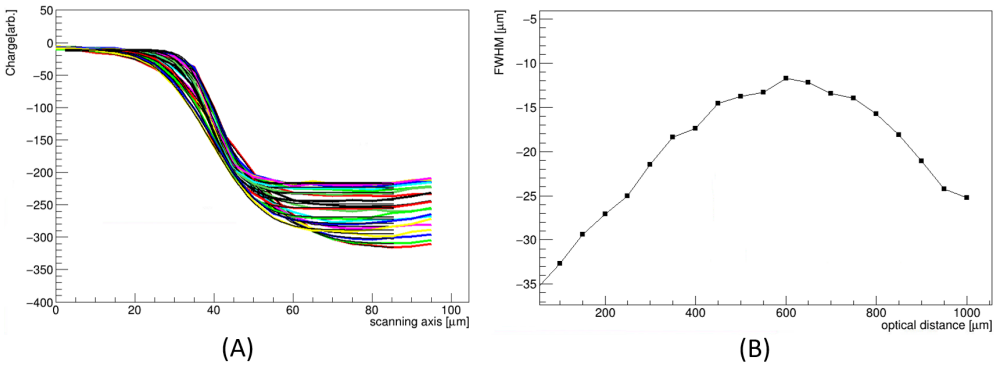

Figure 3.10: Collected charge as a function of the coordinate along the sensor surface (A). The transition between the metallic region and where the laser induces a signal in the device induces the characteristic "S" shape of the curve. In (B) are visible the values of FWHM extracted from the fit as a function of the distance between optics and DUT.

software suite, provided by Particulars, that allows recording a single waveform from 4 oscilloscope channels for each point of the scan. Such recorded waveform data can be then analysed offline through C++ based ROOT [59] macros which allow for the extraction of important parameters such as amplitude, area and risetime of the signal. To perform the focus optimisation, the amplitude and/or the charge are plotted with respect to the x-coordinate, obtaining a series of s-curves (see Figure 3.10, left) that are fitted employing a convolution of a step and a gaussian function, the error function. These functions represent, respectively, the passage from a region with no signal to a region where the signal can be induced in the sensor and the spatially extended structure of the beam spot. In fact, the optimal spot size is derived by minimizing the Full-Width-at-Half-Maximum (FWHM) of the gaussian function (Figure 3.10, right), which also the value reported in Chapter 4 when referring to the laser beam size.

The following sections are devoted to describing the methods used to investigate various characteristics of the DUT using this setup.

3.4.1 Gain Measurements

The gain G of a sensor was defined in chapter 1 and corresponds to the amount of charge collected by a UFSD Q_{UFSD} over the charge collected in a device with no gain (PiN) Q_{PiN}, i.e.

$$G = \frac{Q_{UFSD}}{Q_{PiN}}. \tag{3.7}$$

Recent studies [60] showed a gain suppression mechanism that does not scale linearly with respect to the laser intensity. For this reason, it is essential to perform the measurement of this parameter by tuning the laser intensity to a value such that it reproduces the MPV amount of charge of one MIP in order to reduce such an effect. It is nonetheless possible to account for

this screening mechanism and correct it after the measurements since it has proven to be very reproducible on multiple setups [58].

3.4.2 Time resolution - jitter

the jitter component of a UFSD time resolution is measurable through the analysis of the signal induced by the laser beam calibrated on one MIP-equivalent intensity. For this measurement in particular, it is important to generate the same amount of charge as a MIP since the time resolution depends on the signal amplitude. By computing the standard deviation σ_t of the difference in time between the DUT signal and the trigger pulse generated by the laser controller one can extract the jitter component $\sigma_{t,UFSD_jitter}$ of the UFSD DUT time resolution, since

$$\sigma_t^2 = \sigma_{t,UFSD_jitter}^2 + \sigma_{t,trigger}^2 \tag{3.8}$$

where $\sigma_{t,trigger}$ corresponds the uncertainty on the trigger measurement. Ideally $\sigma_{t,trigger} \ll \sigma_{t,UFSD_jitter}$, but it is possible to compensate by optically splitting the laser into two equal components and delaying one by a few ns. Both are then injected onto the DUT and the standard resolution of the difference between the two is then computed, without taking the laser trigger into consideration. It should be noted how this second method needs accurate tuning of both signals on a MIP-equivalent signal and could lead to greater systematic errors due to the slitting and delaying of the laser beam.

3.4.3 Large Area Scan

The precise characterization of large-area devices is one of the main advantages of the Particulars TCT setup. Among the various options, it is possible to record a single waveform of 4 channels at different (x,y) positions along the sensor surface. An offline analysis suite similar to the one employed for the focus optimisation (see Section 3.4 of this Chapter), allows to plot of different waveform features with respect to the laser position. With the advent of the first RSD batch (see Section 2.2), this data acquisition technique had proven to be restrictive. Due to the larger number of pads of the sensors from the RSD1 and RSD2 productions and the fact that a single waveform acquisition does not provide enough data to perform statistical analysis, the Turin TCT was upgraded both from a hardware and software point of view. Instead of the Teledyne LeCroy 4-channel oscilloscope, it was employed the CAEN 16+1-channel Digitizer DT5742 [61]. It features 16 analog input channels with 50 Ωinput impedance, one additional analog input channel dedicated to the trigger, 5 GS/s sampling rate, 12-bit resolution, 2x DRS4 digitizing chips and 500 MHz bandwidth. A specific python ROOT-based software package called UFSD_DigiDAQ was developed within the UFSD group to handle the digitizer, the HV supplier and the micrometric stages [62]. It wraps the CAEN proprietary WaveDump C++ [63] libraries into python, allowing to record multiple waveforms for each laser shooting position on the DUT and at a given value of bias voltage,

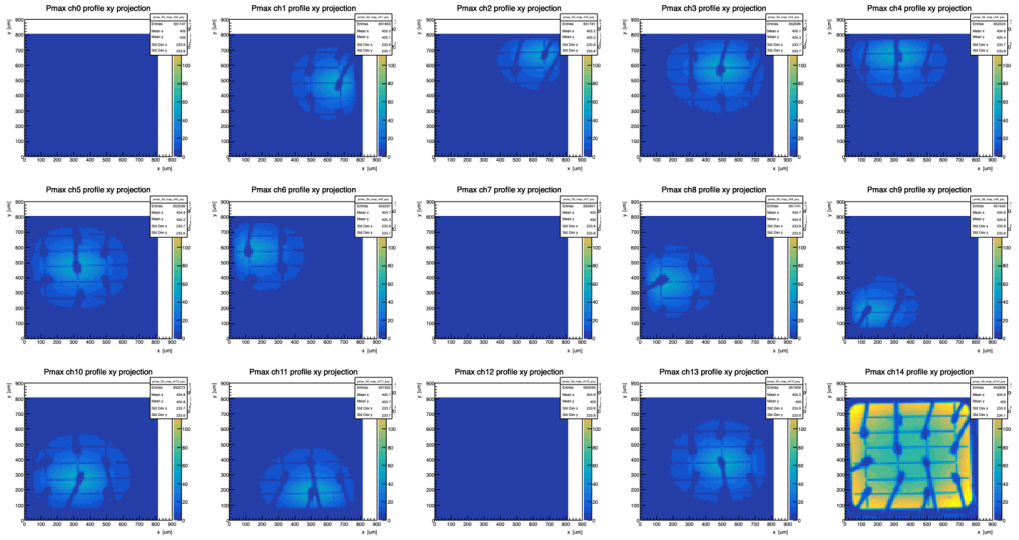

Figure 3.11: Different pads amplitudes with respect to the laser position. Channels 0,7,12 were disconnected during the data acquisition since the sensor at hand has 12 + 1 (DC ring, ch14) pads. The scan was performed with 10 µm steps in both directions.

which are saved in a .root file. With this addition, it is possible to shoot the laser at different positions on the sensor surface with very fine steps. In Fig. 3.11 is represented a result of a scan performed on an RSD2 detector with 12 AC-coupled pads and the DC contact acquired at the same time, with 100 waveforms recorded at each point in space. The collected data can then undergo different analyses, explained in detail in Chapter 4.

TCT setups are also ideal to measure the no-gain region of pixelated silicon detectors and the variation in charge collection efficiency of irradiated devices. Both methods are not described since they are not relevant to this work, an interested reader could find a detailed description of both in Chapter 4 of [39].

3.5 Read-out Boards

The measurements were carried out in the Turin Laboratory using three different read-out boards, all shown in Figure 3.12. All of them provide a larger gold-plated pad able to host the pad and smaller contacts, also gold-plated, on which the wire bonded to the sensor pad is bonded. A short description of their main characteristics follows:

- **Mignone (Torino) board**: it consists of a simple Printed Circuit Board that connects the bias voltage HV-BNC connector to the gold-plated central pad. Additionally, three lanes with no amplifiers are present, accessible through the SMU connectors visible in the figure. It is usually employed in combination with broadband 20 dB or 40 dB external amplifiers by Cividec for gain measurements. It was developed by INFN Torino.

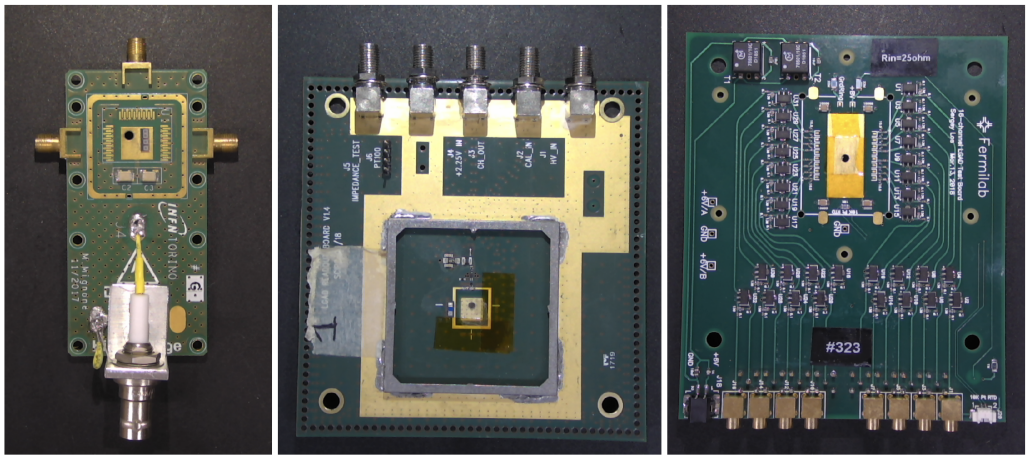

Figure 3.12: Pictures of the read-out boards employed in the Turin Laboratory. From left to right: Mignone, Santa Cruz (UCSC) and FNAL boards.

- **Santa Cruz board**: the Santa Cruz (SC) read-out board was developed by the University of California of Santa Cruz (UCSC). It is more articulated than the Mignone board since it provides: (i) a bias voltage connection to the gold-plated central pad, (ii) a single output channel with a fast inverting current amplifier with trans-impedance of about 470 Ω, that corresponds to an amplifier gain factor of about x10, (iii) an input low voltage connection to provide power to the amplifier (2.25 V), (iv) a calibration lane employed to inject charge for calibrating the amplifier performances, (v) and, finally, a Pt100 used to monitor the temperature close to the DUT. When combined with a 20 dB Cividec external amplifier and reading the output of a UFSD provides a noise RMS of about 3 mV.

- **FNAL board**: The rightmost picture in Fig. 3.12 depicts a 16 channels read-out board developed by the Fermi National Accelerator Laboratory (FNAL) electronics department. Each output lane is equipped with two amplificators based on the Mini-Circuit GALI-66+ integrated circuit, resulting in a total amplification factor of about x70. It has a bandwidth of ~ 1 GHz, and each amplifier uses a 25 Ωinput impedance and has a noise RMS of about 2 mV when coupled with a UFSD. It is of particular importance for this work, given the number of output channels it provides, and it is the board usually employed for large area scans explained in Section 3.4.3 on sensors from the RSD2 production (see Chapters 2,4).

3.6 DESY Test Beam Experimental Setup

A realistic application of the RSD2 devices was tested in various test beams performed at the DESY II Test Beam Facility in Hamburg A. This section describes the experimental setup deployed for this specific situation. More information on the facility can be found in Appendix A.

Due to the fact that multiple test beam sessions were performed, the

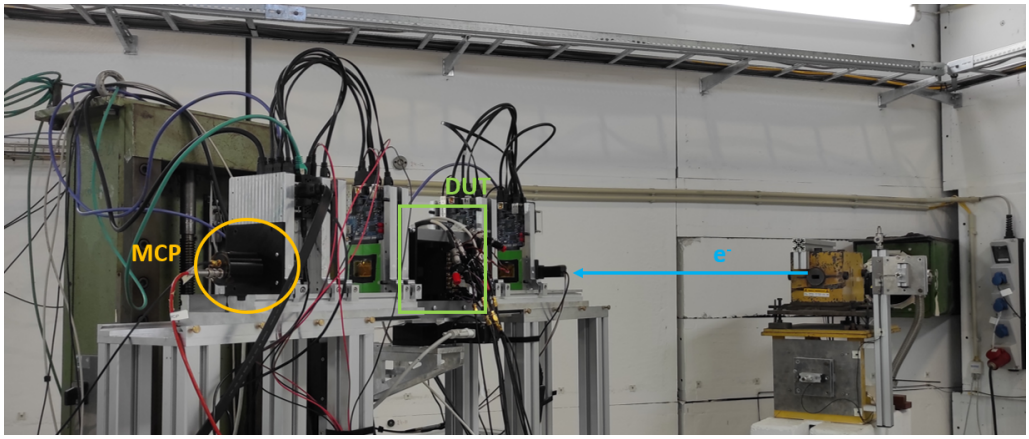

Figure 3.13: Photo taken during the test beam performed in the T24 area at the DESY II Test Beam Facility. The electron beam comes out from the secondary collimator and impinges on the first three planes of the ADENIUM telescope. The DUT is placed on a custom 3D printed frame placed on x-y-θ PI stage between the two telescope portions. Downstream from the DUT and after the remaining three telescope planes, it is placed the MCP timing reference mounted.

RSD2 sensors were tested in different test beam areas. For the purpose of this thesis, the experimental setup of the first test in T24 will be described, given that the disposition of the instrumentation was completely analogous.

The RSD2 devices aim at achieving top-of-the-line time and spatial resolution, and the proper instrumentation to assess their performances should be employed. The time reference of the setup is provided by an MCP produced by Photek [64] able to provide a time resolution of $\sim$ 15 ps to the system. The spatial resolution was estimated thanks to the ADENIUM telescope present in T24 that was arranged as visible in Figure 3.13. The DUT was mounted between the two sections of the ADENIUM telescope, composed of three planes each. To guarantee a correct interface with the moving PI stages provided at DESY, a custom 3D-printed frame was designed to host the DUT sensor. Similarly, another 3D printed frame was created to align the MCP with the particle beam and positioned downstream with respect to the DUT-telescope system (furthest left in the picture). It is worth noticing that the MCP signals are due to the Cerenkov light emitted by the scintillator coupled to it (see [64]). The positions of the telescope planes and the DUT along the beam direction are accurately measured with respect to the first plane since they are needed as input in the analysis.

The readout of the DUT signals was carried out employing the CAEN 16+1-channel Digitizer DT5742 [61] already utilized for the TCT measurements performed in the Turin Laboratory. It features 50 Ωinput impedance on all digitized channels, one additional analogue input channel dedicated to the trigger, 5 GS/s sampling rate, 12-bit resolution, 2x DRS4 digitizing chips and 500 MHz bandwidth. The data was then stored thanks to the UFSDPyDAQ software [62] on a root file. See Section 3.4.3 for further information on this instrument usage. A layout of the trigger logic can be found in Figure 3.14. The MCP signal is provided to the digitizer, which then generates a TTL busy signal. The logical signal is then forwarded to

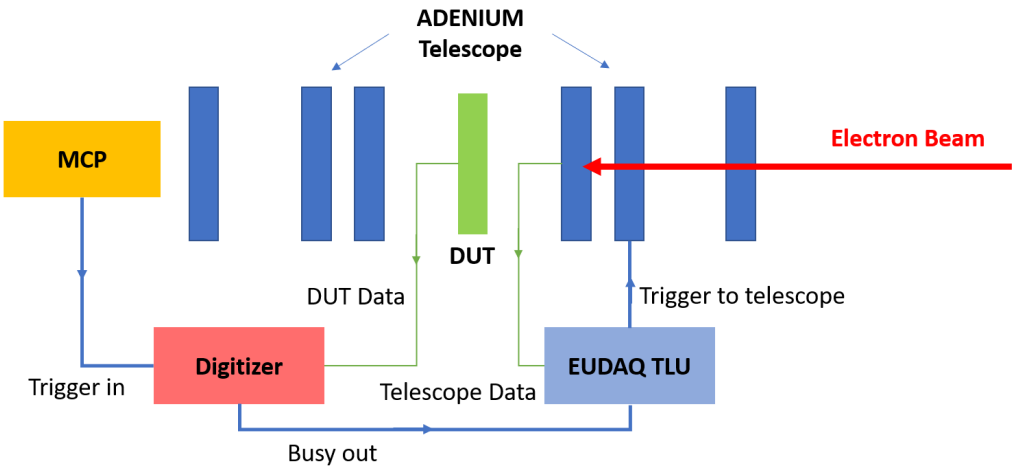

Figure 3.14: Trigger layout of the DESY test beam. The MCP provides a signal to the digitizer, which is employed to acquire the DUT data and generate a TTL signal (digitizer busy signal). Such logical output is forwarded to the EUDAQ TLU, which enables the data acquisition of the telescope. All trigger signals are depicted in blue, while data streams are in green.

the TLU, which triggers the telescope data acquisition. The data streams of the DUT and the telescope are saved separately, the first in a root file which stores the waveform samples of the signals for each event, while the second is a raw file based on the EUDAQ format.

The electron beam energy was kept in the range 3.6-6 GeV to guarantee a sufficiently high event rate combined with low multiple scattering.

During the data acquisition, it was noticed that the number of events recorded by the two systems, tracker telescope and digitizer, slightly differ above a certain number of triggers. After a detailed analysis, it was concluded that this issue is due to eventual generations of a rebound signal by the digitizer some microseconds after the falling edge of the busy signal. It was impossible to solve the problem from a hardware point of view, but a viable solution was found in the data analysis, which is reported in the 4.6 Section.

3.6.1 Telescope data extraction

The extraction of the tracks hit positions on the DUT is not natively possible in Corryvreckan at the time of writing. Therefore, the *4DTracking* method [65] was modified to generate an output containing the hit position at the DUT position when including this class in the Corryvreckan analysis. It should be noted that the ideal pipeline to merge the two different files into a single dataset would be to include the DUT waveform information into a EUDAQ format or to load the data inside the Corryvreckan environment. Nonetheless, the way in which the position is reconstructed (see Section 4.3) is not included in this suite, and the time resolution analysis typical of the standard tracking sensors is entirely new to this software package. Loading the DUT information inside Corryvreckan would mean

developing a brand new branch of this software and would require a serious effort, which is not the scope of this first analysis of the RSD2 devices. Therefore, we opted for a more straightforward approach: extracting the hit positions from Corryvreckan and conducting the final analysis outside its environment. To correctly fit the tracks, pre-alignment and alignment phases are needed. In these phases, the DUT is excluded from the analysis. Each plane is moved along the x-y coordinates, i.e. transversely with respect to the beam directions, and rotated in 3D to better fit the reconstructed tracks. In particular, the pre-alignment phase is conducted by enabling the *Correlations* and *Prealignment* methods, while the alignment is obtained by recursively running Corryvreckan with the addition of the methods *Tracking4D* and *AlignmentTrackChi2* until the planes of the telescope are moved by less than one micrometre in all directions. Once this series of actions is performed on the raw telescope file, an output file with all the hit positions at the DUT z-coordinate is generated and provided as input to the final data analysis reported in the next Section. It should be noted that events with multiple tracks are discarded. Given the relatively small dimensions of the trigger, the number of events in which the telescope reconstructs more than one track amounts to approximately 1 % of the total.

The methods and experimental setups described in this Chapter were employed to characterize the RSD2 production, whose results are reported in the next Chapter 4.

Chapter 4

Experimental Results

This chapter describes the experimental results obtained in the Turin Laboratory on the RSD2 detectors. For more details on the RSD2 production, see Section 2.3, while an exhaustive description of the experimental techniques exploited for data acquisition is given in Chapter 3.

Firstly, the results of some sample sensors static characterization are reported. Secondly, gain measurements made using the TCT configuration and with the DUTs bonded on two different read-out boards are shown. The final sections of this chapter are dedicated to the description of the large-area scans performed on the devices, along with the two analysis methods adopted to extrapolate the spatial and temporal resolutions.

The main objective of the inquiry presented in this chapter consists in evaluating the differences between the various geometries and layouts of the RSD2 production. The main DC-RSD future production (see Chapter 5) was tuned on the information gathered as a result of the RSD2 data analysis.

4.1 Static Characterization and Gain

Static characterization of the RSD2 devices was performed in the Turin Laboratory exploiting the setup described in Section 3.1. Current-Voltage, Capacitance-Frequency and Capacitance-Voltage characteristics were measured to assess the differences between sensors from the various wafers reported in Chapter 2.

4.1.1 Current-Voltage Characterization

On-wafer Current-Voltage characterization was performed on all devices and was carried out in FBK before the cutting procedure. In order to establish if the separation of the individual sensors had any impacts on their performances, *I(V)* curves were measured on a sample of sensors in the Turin Laboratory. The results were then compared with the ones obtained in the foundry. The sample consists in both PiN and LGAD devices from Block A with ∼800x800 µm^2 active area, called "device 08". *I(V)* curves were traced for at least one PiN and one LGAD from each of the 15 RSD2 wafers, finding great agreement with all FBK measurements. An example of

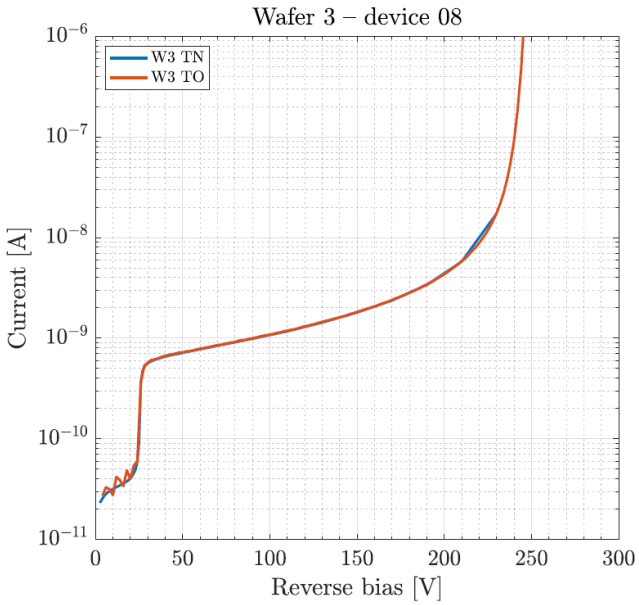

Figure 4.1: Comparison between the *I(V)* measured at FBK (blue) and in Turin Laboratory (red) on an 800x800 µm^2 active area detector.

these comparisons is visible in Figure 4.1. It is found that the 55 µm-thick wafers with gain layer doping equal to 0.96 (1, 2, 8, 9, 10, 11 and 12) all reach breakdown in the range 290-320 V, with no evident dependency on the *n+* doping. The same uniformity was noticed for the ones with a *p*-gain dose of 0.98 (3, 7, 13 and 14), with breakdown bias in the range of 230-270 V.

Finally, the only wafer with a lower gain layer dose (w15, *p*-gain = 0.94) goes into breakdown around 360-400 V. Moreover, from the analysis of this inspection, it was deduced that the FBK data was reliable and that all the different wafers behave as expected from their split table 2.2. From the *I(V)* curves measured by FBK, some maps of leakage current at a specific bias voltage as a function of the sensor position on the wafer can be drawn. Fig. 4.2 shows a map depicting this map for the same sensor tested in Turin in the whole wafer. Similar maps can be used to (i) determine the uniformity of the devices among the wafer, (ii) assess the differences in terms of gain and wafer type, and (iii) choose an ideal DUT. Analogous maps were produced for the larger devices from Block B and Block C, finding that wafers 3, 6, 7, 8 and 13 have good uniformity and yield, excluding those too close to the edges of the wafers in Blocks A and C.

Considering the results obtained, it was decided to restrict the additional static analysis to a sub-sample of wafers. Wafers 3, 7 and 13 were chosen because of their identical substrate, *p*-gain doping and thickness, leaving the only difference between each other the *n+* resistivity. The last one chosen consists of wafer 15, designated because identical to W13 except in its *p*-gain dose.

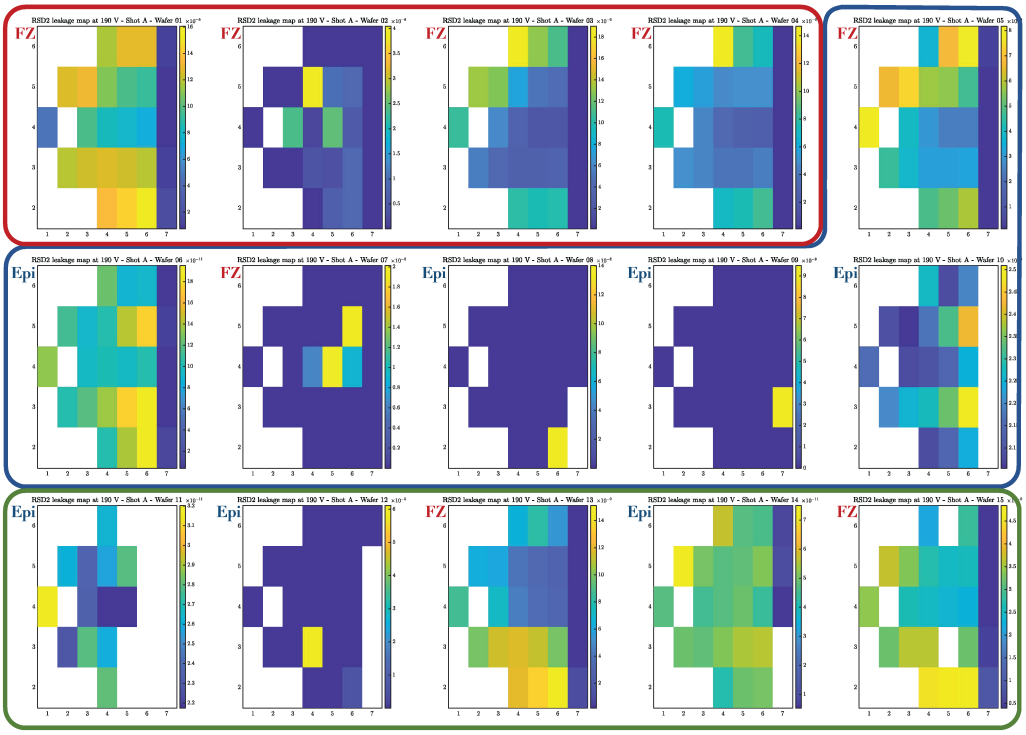

Figure 4.2: Maps of the leakage current @ 190 V on device 08 as a function of their position (row and column) on the wafer. All vertical scales are in A and are adjusted to better show the non-uniformities on the same wafer. The red, blue and green contours correspond to different $n+$ layer resistivity.

4.1.2 DUTs Full Static Characterization

A complete static characterization of the selected DUTs was performed in the Turin Laboratory. The tests involved sensors with smaller active areas from Block A and larger ones from Block B for each wafer. The small sensor is the structure numbered 15, also called "boxes", while the bigger one is the sensor 32 with a 2.6x2.6 mm^2 active area (see Section 2.3). They represent the smallest and biggest active area devices, respectively, that are employed in the characterization described in the next section 4.2.

Current-Voltage Characterization

Current-Voltage curves were traced to establish the correct functioning of all the devices, ensuring that the measurements matched the previous obtained. Figure 4.3 shows the plots of these characteristics. The differences in gain are evident, whereas wafers 3, 7 and 13 tend to reach breakdown in the same bias range, while wafer 15 has its increase in leakage current at a higher value of reverse voltage. It is noticeable the higher leakage current of the larger devices within the same wafer, as expected. Device 15 of Wafer 7 has a higher current and it is reported as an example of a functioning device with processing issues that brought a higher leakage current. This sensor corresponds to the one shown in Fig. 4.2 in the position row = 4, column = 6.

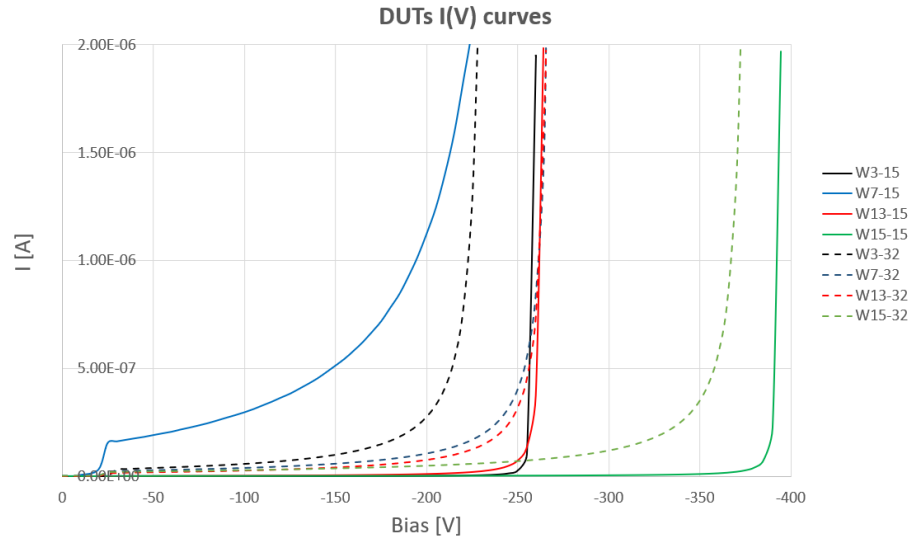

Figure 4.3: Current-Voltage characteristics of the DUTs. The number "15" refers to small structures (800x800 μm^2), while the number "32" corresponds to bigger structures (2.6x2.6 mm^2). On the y-axis, it is reported the DC pad current.

Capacitance Measurements

The following step involves Capacitance-Frequency and Capacitance-Voltage curves. They were measured employing the method described in Section 3.3 on all the DUTs already characterized by a *I(V)* standpoint. A sweep in frequency of the capacitance was performed to collect information about the ideal point for the *C(V)* measurement. All sensors had this ideal value in the range of 1-2 kHz, except for the Wafer 7 detectors. In the case of this wafer, abnormal behaviour was observed for several devices coming from different positions on the wafer. The trend observed in Fig. 4.4 shows a sudden early decrease in capacitance for increasing frequencies. Various amplitudes of the injected AC signal were tried, leading to the same outcome. This result can be due to a defective handle wafer or some errors made during the production procedure, resulting in weaker insulation between the guard ring and the pad. Such a hypothesis is also confirmed with the Capacitance-Voltage characteristics, where the capacitance does not show the typical trend proper of LGADs, and by the higher current drawn by the guard rings observed on most of the devices. Nonetheless, some devices from this wafer are still functional and were employed in the next steps of this work.

C(V) measurements were carried out on all sensors to establish the bias voltage needed to deplete the gain layer and to extrapolate its dose profile. The inspected depth was computed having as $d = \frac{\epsilon_{Si} A}{C}$, being A the area covered by the gain layer, ϵ_{Si} the silicon permittivity and C the measured capacitance. Having obtained d, with Eq. 3.4 it is possible to determine the doping density, employing the numerical derivative of $1/C^2$. The doping densities as a function of the depth inside the sensor are shown in Fig. 4.5 for all the DUTs except the W7 devices. As visible in Figure 4.5, the dose profiles of wafers 13 and 15 overlap and peak at the same depth value in

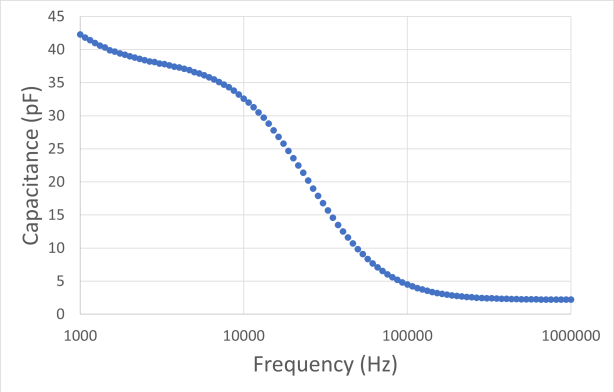

Figure 4.4: *C(f)* characteristics (*left*) curve of a device from wafer 7. It can be noticed the sudden decrease in capacitance at low-frequency values and the absence of a plateau in that region.

both geometries. On the other hand, W3 has a different peak position due to its difference in resistivity and RC coupling constant, proven by the significant shift in depth between the two structures geometries. Uniformity among different big and small structures from the same wafer was also tested, finding excellent agreement between the same different structures with a peak position within the error due to the gain layer area estimation. Finally, the ratio $ratio_{th}$ between the total dose of the W15 and the one of the W13 can be computed from the production split table by employing the gain layer doses. One can perform a comparison with the total dose extrapolated with these measurements, obtaining

$$\begin{aligned} ratio_{th} &= \frac{N^{th}_{A,W13}}{N^{th}_{A,W15}} \simeq 1.04 \\ ratio_{exp} &= \frac{N^{exp}_{A,W13}}{N^{exp}_{A,W15}} \simeq 1.08 \pm 0.04 \end{aligned} \tag{4.1}$$

where the error on the experimental ratio $ratio_{exp}$ should be considered a lower limit since it has been calculated considering no inaccuracy on the capacitance and an error on the area A of 1% in the small devices.

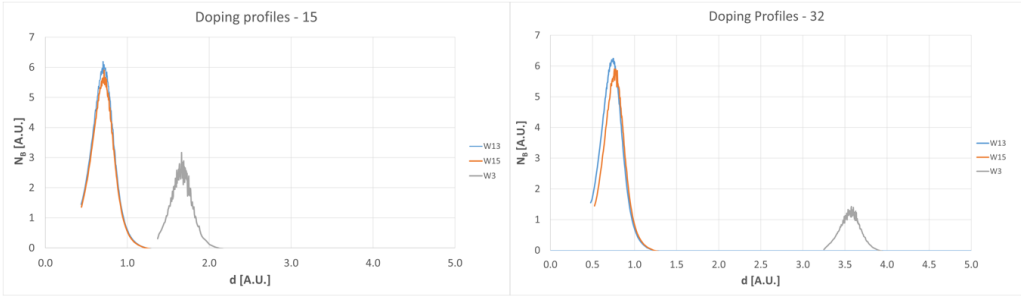

Figure 4.5: Doping densities as a function of the depth of the devices tested for the small structures 15 (*left)* and large structures 32 *right*.

4.1.3 Gain Measurement

The sensor gain is essential to the RSD sensors since their performances greatly depend on the amplitude of the recorded signals and on the electronic noise, as discussed in the next sections. In order to have a deeper understanding of the RSD2 performances, the characterisation of this parameter is fundamental to understand the mechanism at play. The DUTs gain was measured employing the method discussed in Section 3.4.1 at the TCT in the Turin Laboratory. The laser calibration was executed with an RSD2 PiN small structure (structure 15) from wafer 3. Multiple measurements have been taken exploiting the Mignone and FNAL readout boards 3.5 and the signals recorded to draw the gain curves. The gain measurements obtained with the FNAL readout board are of particular importance since it is the board of choice in the large area measurements. The results of this inquiry are reported in Figure 4.6. It can be noticed that the reverse bias voltage spans over a wider range than one of the *I(V)* curves due to a quenching resistor placed on the bias line of the FNAL board. The shift in bias is not of particular relevance since the DUTs are placed inside a dark enclosure and the leakage current is kept as low as possible. From these results, it is possible to convey that all devices reach a gain value of about 20 in a bias region where no discharges occur due to the proximity to the breakdown voltage. It is also evident the trend that was already visible in the Current-Voltage characteristics, where wafers with lower gain (wafer 15, for example) reach a higher gain value with higher bias. Moreover, the resistivity does not seem to affect the gain value, but it does alter the signal shape, with higher resistivity DUTs having a longer signal falling edge.

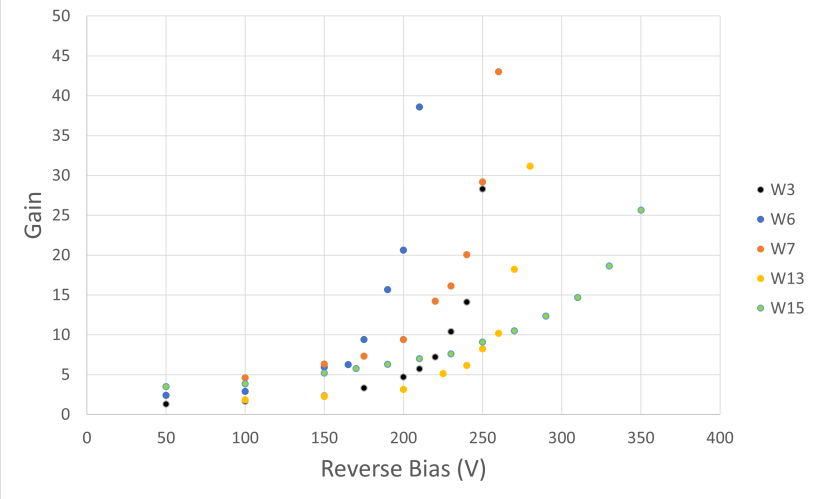

Figure 4.6: Gain as a function of reverse bias for the DUT of the RSD2 production.

4.2 Large Area Scans and Analysis

Central to this work is analysing the RSD2 DUTs performance assessments over their entire active area employing the Turin TCT setup. Various

geometries have been tested and analysed with analytical and Machine-Learning (ML) methods, depending on the suitability of the AC-pads disposition. In the first part, a general description of the dependencies of the time and space resolutions is given on which the analysis and future optimisations of RSD depend. The data acquisition has been performed following the procedure described in Section 3.4.3 with the laser intensity set to produce a signal equivalent to the one produced by 1-3 MIPs. In these scans, the shape of the laser spot on the DUT is of fundamental importance, so the spot FWHM has been kept within the minimum allowed by the setup at disposal, hence $10 \pm 1\mu m$. Each acquisition consists of a scan over the sensor surface, covering an area larger than the one of the pixel. The laser moves by 10-20 µm steps depending on the area to be covered, and 50-100 shots are recorded for each position. The waveforms are then processed to extract the features of interest by a C++ ROOT-based application which are fed to the ML or analytical method for the position reconstruction.

Spatial Resolution

The space resolution reconstruction σ_{pos} has four distinct contributions:

$$\sigma^2_{pos} = \sigma^2_{jitter} + \sigma^2_{rec} + \sigma^2_{setup} + \sigma^2_{sensor}. \tag{4.2}$$

The first contribution σ_{jitter} degrades the precision of the measurement, while the other terms degrade the accuracy of the position reconstruction.

- σ_{jitter}: The jitter term is due to the amplitude variation caused by the electronic noise. It increases with larger electronics noise $\sigma_{el.noise}$, while it becomes less noticeable for high amplitude A values, hence

$$\sigma_{jitter} \sim \frac{\sigma_{el.noise}}{A}. \tag{4.3}$$

  The role of readout electronics in the RSD performances is fundamental: since the jitter is the predominant contributor to the total spatial resolution, very low noise electronics should be employed. Traditionally, one option consists of adopting current integrating amplifiers, which are unsuitable for AC-RSDs given their bipolar signals. This is one of the motivations behind the development of DC-coupled RSD (DC-RSD) described in Chapter 5. In RSDs, the signal is split among n AC-pads, so the amplitude of the signal collected by each one is proportional to $1/n$. Since the electronics noise variance is also directly dependent on n

$$\sigma_{jitter} \sim \frac{\frac{\sigma_{el.noise}}{\sqrt{n}}}{\frac{dV/dx}{n}} = \frac{\sigma_{el.noise}}{dV/dx}\sqrt{n} \tag{4.4}$$

  Therefore, the number of pads sets a limit on spatial precision. The jitter can be mitigated by employing low-noise electronics, biasing the sensor so that high gain values are reached, and reducing the number of readout pads absorbing the produced signal to a reasonable amount.

- σ_{rec}: the position is inferred through algorithms that might generate a systematic offset depending on the hit position. One example consists of the distortion due to the charge imbalance method reported in equation 4.6, which, depending on the detector type and its attributes, might induce a more significant discrepancy between the hit position and the reconstructed coordinate in a specific region of the active area. This is a known phenomenon and has been studied in resistive gas detectors [66].

- σ_{setup}: It is related to the experimental setup. Small variations in the beam intensity, the laser focus or eventual differences in the gain of the amplificators could lead to less accurate position reconstruction.

- σ_{sensor}: Also the sensor imperfections contribute to the total resolution. For example, a non-uniform $n+$ resistive layer would cause the signal to spread unevenly, causing differences in reconstruction among the sensor surface.

Temporal Resolution

The temporal resolution of an RSD device has the same contributions as that of a traditional UFSD, whose parametrization terms and their contributions are discussed in [67]. Since the signal is shared, the signal travels a certain distance before reaching the read-out pad, and the delay between the hit time and arrival time to the metalization introduces uncertainty.

$$\sigma^2_{time} = \sigma^2_{jitter} + \sigma^2_{Landau} + \sigma^2_{delay} \tag{4.5}$$

- σ_{jitter}: similarly to the spatial reconstruction, it is due to the electronics, $\sigma_{jitter} = \sigma_{el.noise}/(dV/dt)$. As for the spatial resolution, the jitter increases if the signal is shared among n readout pads as $\sigma_{jitter} \sim \sqrt{n}$, see Equation 4.4.

- σ_{Landau}: due to non-uniform ionization, it accounts for 30 ps in 50 µm thick sensors.

- σ_{delay}: depends on the hit position reconstruction and the precision of the delay measurement.

The prevailing term in RSD depends on the situation: depending on the signal amplitude, the jitter or the Landau noise is dominant, respectively, for small and large signals. Degradation of the computed time does not depend on the pixel size if the $n+$ resistivity is tuned on its dimensions and the delay is well-measured. It does not worsen for spatial resolutions with uncertainty under 30-40 µm.

4.3 Reconstruction Methods

Two different approaches have been carried out to reconstruct the hit position from features of the signals collected on the AC-pads: one is based

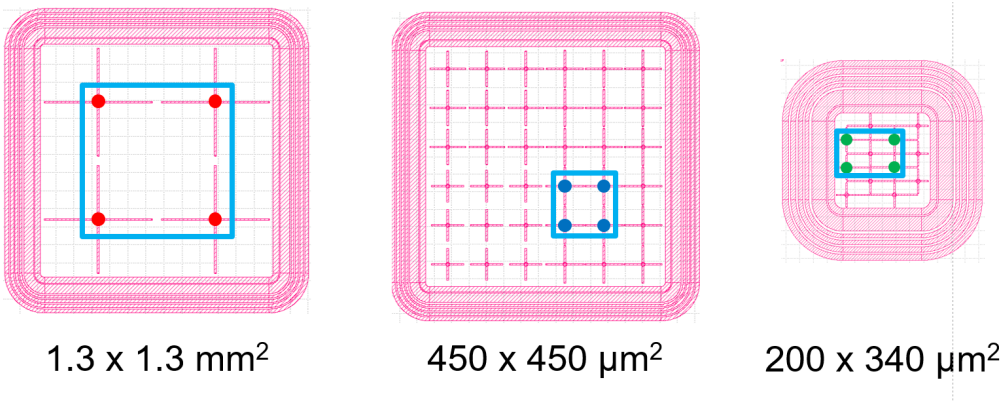

Figure 4.7: Geometrical layouts of the DUTs employed with the analytical method. The area considered is highlighted in blue, while the dots represent the pads contacted and connected to the read-out electronics. At the bottom are indicated the dimensions of the area of inspection.

on an analytical approach mixed with the use of a look-up table, while the second benefits from ML techniques.

4.4 Analytical Method

This approach is based on an implementation of an analytical law to the data which describes the evolution of the signal or its features over the detector resistive layer. Only devices with squared or square-like pixels have been considered for this analysis. In Figure 4.7 are reported the layouts of the three different sensors taken into consideration. They have different pitches, spanning from 200x300 µm^2, with the same active area of the device 15 previously mentioned, through 450x450 µm^2, up to 1.3x1.3 mm^2. The wafers evaluated are the ones described in Section 4.1, with the exception of wafer 13 since its resistivity is equal to the one of w15 and it has the same gain doping as the remaining wafers. Geometrically, all devices are characterized by 20 µm-thick crosses, with length and distances in between them that depend on the pitch. The device with the larger pitch has a inter-crosses D distance of 100 µm (see Section 2.3), while both the 450x450 µm^2 and the 200x300 µm^2 sensors have $D = 10$ µm,

Since in RSDs the relative distances between the read-out electrodes and the impact point determines how the signal is shared among them, it is possible to infer the hit position by exploiting features of the collected waveforms. Depending on the pad layout, the position can be identified with an analytical model only or a new approach is needed. The first is valid for point-like read-out electrodes proper of the RSD1 production, while RSD2 devices have extended metalization, which renders the analytical approach unsuitable for modelling the signal propagation on the resistive layer. In the second scenario, a reconstruction algorithm may be found, and its biases can then be corrected using the experimental data. The first part of this work was published in [68], which reports the results obtained on the DUTs from wafer 15.

4.4.1 Hit Position Reconstruction

Two different reconstruction algorithms were considered for the RSD2 devices analysis: (i) the Signal-Weighted Position (SWP) and (ii) the Discretized Position Circuit (DPC) [69]. From recent studies on the RSD2 sensors [68], it has become evident that the most suited is the DPC, in which the position is reconstructed using the signal amplitude or charge imbalance between the pads on the two sides (top-bottom for the y-coordinate and right-left for the x-coordinate). The positions are reconstructed as in Equation 4.6.

$$\begin{aligned} x_{rec,i} &= x_{centre} + k_x \frac{pitch}{2} \frac{A_3 + A_4 - (A_1 + A_2)}{\sum_{j=0}^{4} A_j} \\ y_{rec,i} &= y_{centre} + k_y \frac{pitch}{2} \frac{A_1 + A_3 - (A_2 + A_4)}{\sum_{j=0}^{4} A_j}, \end{aligned} \tag{4.6}$$

being $(x_{rec,i}, y_{rec,i})$ the reconstructed coordinates of the i-th hit on the sensor, (x_{centre}, y_{centre}) the position of the pixel centre, and A_j can be either the amplitude or the charge collected on the j-h pad. As previously mentioned, the RSD2 signals are bipolar, making correctly integrating their positive portion difficult. Moreover, the amplitude of the signal decreases with the propagation on the resistive layer while the area remains constant. For these reasons, the amplitudes were chosen and used for the rest of this work, having also considered the signal-to-noise ratio of the electronics employed. k_x and k_x are measured experimentally and are obtained through

$$\begin{aligned} k_x &= \frac{1}{\frac{A_3+A_4-(A_1+A_2)}{\sum_{j=0}^{4} A_j}\Big|_{x=x_{tr}}} \\ k_y &= \frac{1}{\frac{A_1+A_3-(A_2+A_4)}{\sum_{j=0}^{4} A_j}\Big|_{y=y_{tr}}}, \end{aligned} \tag{4.7}$$

where (x_{tr}, y_{tr}) are the coordinates of the top right pad. These parameters scale the reconstruction position in the event that, for hit positions close to one electrode, the signal collected from the electrode on the other side might not go to zero, limiting erroneous position reconstruction. Their importance is greater for pixels with small pitches and if the resistivity of the resistive sheet is low. In contrast, for large pixels from wafers with low resistivity, it is usually equal to 1. To avoid nonphysical results due to the presence of the electrodes metallization combined with the spatial extension of the beam spot, it has been defined a minimum distance from the metal of 20 µm for the 200x300 µm^2 and 450x450 µm^2 layouts, and of 30 µm for the 1300x1300 µm^2. Below this value, the waveforms are discarded and not taken into consideration. This limit defines the fiducial area over which the analysis is performed.

4.4.2 Look-up Table

Figure 4.8 (B) shows an example of reconstruction in a 450x450 µm^2 pixel obtained with the DPC method. As visible from 4.8 (C), the points are non-

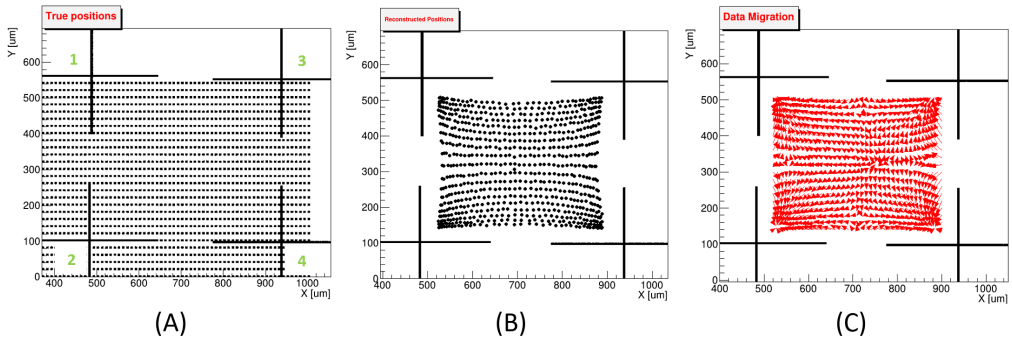

Figure 4.8: Example of a position reconstruction obtained on a 450x450 µm^2 pixel from wafer 7. (A) shows all the laser positions in on the device, (B) depicts the positions reconstructed inside the fiducial area and (C) the migration of the reconstructed points with respect to the true ones.

negligibly shifted from the original point due to the reconstruction method, even if fairly accurate thanks to the cross-shaped metal electrodes. Clusters of points tend to develop close to the read-out pads, generating large migrations. Nonetheless, it is possible to correct this shift between the reconstructed position $(x_{rec,i}, y_{rec,i})$ and the true hit coordinates (x_{true}, y_{true}) by performing a so-called "training" data acquisition in which the systematic difference between the two is evaluated and recorded in a look-up table. When a second data acquisition takes place, the measured coordinate $(x, y)_{meas})$ is compared to the proximity of recorded coordinates $(x, y)_{meas.training}$ (within a circle of r_{cor}) and shifted towards the true ones $(x, y)_{truetraining}$. Hence

$$\begin{aligned} x_{rec} &= x_{meas} + \Delta x \\ y_{rec} &= y_{meas} + \Delta y \end{aligned} \tag{4.8}$$

Where the shifts Δx and Δy result from the equation

$$\begin{aligned} \Delta x &= \frac{\sum_i^N w_i (x^i_{meas.training} - x^i_{truetraining})^2}{\sum_i^N w_i} \\ \Delta y &= \frac{\sum_i^N w_i (y^i_{meas.training} - y^i_{truetraining})^2}{\sum_i^N w_i} \\ w_i &= [(x^i_{meas} - x^i_{meas.training})^2 + (y^i_{meas} - y^i_{meas.training})^2]^{-2}. \end{aligned} \tag{4.9}$$

The radius r_{cor} value is tuned on the pixel dimension and the laser step to ensure that some training coordinates are included, and not too large to avoid points with different migration characteristics. Its value did not substantially impact the correction and was set to 30 µm for the subsequent studies. After this procedure, the terms σ_{setup} and σ_{sensor} become negligible, as demonstrated in [68]. The "training" data corresponds to a dataset taken in the best possible scenario, meaning that a well-known environment is needed and the highest signal-to-noise ratio of that particular sensor. Therefore the correction matrix was created with measurements in the TCT setup previously mentioned with the sensor at its maximum

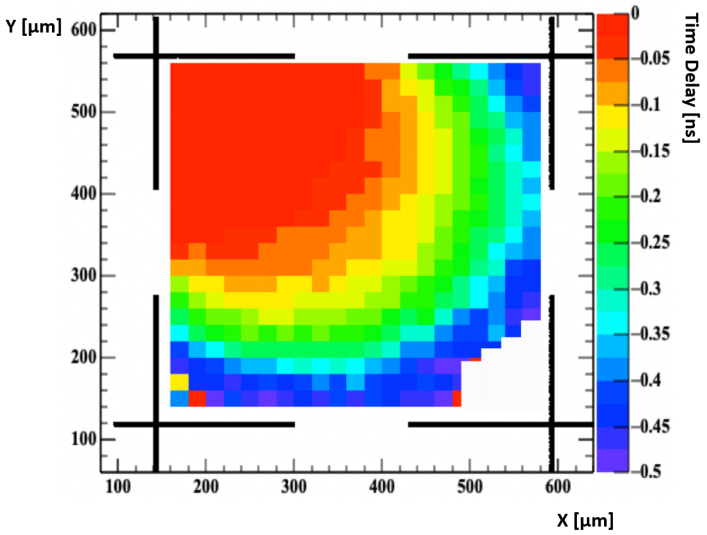

Figure 4.9: Signal delay with respect to the top-left read-out pad the 450x450 µm^2 geometrical layout from wafer 15. Image is taken from [68].

viable gain. Applying the same look-up table to devices with different characteristics could result in an ambiguous position reconstruction since the deformation of the reconstructed position pattern depends on the signal generation, its propagation among the resistive surface and how it is collected by the various electrodes. Therefore, this procedure was performed by applying the correction matrix to the sensors of the same wafer.

4.4.3 Hit Time Reconstruction

When measuring the time coordinate with RSDs, it should be kept in mind that the signal travelling towards the i-th electrode has a certain delay t^i_{delay} due to the propagation on the resistive layer between the hit position and the electrode itself. Similarly to other time tagging detectors, the hardware introduces another delay $t^i_{hardware}$ due to cable lengths and read-out boards. Therefore, the reconstructed hit time t^i_{rec} can be expressed as

$$t^i_{rec} = t^i_{meas} + t^i_{delay} + t^i_{hardware} \tag{4.10}$$

being t^i_{meas} the measured time of the signal collected by the i-th electrode.

Figure 4.9 shows the delay measured for the 450x450 µm^2 structure from wafer 15. Such a histogram can give information about the t_{deleay} parameter, which depends on the layout of the electrodes, the capacitive coupling with the n$^+$ layer and its resistivity. The hardware delay term is estimated through these maps by choosing a delimited area close to the read-out pad, i.e. the pixel corners, where the influence of the propagation is negligible, in the order of 20x20 µm^2. The measured time for a given position t_{rec} can be calculated by considering the charge-sharing nature of RSDs. Its value is found by minimising the following Equation 4.11

$$\chi^2 = \frac{\sum_i^4 (t_{rec} - t^i_{rec})^2}{\sum_i^4 \sigma_i^2} = \frac{\sum_i^4 (t_{rec} - t^i_{rec})^2}{\sum_i^4 \frac{\sigma_{el.noise}}{dV_i/dt}} \tag{4.11}$$

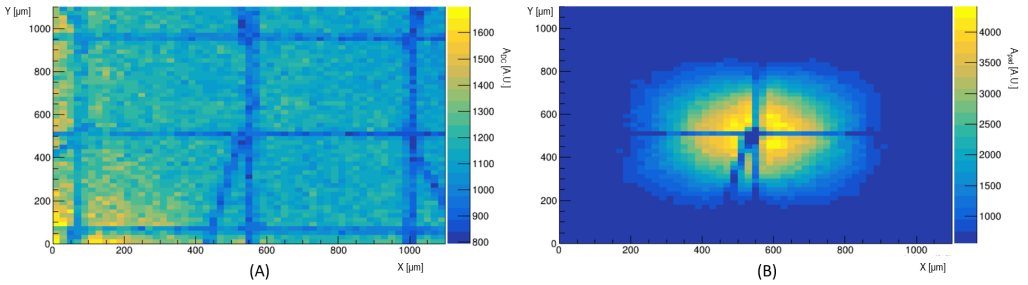

Figure 4.10: Maps of the DC electrode (A) amplitude and one of the AC-pads (B) recorded in each position on the sensor. The DUT corresponds to a W3 450x450 µm^2.

being σ_i the uncertainty on the reconstructed time of the i-th pad t^i_{rec}. Since the jitter term is the only one that improves with adding multiple pad readings, it has been used in the χ^2 expression. Approximating its value with $\sigma_i \sim \frac{\sigma_{el.noise}}{A_i/t_{rise}}$, where A_i is the signal amplitude and t_{rise} its risetime, one obtains

$$\begin{aligned} t_{rec} &= \frac{\sum_i^4 A_i^2 t^i_{rec}}{\sum_i^4 A_i^2} \\ \sigma_{trec} &= \frac{t_{rise}\sigma_{el.noise}}{\sqrt{\sum_i^4 A_i^2}}. \end{aligned} \tag{4.12}$$

Assuming an equal split among the n electrodes, the error becomes $\sigma_{trec} = \frac{t_{rise}\sigma_{el.noise}}{A}\sqrt{n}$, proving that the time resolution worsens with the increase in pad number as $\sqrt{n}$ just as the spatial resolution.

Alignment and Reference System

Aligning the sensor is made possible by exploiting its metal pads which reflect the laser. Each electrode coordinates in the laser reference system is found by looking for the signal amplitude minimum of the specific pad. This information is then fed to the algorithm that computes the pixel centre and shifts the reconstruction reference system accordingly through Equation 4.6. Figure 4.10 shows a map of the amplitudes recorded on the DC electrode (A) and one AC-pad (B) of a wafer device 3 with 450x450 µm^2 pixels. The metallic electrode positions are clearly visible as regions with lower amplitude, and even greater precision can be found by utilising the AC-pads maps (*right*). Occasionally a DUT could be glued with a slight rotation with respect to the board and, therefore, to the laser reference system. To account for this variation, a rotation of the laser coordinates with respect to the reconstruction reference system was performed when necessary. Its impact on the final reconstruction is low, even for the larger structures, since the rotation angle does not exceed 3°.

4.4.4 Space Resolution Results

This section reports the various DUTs space resolutions as a function of the gain. The variation of gain is achieved by changing the bias voltage of the

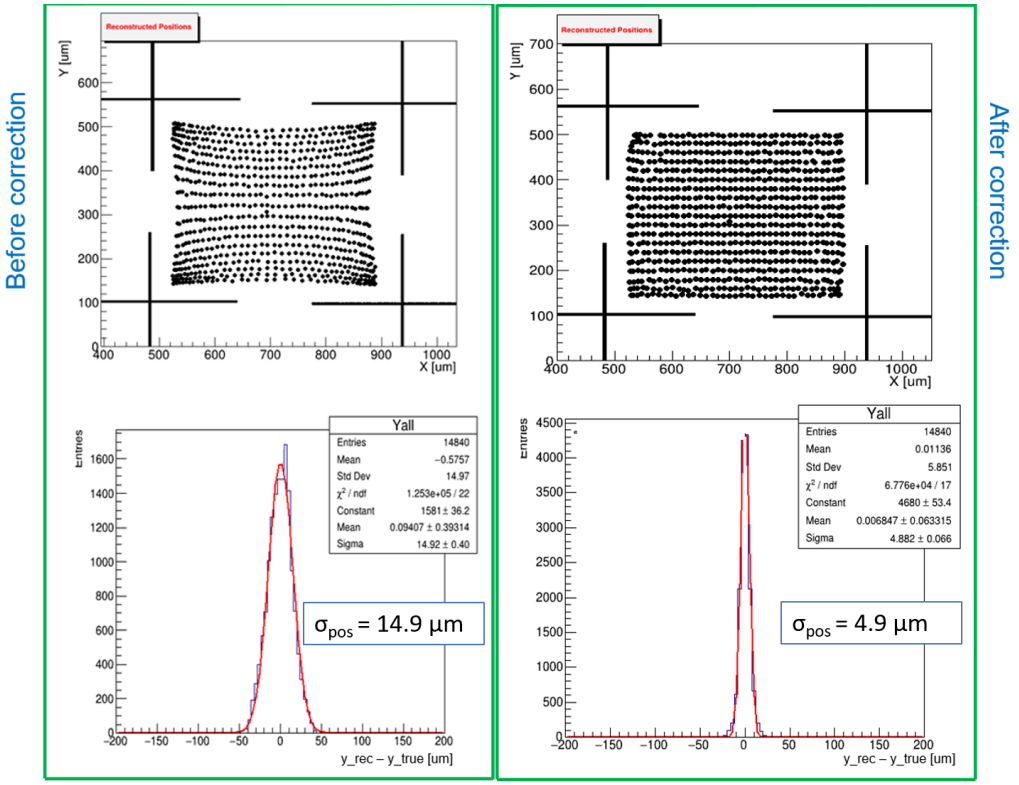

Figure 4.11: Position resolution before (*left*) and after (*right*) correction on a 450x450 µm^2 device from wafer 3 at its maximum gain point.

DUTs and the intensity of the laser. The procedure followed for each sensor consists in:

1. scanning the sensor surface shooting the laser with 10 µm step for the 200x340 µm^2 and the 450x450 µm^2 devices, while 20 µm steps have been chosen for the 1300x1300 µm^2 layout.

2. The signal is collected in each point 50-100 times and its amplitude is used to reconstruct the position with Equation 4.6. This second step produces the results displayed in Figure 4.11 (left), with an already promising position resolution result $\sigma_{pos} = 14.9\mu m$ obtained by performing a gaussian fit on the distribution of the difference between the reconstructed positions and the true ones. Non-gaussian tails are visible in the graph due to the clustering discussed in Section 4.4.2.

3. The correction procedure is applied to the data acquired, as explained in Section4.4.2, having employed the highest gain dataset for each sensor to perform the training and generate the look-up table. As a result, the position resolution is greatly improved, as visible in Figure 4.11 (*right*): the non-gaussian tails are almost eliminated and the value of the spatial reconstruction refines to the value of $\sigma_{pos} = 4.9\mu m$, with a 3x improvement factor.

Since signals produced by sensors with higher resistivity have longer RC constant, their DC signal is more extended in time, and the estimation of the

total area of the signal is problematic due to low deviation from the baseline. Therefore, it has been chosen to report the spatial resolution results as a function of the AC-signals amplitude sum instead. Previous experience [68] and lab measurement assessed that with the sensor operating at gain 30 and the laser intensity set to 1 MIP, the amplitude sum ranges in the 55-60 mV interval. The value of the amplitude sum is found through a gaussian fit over the area inspected.

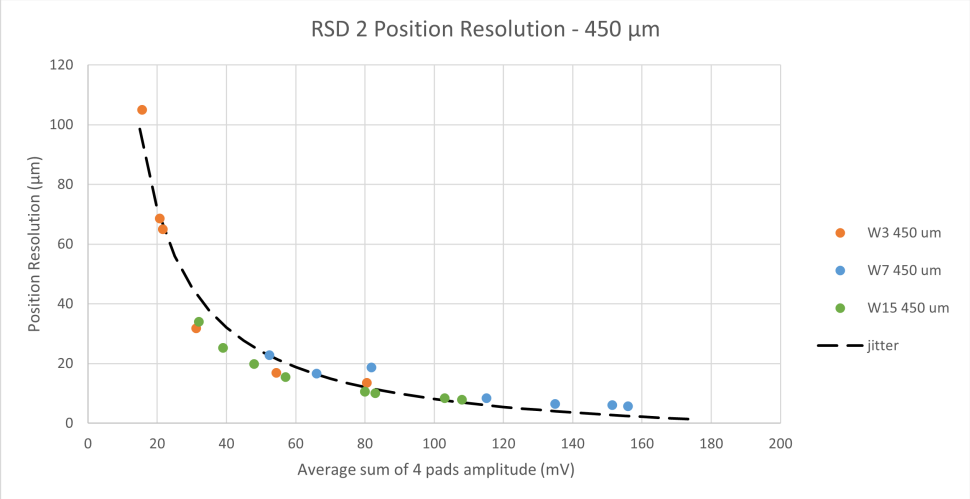

Figure 4.12: Position resolution of the 450x450 µm^2 devices from RSD2 obtained with the analytical method. Each color corresponds to a different device, different points of the same color correspond to data acquisitions taken at different bias points.

This study aims to understand the interplay between resistive layer doping and pixel dimensions. In Figure 4.12 are reported the results obtained with 450x450 µm^2 for all the wafers tested as a function of the AC-amplitude sum. Despite the differences in terms of $n+$ resistivity between wafers, the resolution values are all overlapping and agree with the jitter trend $\sim 1/A$ which is dominant even at high gain. A spatial resolution at amplitude = 60 mV (gain = 30) is equal to 18 µm, about 4 % of the pitch.

A dependence on the resistivity is seen in the case of the smallest device, the 200x340 µm^2 layout. Thanks to its rectangular geometry and the DPC method, it has been possible to separate the reconstruction on the two coordinates, conducting a reconstruction over the side 200 µm long and a separate one over the 340 µm side. It is noticeable how the resolution is better on a more resistive surface if the distances at play are smaller. In fact, the shortest side of the wafer 3 sensor reaches $\sigma_{pos} = 7.7\mu m$ at 55 mV in amplitude, again about 4 % of the pitch, whereas wafer 15 resolutions are double for high values of gain. Both sensors follow a jitter-like curve (see Figure 4.13) which dominates their performances as expected. Finally, the 1300x1300 µm^2 output proves this trend, with the less $n+$-resistive wafer 15 that performs better over longer pitches than wafer 3. Figure 4.14

To summarize these ideas and confront the results obtained on the different wafers, it was drawn the projection of all the resolutions at 55 mV in Figure 4.15. The linear fits slope suggests that the way the resolution scales

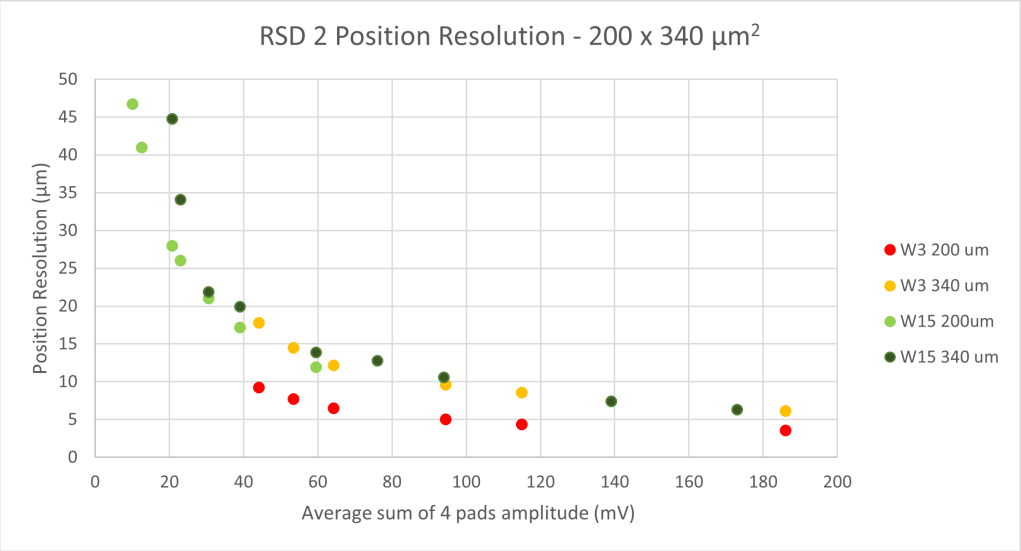

Figure 4.13: Position resolution of the 200x340 µm^2 layout achieved with the analytical method.

with the pixel dimensions depends on the resistivity, aiding in the choice of the correct one for a desired pixel size. From the results obtained, for small pitches ($\leq$ 200 µm) one should use higher sheet resistivities, while for larger pitches ($\sim$ 1 mm) lower resistivities are preferable. Finally, it should be noted that better results are expected by exploiting point-like particles and a precise tracking system instead of a laser with a spot size of $\sim$ 10 µm.

All devices reach resolutions at equivalent gain = 20 below what is reachable with traditional silicon pixels $\sigma_{trad} = \frac{pitch}{\sqrt{12}}$. It would equal to $\sim$ 375 µm, 130 µm, 98 µm and 58 µm, for 1300 µm, 450 µm, 300 µm and 200 µm pitches, respectively. Thanks to these results, the devices from RSD2 have proven to be a very convincing candidate for space reconstruction in future experiments.

4.4.5 Time Resolution

The TCT set-up was utilized in this study to measure the time difference ($t_{trig} - t_{rec}$) between trigger time and reconstructed event time of the points of the laser scan over the fiducial area. The nature of the measurement does not allow to take into account the Landau term of the time resolution, as already discussed in 3.4 which accounts for 30 ps in a 50 µm thick RSD sensor and was measured in [53]. t_{rec} is reconstructed with the methods described in Section 4.4.3 and its difference with t_{trig} is reported in Figure 4.16. Although very precise, the TCT trigger has its own time resolution, equal to 10 ps, which was subtracted in quadrature. The distribution along the sensor surface (A) shows a good uniformity, proven by the absence of non-gaussian tails in the 1D distribution on (B). The events with the poorest resolution are concentrated in the region of the sensor where the signal tends to be collected primarily by one pad, proving once again the goodness of the charge sharing.

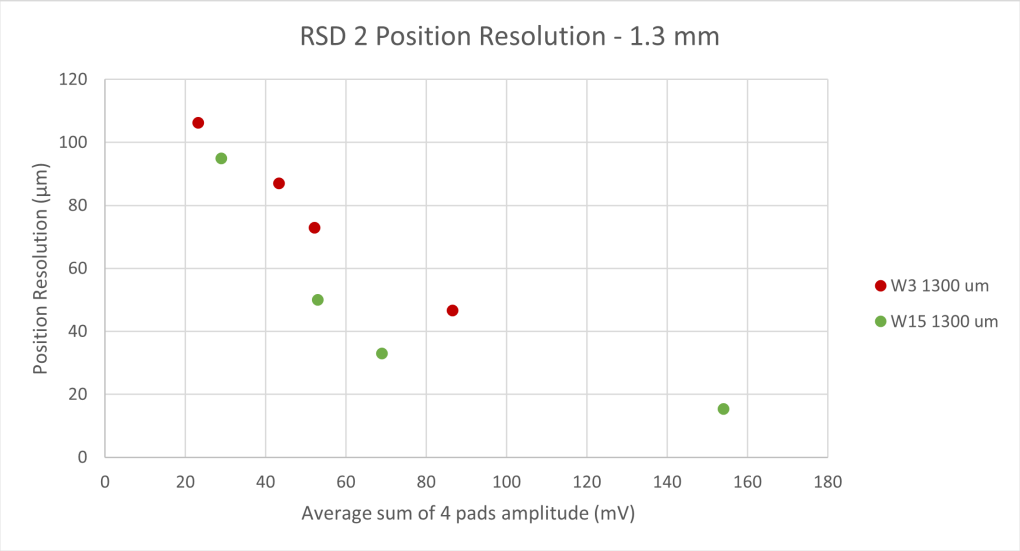

Figure 4.14: Position resolution of the 1.3x1.3 mm^2 devices from RSD2 obtained with the analytical method.

The time of the maximum has been used as t_{meas} (see Equation 4.10) for the analysis, which yields better results than the value obtained with the more commonly used constant fraction algorithm due to the limited number of samples on the signal rising edge. This feature is not linked to a specific aspect of the resistive read-out but rather to the digitizer's 5 GS/s sampling rate. These results indicate that resistive read-out does not degrade the timing performance of the UFSD design, and a very uniform response over large pixels is achievable. The result of this inquiry is presented in Figure 4.17. Since the Landau term is absent and the spatial resolution was proven excellent in the last Section 4.8, the time resolution is dominated by the jitter contribution. As visible in the figure, this holds for the DUT from wafers 7 and 15, whose time resolution fits the evolution of the time jitter for every pixel size measured. However, the sensors from W3 deviate from this trend and have significantly worse time resolution. The propagation over a resistive layer with a value of $n+$ can adversely affect the accuracy of time measurement, as evidenced by this observation. At the same time, this result can be due to a combination of the lack of sampling points on the waveform and the method employed to extract the t_{meas} in the analysis phase. In fact, the time at the peak is estimated from a fit of the waveform sampled points closest to its maximum, but the longer falling edge of wafer 3 in combination with the noise can make this value shift more in time than one of the other wafers. Such result could benefit from the use of a different acquisition chain: for instance a high-bandwith oscilloscope with high sampling rate could help in the determination of the signal time of arrival. Nonetheless, an exceptional value of time jitter at 55 mV of 15 ps for wafers 7 and 15, and 50 ps for wafer 3 was measured, demonstrating that the timing capabilities of UFSDs are maintained. In addition to the space resolution obtained in the previous section, this result proves how devices from Resistive Silicon Detectors are one promising candidate for future 4D

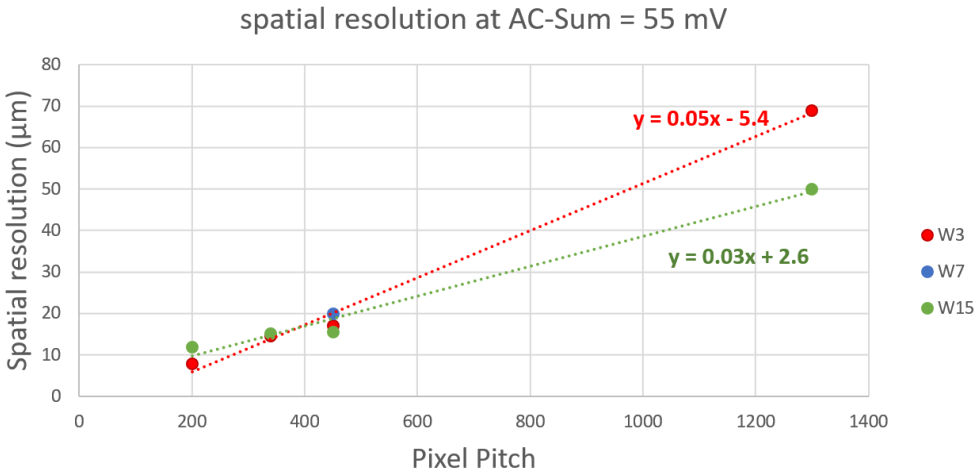

Figure 4.15: Position resolution at 55 mV

detectors.

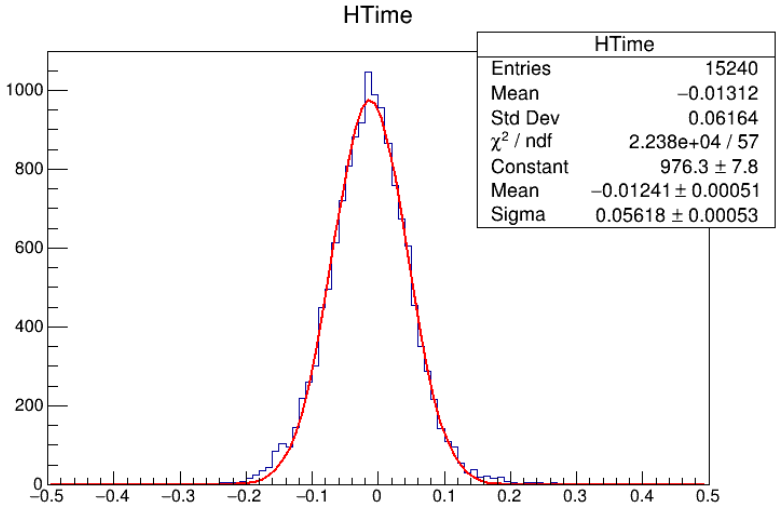

Figure 4.16: Time difference between the trigger time and the reconstructed event time on the pixel surface collected in a 1D histogram. The DUT is a 450x450 μm^2 from wafer 3.

4.5 Machine Learning Reconstruction

This section reports a parallel approach to position reconstruction in RSD2 based on Machine Learning (ML) techniques. The mechanism of charge sharing offers an ideal case to apply these techniques since it possesses the fundamental ingredients of such algorithms: given a specific input feature, i.e. the signal characteristics, a precise output is required, the hit position. In addition, the TCT setup allows taking a great amount of data to train the ML algorithm, necessary for the correct exploitation of this method. The ML approach to RSD position reconstruction has been proven perfectly suited and promising in the analysis of the RSD1 production devices [47], providing better results than a simple analytical model. The results reported in this work were published in [70, 50].

4.5.1 Devices Under Test and Reconstruction Procedure

The Devices Under Test (DUTs) employed in the ML approach differ from the ones measured in the analytical reconstruction previously described in Section 4.4 due to the ability of this approach to benefit from a larger number of read-out electrodes and, subsequently, features provided to the algorithm. All the devices come from wafer 15 of the RSD2 production described in Section 2.3 and share the same gain layer extension of 800x800 μm^2. Figure 4.18 displays the geometrical layout of such devices; they consist of a 3x4 array of pads disposed on the vertices of equilateral triangles with 200 µm sides (or pitch). Each device was given a name depending on the resemblance of the metal pads with some geometric figures: "crosses", "snowflakes" and "boxes" respectively from left to right in the picture. Each structure possesses 20 µm thick crosses, with a distance in between the crosses ranging from the 10 µm of the "snowflakes", through the 20 µm of

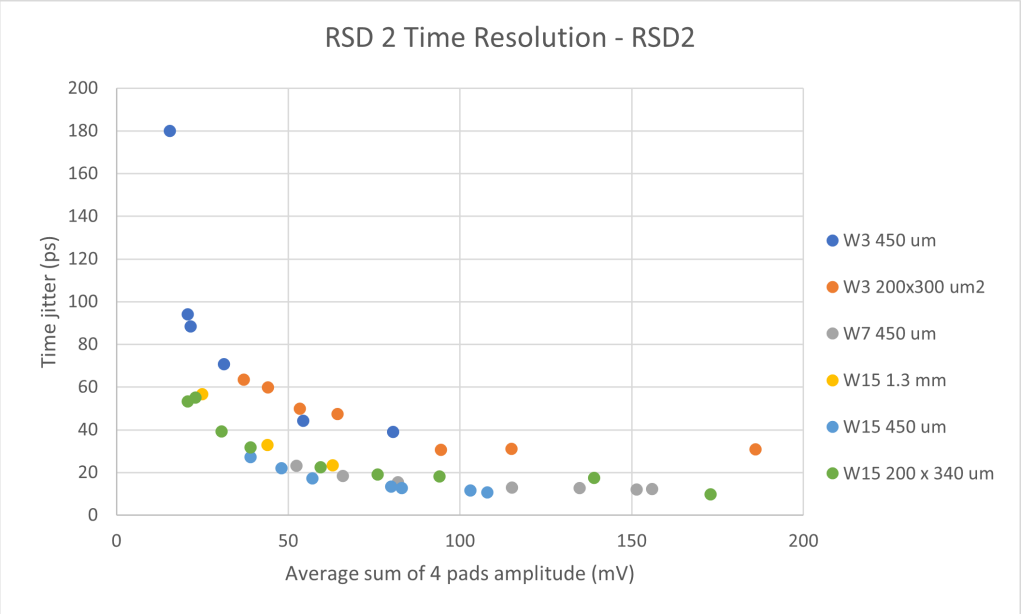

Figure 4.17: Time resolution of the RSD2 DUTs from the three different wafers.

the "boxes", up to the 100 µm of the "crosses".

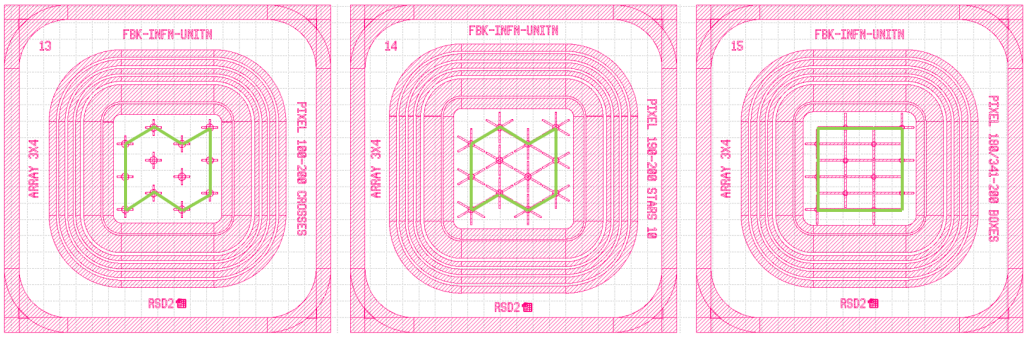

Figure 4.18: Geometrical layout representation of the devices used in the ML analysis. From left to right: "crosses", "snowflakes" and "boxes". The fiducial area is circled in green.

All 14 AC-pads and the DC contact were read out by the digitizer and exploited for position reconstruction. A fiducial area was defined for each sensor, based on where at least two signals are expected to be collected by the AC-pads and it is shown circled in green in Figure 4.18. The data acquisition was performed in the Turin Laboratory with the setup described in Section 3.4 with the laser intensity set to $\sim$ 5 MIPs and three different bias points were considered. All DUTs have been scanned with 10 µm steps on their whole active area, acquiring 100 waveforms for each position.

The methodology adopted for the reconstruction process is based on a standard data science pipeline: (i) first the raw data is processed to extract the signal features that form the dataset fed to the ML algorithm (*feature extraction*), (ii) then the dataset is split into two subsets, one is employed

for the training the model to fit the data (*training*), (iii) while the second is used to test the goodness of the fit (*test*). In the next paragraphs, each step of the pipeline is described in greater detail.

1. *Feature extraction*: the raw data undergoes processing based on a C++ algorithm able to extract features from the waveform collected on the 14 AC-pads. The events in the proximity of the metal pads and the wire bonds, i.e. where the laser is reflected, are discarded along with the ones with coordinates outside of the fiducial area. In this study, the amplitudes of the 14 pads are the feature used to predict the position and were organized in a tabular dataset containing the laser position of the hit and the 14 amplitudes. Mathematically, each event is uniquely described by a point $v \in \mathbb{R}^{14}$.

2. *Training*: training of the model is performed on a 20 % subset of the total dataset with random positions inside the fiducial area. The remaining 80 % subset is used to evaluate the reconstruction performances of the model, meaning that the two subsets are non-overlapping to better assess the generalization capabilities of the model. During the training procedure, the model learns to associate each point v to a certain set of coordinates (x, y). This split procedure was tried multiple times splitting randomly the two sets, obtaining the same results with a deviation completely negligible to the experimental error reported in the results. During the testing phase, the model will be required to make predictions for coordinates that were not utilized during its training, as is the case when the model is deployed. In the future, this approach will be utilized to predict the hit position from data obtained with particles employing the TCT dataset as training for the prediction. A Random Forest has been used as a regression model, consisting of multiple decision trees (100 in our case) trained in parallel. It should be noted that the x and y coordinates are predicted separately: the model consists of two Random Forests each predicting one coordinate using the same input data. In other words, for every event point v, $x_{pred} = f_x(v)$ is predicted by the first forest and $y_{pred} = f_y(v)$ from the second, the final prediction will be (x_{pred}, y_{pred}).

4.5.2 Experimental Results

Having obtained the predicted set of coordinates, the spatial resolution σ_{DUT} was computed by comparing them with the laser reference recorded in the data acquisition. The difference (x, y) - (x_{pred}, y_{pred}) between the two was recorded in a residuals histogram and then fitted with a gaussian distribution whose standard deviation represents the spatial resolution. The setup resolution was accounted for through

$$\sigma_{meas} = \sqrt{\sigma_{DUT}^2 + \sigma_{setup}^2} \tag{4.13}$$

where both the x and y coordinates contribute independently to the total DUT resolution since they are predicted separately. Hence

$$\sigma_{DUT} = \sqrt{\sigma_{DUT,x}^2 + \sigma_{DUT,y}^2}. \tag{4.14}$$

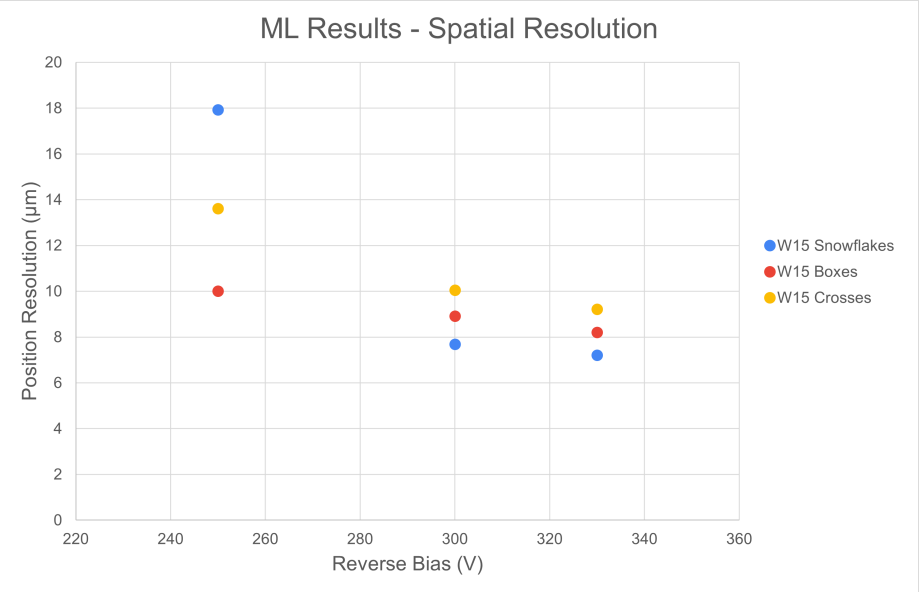

Figure 4.19: Spatial resolution as a function of the sum of the amplitudes. DUTs obtained with the ML approach

The setup resolution is difficult to estimate, it includes effects due to the eventual incorrect positioning of the stages, the not point-like charge generation inside the device due to the laser beam structure and eventual variations in the laser intensity. The repeated measurement of the same device brought to an estimation of this term so that the value $\sigma_{setup} \sim 2$ µm was used. A more precise estimate of this factor can be assessed with measurements on particle beams equipped with very precise tracking systems. The prediction results are very similar for both axis in all devices, with a maximum difference equal to ~ 1 µm for the minimum bias point.

In Figure 4.19 are illustrated the position resolutions obtained with the ML approach as a function of the bias voltage applied to the DUTs. The resolution is much lower than what would be obtained with traditional silicon pixels with 200 µm pitch. In fact, their resolution $\sigma_{trad} = \frac{pitch}{\sqrt{12}} \sim 58$ µm, while all DUTs reach a resolution < 10 µm.

4.6 DESY Test Beam Preliminary Results

The purpose of this section is to outline the methods developed to analyse the data collected from RSD2 devices during the DESY II test beam campaigns carried out in winter and spring 2022-2023. As the data analysis is currently underway, the spatial resolution achieved by one sensor is reported, but the result is not final and should be considered as preliminary.

The device tested consists of a RSD2 450 µm-pitch from wafer 6. A scheme of the bonds of the pad can be found in Figure 4.20. The device was bonded on a 16-ch FNAL board, whose description can be found in Section 3.5. Given the number of channels available on both the readout board and the digitizer, it was impossible to read out all the sensor pads. Therefore it was chosen to ground one pad on the rightmost column. To guarantee that the absence in the reconstruction of such a pad does not bias the resolution outcome, the region of interest in which the reconstruction is made is enclosed by the black square in the Figure.

The DUT was placed in between the two ADENIUM telescope portions in T24. A preliminary alignment of the DUT with respect to the telescope was obtained by maximising the coincidences between the DUT and the telescope planes, moving the DUT thanks to the PI stages previously mentioned. The DUT was then biased at 220 V, corresponding to the maximum safe reverse bias providable, being the breakdown point of this device around 240 V. The DUT data acquisition was made thanks to the CAEN digitizer described in the previous sections and the trigger scheme represented in Figure 3.14, illustrated in Section 3.6. It should be noted that the sensitive surface ratio between the trigger and the region of interest of the DUT is $\frac{ROI_{DUT}}{S_{MCP}} = \frac{0.81mm^2}{50mm^2} \sim 1\%$, meaning that high statistics is needed. For this reason, it was chosen to set the beam energy to 4.4 GeV to maximise the beam flux [71] and maintain an acceptable mean multiple scattering angle.

4.7 Data analysis

The data analysis was performed with the objective of confronting the spatial and time reference data with the DUT data to extract the time and space resolution. Since the DUT and MCP waveforms samples are stored in a file with a specific format, while the telescope data is stored in another raw file, it was first necessary to extract the valuable parameters from each one and proceed to confront them. The digitized waveforms of the MCP and DUT were processed with a C++ ROOT-based script completely analogous to the one described in Section 3.4.3, and the reader may refer to that Section for further details on the matter. On the other hand, the extraction of the telescope data from the raw file was performed by developing an ad hoc suite based on the use of the 4D track reconstruction software package Corryvreckan [72].

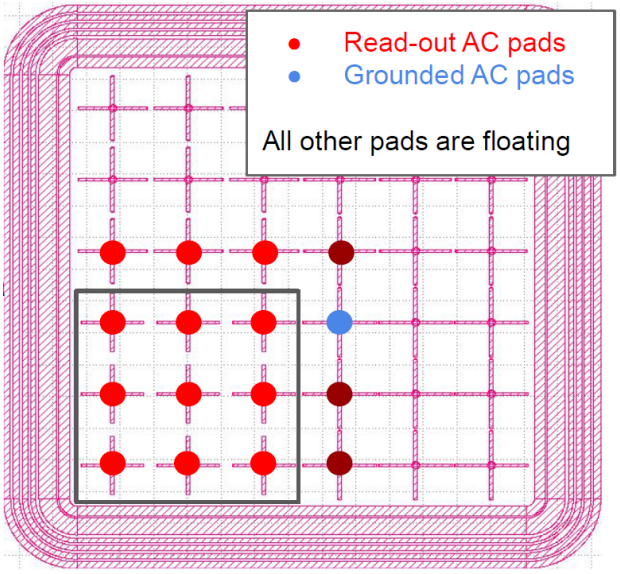

Figure 4.20: Bonding scheme of the 450 µm pitch sensor tested in the DESY II Test Beam Facility. The area of interest is enclosed in the black square (see text for further information).

4.7.1 Position Reconstruction

Given the multi-pad layout of the DUT, the position reconstruction was performed by computing the reconstructed position x_i as the mean of the pad positions weighted on the amplitude A_i^j seen by each pad j for a certain event i, as formulated in Equation 4.15

$$x_i = \frac{\sum_j A_i^j x_j}{\sum_j A^j} \tag{4.15}$$

This formulation allows to reconstruct the hit position without having any notion of which square of the pad is hit.

4.7.2 Telescope Data Synchronization

As already mentioned, instabilities on the busy signal generated by the digitizer and provided to the TLU as a trigger brought desynchronization of the DUT data with respect to the telescope data. In particular, it was observed that a secondary TTL signal is produced some µs after the end of the busy signal every 5k-10k events, with no apparent reason. Therefore, a method was devised to sync the data streams of the telescope and the digitizer. Such a method is based on the information provided by the TLU on the triggers timestamp and on the comparison of the distance of the event reconstructed by the DUT and the position projected on the DUT itself by the reconstructed track. Firstly, the position x_{pad}^i of the pad seeing the highest amplitude is assigned to each event i, then the difference $evt\_delta_{i,j} = |x_{pad,i} - x_{telescope,i}|$ is evaluated for events i spanning in the interval $j \in i + [-20, 20]$. By plotting (Figure 4.21) the evt_{delta}, it is possible to visualise the synchronised events since such a parameter is minimized,

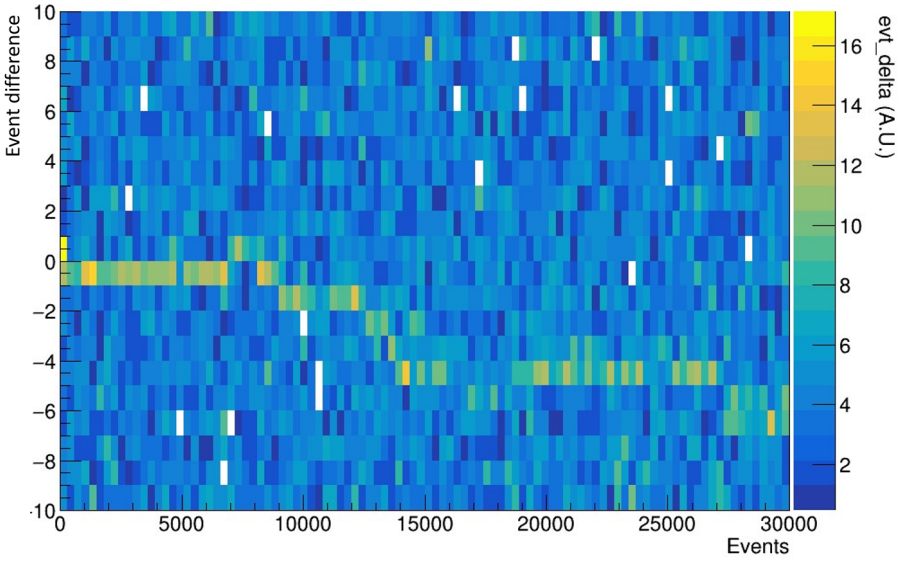

Figure 4.21: Histogram of the *evt_delta* parameter as a function of the event number. See text for more information. The points in which the *evt_delta* is greater (warmer coloured bins) indicate synchronization of the telescope and digitizer datasets.

on average, when the telescope and the DUT reconstruct the same particle passage. By comparing this information with the ones that possess a time difference between TLU triggers < 190 µs, it is possible to locate the exact event in which the desynchronisation occurs and correct this issue.

4.7.3 Telescope Resolution

The ADENIUM telescope resolution reported in [73] does not account for the configuration employed in this analysis due to the high material budget. In fact, two different DUTs were placed on the beam direction with corresponding PCB, amounting to circa 1.5 mm of both silicon and PCB. Therefore, it was decided to estimate the spatial resolution of the Telescope by employing a ExFlu wafer 1 LGAD [27] and fitting the amplitude distribution at the edges of the sensor. Assuming that the electrical field in region covered by the gain layer is constant and the transition to zero negligible compared to the telescope resolution, the sigma of an error function fitting the histogram illustrated in Figure 4.22 corresponds to the spatial resolution of the hit positions on the DUT reconstructed by the telescope.

Therefore, the telescope resolution in this configuration was estimated to be about 30 µm.

4.7.4 Results of the 450 µm position resolution

Once the datasets are synchronized, the spatial resolution was evaluated by comparing the position reconstructed by the DUT with the formulation expressed in Eq. 4.15 to the hit position projected by the track reconstructed by the telescope on the DUT. Some cuts were made on the data taken into

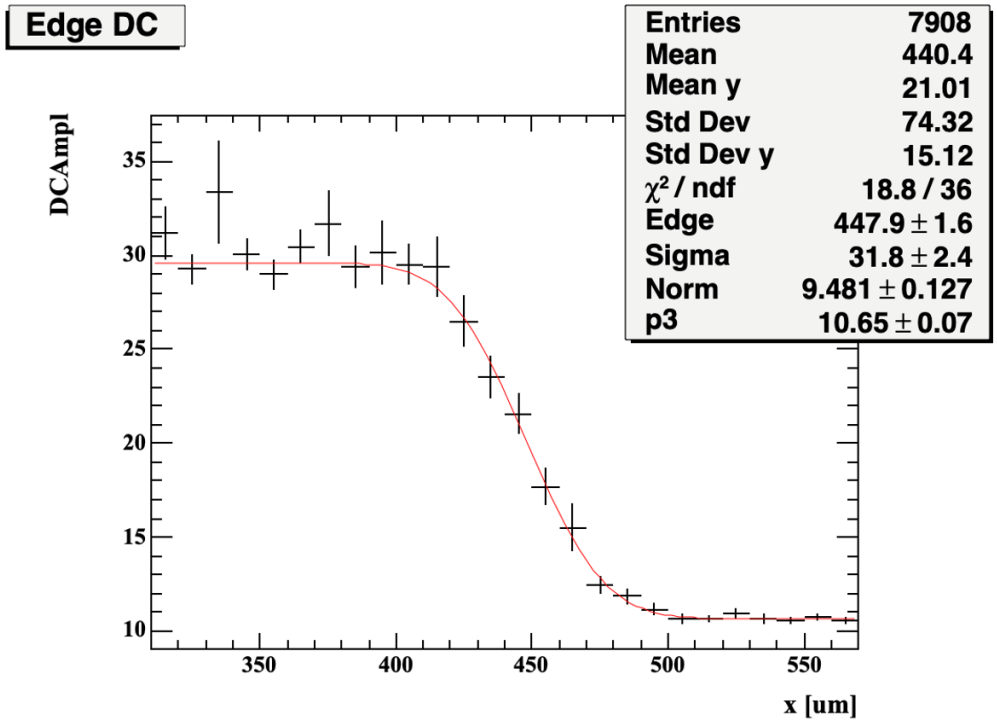

Figure 4.22: Signal amplitude at the edge of the device fitted with a conjugated error function (*Erfc* in the ROOT framework, [74]). The sigma of this function gives an approximation of the spatial resolution of the tracker.

consideration. In particular, the highest pad must see at least 8 mV in amplitude and the sum of the amplitude the four pads cornering the square in which the position is reconstructed should exceed 25 mV. An additional criteria to fine tune the reconstruction was included in the analysis: if an event has the amplitude of four pads that differ for less than 3 mV, i.e. it falls in between pixels, the position is reconstructed twice in the two neighbouring squares with the abovementioned formula and the final position is obtained as the average of the two evaluations. The dataset considered consists of circa 270k MCP triggers, with the DUT biased at 220 V, corresponding to a gain of about 25. After a first phase of correcting for the offsets of the two coordinates systems, one obtains the histogram depicted in Figure 4.23. The sigma of the gaussian fit is quite similar along both x and y -axis and is equal to $\sigma_{gauss} = 60$ µm. One can obtain the spatial resolution of the RSD2 sensor by subtracting in quadrature the telescope contribution to this number, since the telescope and DUT resolutions are completely uncorrelated, hence

$$\sigma_{pos,450} = \sqrt{\sigma^2_{gauss} - \sigma^2_{telescope}} \sim 51\mu m. \tag{4.16}$$

This and other results of these test beam campaigns indicate how the amplitudes of the signals are lower than what was expected, worsening the capabilities of these devices. Nonetheless the result reported is exceptional, achieving a ratio between the sensor space resolution and its pitch of about

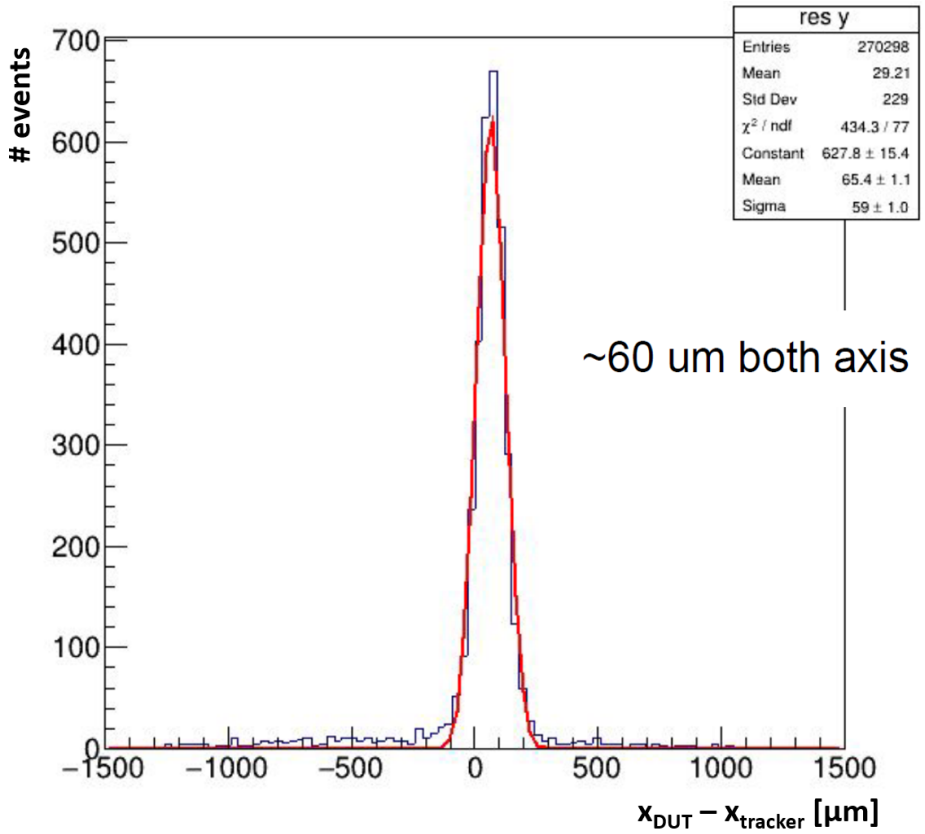

Figure 4.23: Hit position difference between the one reconstructed by the DUT (x_{DUT}) and track intercept on the DUT ($x_{tracker}$) along the y-axis. The data comes from the spring test beam in the T24 area of the DESY II Test Beam Facility.

1/9 on both directions transverse to the beam. A traditional pixelated silicon matrix with resolution $\sigma_{pos} \sim pitch/\sqrt{12}$ would need about 6.8 times the number of pixels to achieve the same result.

Further analysis on this device time resolution and on the rest of the DUTs tested is still underway.

The results described in this Chapter clearly demonstrate the validity of the RSD concept: the feasibility of a device with LGAD-like timing performances and spatial resolution with an unprecedented ratio $pitch/resolution$. In contrast with the RSD1 production, the RSD2 devices are able to deliver these performances over the whole sensitive area, proving that a better design of the geometrical disposition of the AC readout pads is central in charge sharing. Therefore, the RSD technology represents a promising solution on the road to a fully capable 4D tracking detector. As already mentioned in Chapter 0 of this thesis, the development of a fully 4D tracking-capable device should include the addition of technologies aimed at improving the LGAD radiation resistance, currently being designed on a parallel line of research.

At the same time, the RSD2 confirmed that some characteristics of the AC-coupled devices can represent an unnecessary complication. For example, the behaviour of the coupling oxide after irradiation is not well known and the distortion of the reconstruction (visible in Figure 4.11 limits the spatial resolution capabilities. A new approach based on DC-coupled contacts to the RSDs was devised for these and more reasons. The first simulations of DC-RSDs and the production layout are described in the next Chapter 5.

Chapter 5

DC-coupled Resistive Silicon Detectors

This Chapter introduces the new silicon device design conceived in Turin based on the Resistive Silicon Detectors technology. The DC-coupled Resistive Silicon Detectors are an evolution of the AC-RSD discussed in the previous chapters 2 and 4. A basic DC-RSD consists of an LGAD design with a single unsegmented p+ gain layer and an n+ layer on which the output signal is read through metallic pads (grey in Fig. 5.1). The need for a new concept of RSD arises from the difficulties met in trying to optimize the signal sharing and the occupancy of the detectors, as seen in the previous chapter. Further information on these matters and a description of this detectors fundamentals is reported in Section 2.1.2.

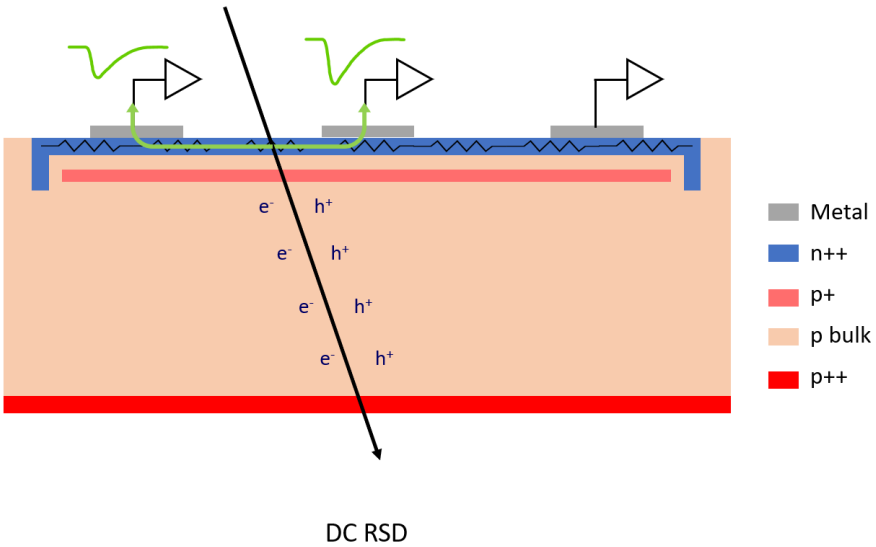

Figure 5.1: Schematics of a DC-RSD.

In the first section of this chapter, it is described how an innovative approach based on Weightfield 2.0 and LTSpice simulations was extensively applied for the first time to the DC-coupled RSD. The second part of this chapter illustrates the simulations performed in the more traditional TCAD tool thanks to the inputs of the hybrid approach. Finally, the layout of the

future DC-RSD production is reported.

5.1 A new hybrid approach to simulations

Traditionally, silicon sensor simulations have been carried out using TCAD-based software. This technique has the virtue of being exceedingly exact, however, it is very demanding in terms of computation time. The time needed for a 3D simulation increases very rapidly with the simulated volume, for example, the simulation of a 100 x 100 μm^2 pixel with a 50 µm thick active area takes about 10 hours. RSD sensor modelling is particularly difficult since the signal spreads across large areas, necessitating a 3D simulation of portions up to a few mm^2. Therefore, to be able to explore a larger number of variations a different type of approach was adopted. The simulation process is split into two steps:

1. the passage of a particle through the sensor bulk and the consequent signal formation

2. the charge spreading over the layer towards the read-out contacts placed at virtual ground.

The first step was performed exploiting the Weightfield2 (WF2) [75] software and the results became input of the second step, based on an LTSpice schematics simulation [41]. The complete simulation of both tasks takes less than a minute, drastically improving the scenarios that are possible to explore.

5.1.1 Weightfield2

The Weightfield2 simulation program was created to better understand the properties involved reproducing the desired square resistance values predictions to laboratory measurements. It has been instrumental in the design and evaluation of UFSDs and has a user-friendly graphical user interface with different areas. The user has the possibility of choosing an external stimulus such as MIP, laser and alpha particle, the irradiation level, and the presence of a magnetic field. Also, the characteristics of the sensor itself can be tuned by changing its physical dimensions, the characteristics of the gain layer, and the operating bias voltage. The Weightfield2 (WF2) simulation program has been adjusted to accurately reproduce the signal produced by a Minimum Ionizing Particle (MIP) hitting a silicon sensor. As the signal formation in DC-RSD is similar to that of a standard LGAD, the current stimulus can be obtained by simulating the signal in a more traditional UFSD sensor of the same thickness (50 µm). The parameters used in the WF2 program were those of the W13 from the FBK UFSD3.2 production [76], biased with a voltage of -200 V. The resulting current signal was recorded and utilized in the subsequent step.

5.1.2 LTspice

To simulate the signal spread over the sensor surface in DC-RSD, Analog Devices LTspice schematics simulation tool is utilized, where electrical components represent the key elements of the detector. The resistive sheet, i.e.

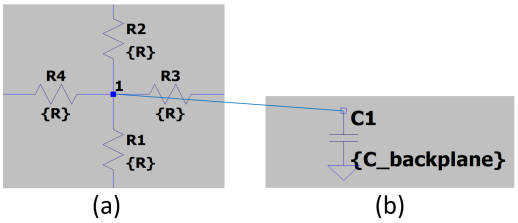

Figure 5.2: Scheme of the LTspice simulation fundamental block.

the $n++$ layer, is represented by a network of resistors, the sensor bulk by capacitors, and the front-end electronics by resistors approximating the read-out input impedance. A fundamental block of the detector modelization, as shown in Fig.5.2, consists of a node connected to four resistors and a capacitor connected to the ground. The typical values for the sheet resistivity and bulk capacitance are a few kΩ/sq and a few fF, respectively, and the capacitance is calculated based on a parallel plate capacitor model, being $C = \epsilon_0 \epsilon_r \frac{A}{d}$, where A is the area covered by the node, d is the detector thickness, and $\epsilon_0 \epsilon_r$ is the silicon dielectric permittivity. The simulated sensor has a squared layout with a side of 340 µm covered with 15x15 blocks unless otherwise specified.

5.1.3 Resistive plane

The first step consisted in reproduce the desired values of square resistance in the LTSpice environment. A grid of 2x2, 3x3, 4x4 and 15x15 nodes with 4 resistors each attached was modelled as visible in Figure 5.3. A voltage potential was applied, scanning from 1 up to 100 V, to the two sides of the matrix and the current flowing through the generator measured. The square resistance of the matrix was evaluated thanks to Ohm's first law and measured for each matrix tested. With constant values of the single resistors, it resulted that the square resistance is the same among the different grids tested, as expected.

5.1.4 Position Reconstruction

The performance of DC-RSDs is evaluated by measuring their spatial resolution. The signal obtained with WF2 (see paragraph 5.1.1) is injected in each node of the resistive plane, the positions are reconstructed and compared with the real ones.

The position is reconstructed by employing a simplified version of the DPC model (see Section 4.2), which computes the amplitude imbalance of the signals measured at the four corners of the resistive plane (the four red dots in the picture on the left of Fig. 5.4). The x-y coordinates are determined as:

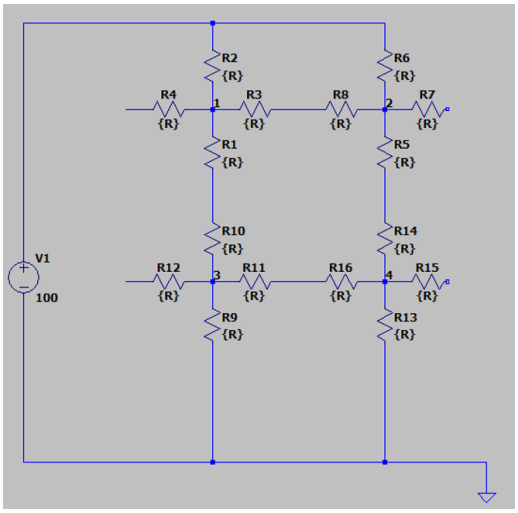

Figure 5.3: Example of the simplest resistive sheet grid. The electric potential was unbalanced providing 1-100 V and the current flowing through the voltage generator was registered.

$$\begin{aligned} x &= \frac{A_2 + A_3 - A_1 - A_4}{A_{tot}} \\ y &= \frac{A_1 + A_2 - A_3 - A_4}{A_{tot}}, \end{aligned} \tag{5.1}$$

where A_i is the signal amplitude at the i-th corner and A_{tot} is the sum of the four amplitudes. This approach to the reconstruction was maintained constant throughout all simulations.

To further match a real-life scenario, the signal at each read-out pad is read through the resistors representing the amplifier boards and amplified with a trans-impedance of 4700 Ω, typical of a Santa Cruz board with the addition of a second stage 20 dB amplifier by Cividec described in Section 3.5 and most commonly used in the Turin Laboratory. Gaussian smearing with 2 mV RMS was added to each amplitude value to reproduce the effect of the noise typical of these amplification chains.

5.1.5 Optimization of the DC-RSD Design

In order to optimize the DC-RSD designs two goodness-of-reconstruction parameters were defined. The first measures the accuracy of the reconstruction, i.e. the average of the distances between the reconstructed point and the original one. The second parameter estimates the dispersion of the reconstructed positions around their mean value. In formulas:

- **Average point accuracy** d, defined as in the following equation (eq. 5.2)

$$d_i = \frac{\sum_{n=0}^{N} |\vec{x_r^{n,i}} - \vec{x_o^i}|}{N}, \quad d = \frac{\sum_{i=0}^{N_{nodes}} d_i}{N_{nodes}} \tag{5.2}$$

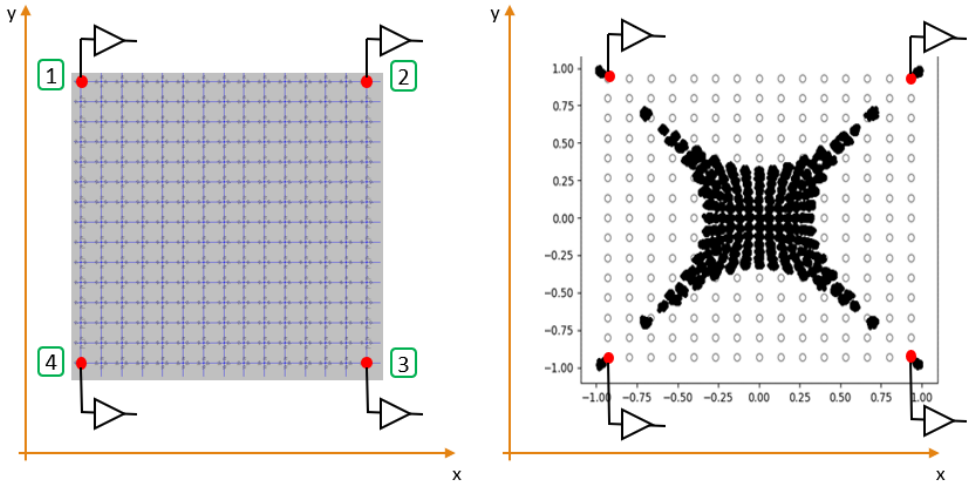

Figure 5.4: Left: simulated configuration. Right: true (empty circles) and reconstructed positions (full circles) of this simulation.

where i is the node index, $\vec{x_r^{n,i}}$ the reconstructed position and $\vec{x_o^i}$ the injection one, N the number of trials per node, N_{nodes} the total number of nodes.

- **Mean reconstructed position dispersion σ**

$$\vec{x_{avg}^i} = \frac{\sum_{n=0}^{N} \vec{x_r^{n,i}}}{N}, \quad \sigma = \frac{1}{N_{nodes}} \sum_{i=0}^{N_{nodes}} \frac{\sum_{n=0}^{N} |\vec{x_r^{n,i}} - \vec{x_{avg}^i}|}{N} \tag{5.3}$$

Three different designs of the DC-RSD were simulated and evaluated: (i) read-out pads at the 4 corners, (ii) read-out pads at the 4 corners connected via a grid of constant resistors, and (iii) read-out pads at the 4 corners connected via a grid of variable resistors. All configurations were evaluated through the minimization of the parameters just defined.

In addition to the spatial resolution, one also wants to minimize the time resolution. This is obtained by ensuring that the signals have high dV/dt, i.e. have high amplitude and short rising time, for equal noise level [67], as described in Section 1.4.1 of this work.

Read-out pads at the 4 corners

This first DC-RSD configuration has been implemented with a sheet resistivity typical of the FBK RSD1 and RSD2 productions, i.e. about 1 kΩ/sq, and the capacitance of each node is 1.29 fF, tuned to represent a 340 µm-wide squared sensor surface, with a distance in between the pads nodes of approximately 317 µm along the square sides. The left pane of Fig. 5.4 shows the simulated configuration while on the right pane the true (empty circles) and reconstructed (full circles) positions of the signals. The distortion visible on the right picture in Fig. 5.4 is typical of detectors with resistive read-out, and it has already been described in literature [66] and

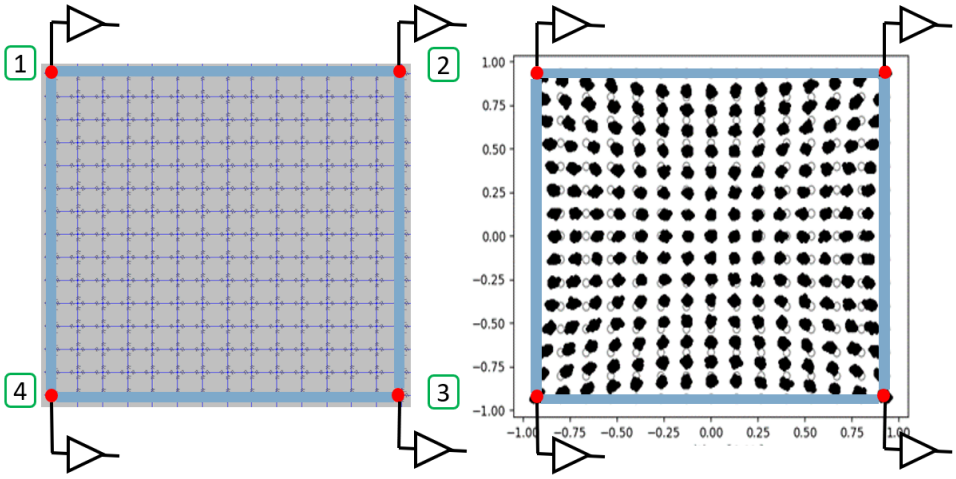

Figure 5.5: Low resistivity strips connecting the electrodes. Left: simulated layout. Right: true (empty circles) and reconstructed positions (full circles) in this configuration.

was already noticed in the RSD2 batch dynamic characterization described in the previous Chapter 4.8. It is noticeable by eye how the reconstructed positions do not overlap with the true ones, therefore new solutions should be explored. The distortion is the product of having signals amplitudes very similar in every region of the detector. In [66], it was suggested that connecting the neighbouring pads could compensate for this effect by providing a path to the amplifier lane with lower impedance and, therefore, absorbing a greater part of the charge for events close to the sensor edges. Connecting the readout pads comes with the advantage of insulating one pixel from its adjacent. In this way, it is more likely to have high enough signals, i.e. whose amplitudes are larger than the noise level and can participate in the position reconstruction, and the sensor could be suited to higher occupancy applications.

Read-out pads at the 4 corners connected via a grid of constant resistors

A series of constant resistance resistors are then introduced to connect the neighbouring read-out pads with resistance much smaller than the ones of the resistive sheet, i.e. $R_{strip} << R_{sheet}$. It was observed that the introduction of such strips strongly improves the reconstruction since the signal is shared in a more balanced way, at least according to equation 5.1 (see Fig. 5.5). The value of resistance of the single resistors was tuned to ensure the isolation in between different read-out channels and the connected amplifiers. Therefore, a total resistance of each strip of at least 10 times the amplifiers input impedance was kept as the minimum value of these tests. Figures 5.7 and 5.6 contain the evaluation of the two parameters for this configuration as a function of the strip linear resistance and the sheet resistance. Each point on the graphs corresponds to 225 injections (simulations) of the signal, one for every node,

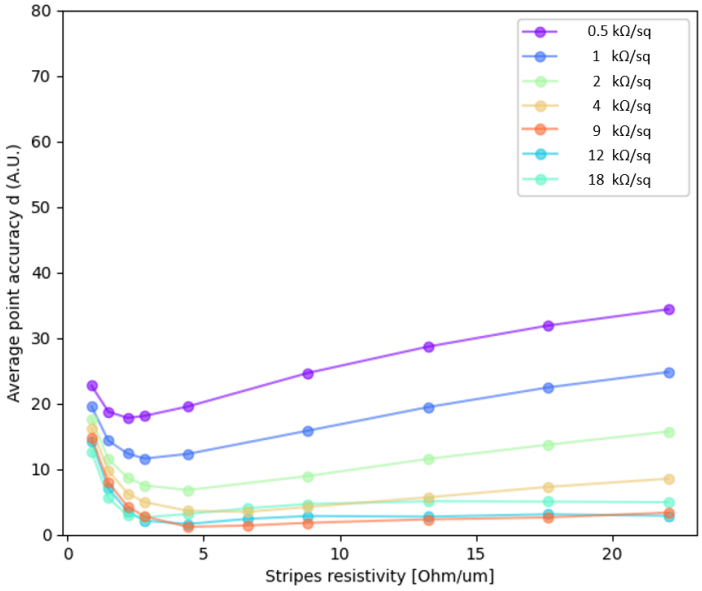

Figure 5.6: Average point accuracy as a function of the strips linear resistance and the sheet resistivity (see labels).

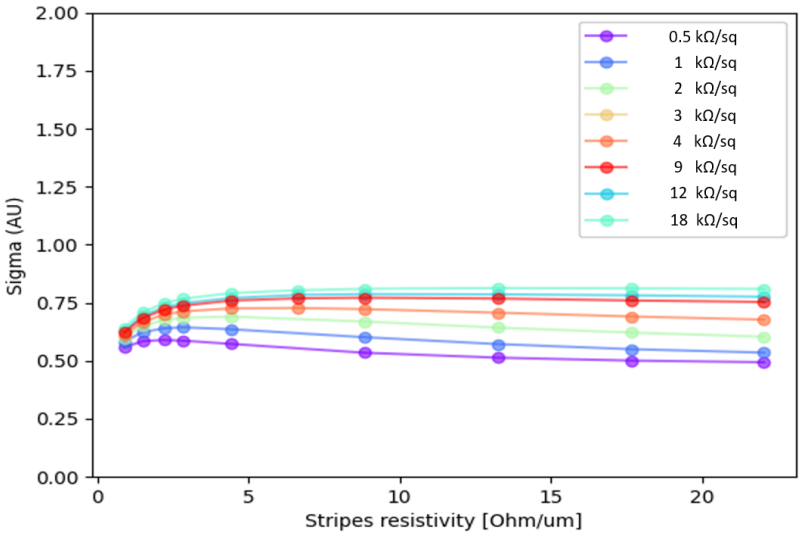

Figure 5.7: Sigma parameter as a function of the strips linear resistance and the sheet resistivity (see labels).

Several considerations can be made from these results: (i) the best value of the strip linear resistance increases weakly with the sheet resistivity. Overall, the minimum d is localized around values of strip linear resistance $R_{strip} = 1 - 3\ \Omega/\mu m$, corresponding to an integrated resistance in between the pads of $R^{tot}_{strip} \sim 320 - 950\ \Omega/\mu m$; (ii) higher sheet resistivities lead to smaller average point accuracy d; (iii) the mean dispersion σ is practically constant in all configurations.

Thanks to these outcomes, an ideal value for the strip resistance was found in $R_{strip} = 3\ \Omega/\mu m$, we studied the shape of the signals as a function of the sheet resistivity. This analysis shows that the shape of the output signals tends to become smaller and longer for high sheet resistivity, worsening the timing capabilities (see Fig. 5.8. The same was observed in the RSD2 analysis of wafer 3 performances (see Section 4.4,

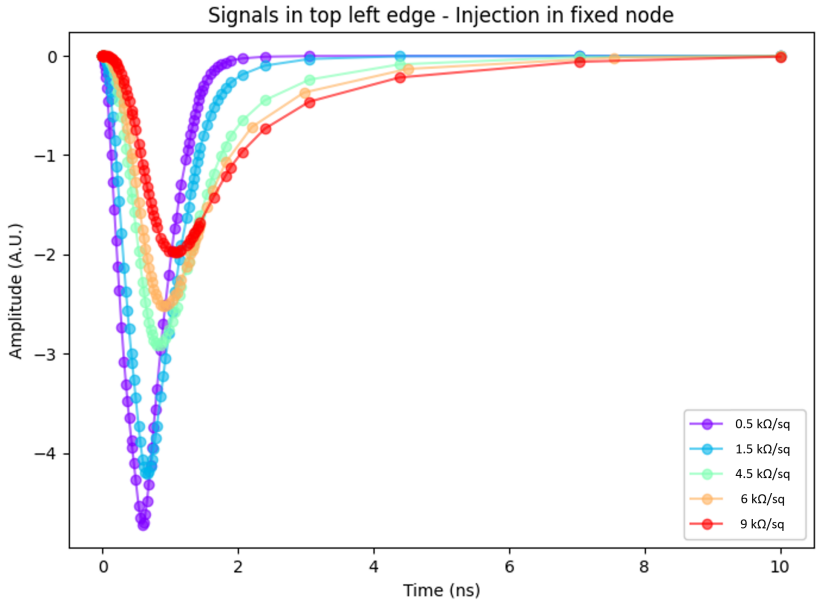

Figure 5.8: Signals picked up in a single electrode in sensors with different sheet resistivity.

Therefore a sweet spot for the parameters at hand in this configuration consists of a sheet resistivity $R_{sheet} = 3\ k\Omega/sq$, which maintains a sharp signal, and a strip resistivity of about $R_{strips} = 2.5\ \Omega/\mu m$ for a 340 μm-wide detector. Such configuration ensures that the signal is shared between four read-out pads and provides the reconstruction pattern visible in Fig. 5.5 (*right*).

Although already much improved, a residual of the distortion pattern is still noticeable. In particular, the reconstructed positions are still systematically shifted with respect to the true positions, even when the optimal strip resistance is implemented. The points tend to cluster slightly towards the sensor centre indicating that too much charge is still reaching the far electrodes when a signal is shot near the edges, especially close to the sides mean position.

Read-out pads at the 4 corners connected via a grid of variable resistors.

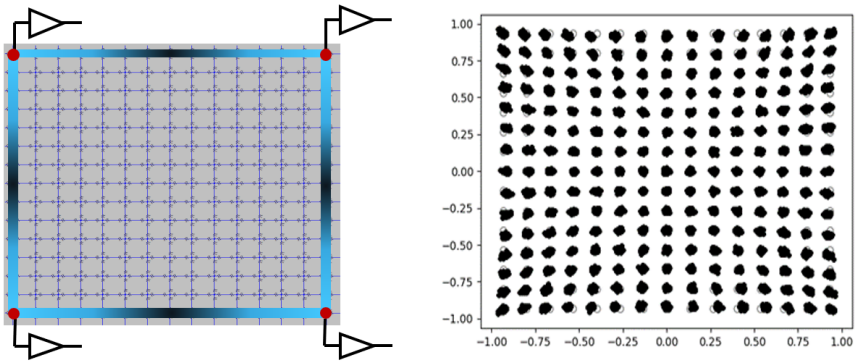

Figure 5.9: Left: a sketch of the variable resistance strips solution. Right: best reconstruction obtained in this configuration (see text for more detailed information).

In [66], it is suggested that connecting the pads with low resistivity paths consisting of arcs of a circle would theoretically compensate for this deformation. It was thought to reproduce this effect by varying the strip resistance along its length. This line of thought brought to the third and last configuration of this study. The strip resistance is increased near its centre and reduced towards the read-out electrode. In this way, a favourable resistive path is created towards the closest pads, while the signal sees the furthest ones as less favourable to reach. A sketch of this solution is drawn on the left pane of Fig. 5.9. The preferred variation of the resistance consists of a gradient depending linearly on the position whose extremes were varied in order to find the best spatial resolution. The best results were obtained with a resistive sheet $R_{sheet} = 3\ k\Omega/sq$ and strip resistivity in the range $R_{strip} = 1 - 10\ \Omega/\mu m$ with a variation of 25% - 50% along the strip length. It is important mentioning that this last setup produces reconstructed points that closely match the original ones. FBK is currently conducting internal tests to verify the feasibility of implementing low-resistivity strips on silicon.

5.1.6 The effect of pixel size

In the last part of the analysis, we studied how the size of the pixel impacts the performance. Its lateral dimension, or rather an area, can be tuned by changing the backplane capacitance, the only parameter which depends on the physical extension of the device in the LTSpice simulations. The explored dimensions range from 130 μm to 1 mm and the resulting waveforms are shown in Fig. 5.10. The signals maintain a sharp rising edge and almost the same amplitude. This study agrees well with our experimental finding that signals propagation on a resistive sheet with $R_{sheet} = 1 - 3\ \mu\Omega/\mu m$ does not significantly change the signal shape [77, 78].

From these results, it is possible to conclude that a DC-coupled sensor with large pixels (up to some mm^2) is in theory feasible. The spatial resolutions typical of RSD2 could be improved, along with the detector occupancy

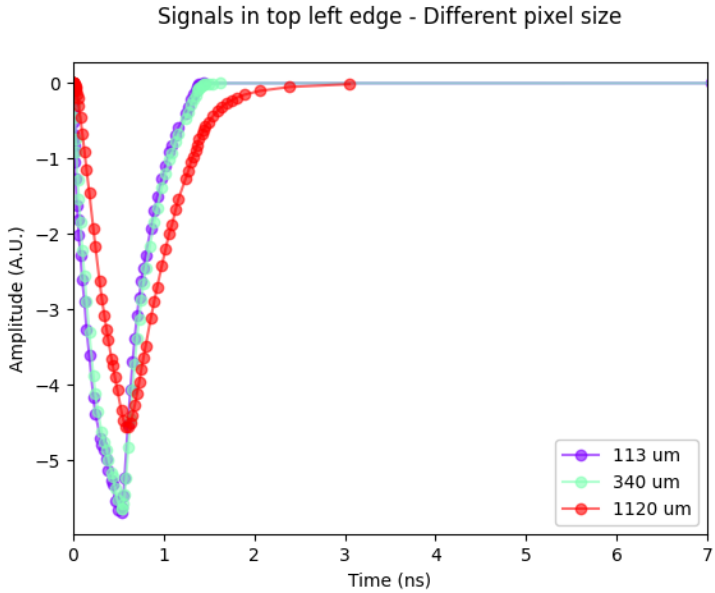

Figure 5.10: Variation of the waveform shape with the pixel size. The injection node is fixed.

thanks to the DC-coupled pads and the presence of resistive strips connecting them. The expected time resolution is the one typical of UFSDs, as already proven by both RSD1 and RSD2 batches if the proper sheet resistance is chosen, depending on the desired sensor size.

5.1.7 TCAD Simulations

The parameters obtained from the hybrid WF2+LTSpice approach were provided as input to a full TCAD simulation of the device 3D volume performed in by the INFN Perugia group [79]. With this tool, it has been carried out the full modelization of the various implants needed to produce the ideal characteristics described in the previous sections. After this initial calibration, the TCAD model was tested with the passage of a simulated MIP through the depleted, impinging on a subset of points represented in Figure 5.11 (*right)*. The position was reconstructed employing the same simple formulation described in Equation 5.1. .

The results obtained with this complete approach to the simulation confirm what was found in the hybrid simulations, finding better spatial reconstruction performances with the introduction of a low resistivity strip connecting the read-out pads. The TCAD simulations are being perfectioned by the INFN Perugia group to obtain the best configuration in terms of both performances and process feasibility.

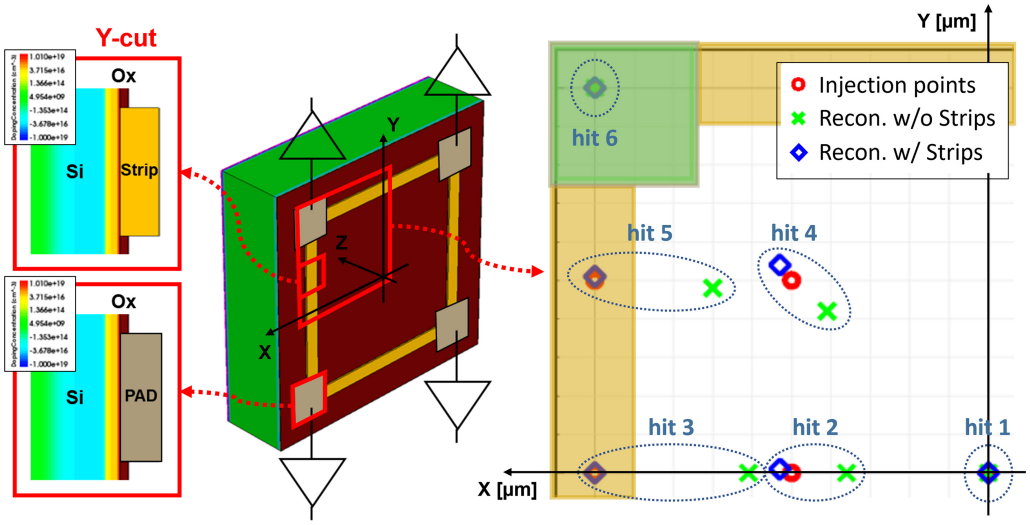

Figure 5.11: 3D rendering of the DC-RSD simulated in TCAD (*left*), Both the connecting strips and the pads are in direct contact with the $n{+}{+}$ layer, as shown in the magnification on the left. The *right* side of the pane shows the different positions of the injected (red) and reconstructed positions. The positions reconstructed in the case of a device without strips are marked in green, while the ones reconstructed with the strip layout are indicated in red. The Figure was taken from [79].

Chapter 6

Outlook: Future DC-RSD Production and Conclusions

6.1 Future DC-RSD Production

Given the promising results provided by the RSD batches illustrated in Chapter 4, in agreement with the SPICE and TCAD simulations described in the last Chapter, it was decided to proceed with the production of a batch of DC-coupled Resistive Silicon Detectors (DC-RSD). Preliminary work with Fondazione Bruno Kessler was initiated to assess which technologies were ideal for this application and to design the optimal layout of the pads and the resistive stripes previously described. Several technological challenges are involved in the actual production of these sensors, from the resistance of the contact between the $n+$ layer and the DC-pads to the realization of the strips with the desired resistivity. Being dedicated to the study of signal sharing in DC-coupled pads, the DC-RSD production by FBK will have internal structures very close to the ones of previous RSD productions. For instance, the gain and resistive layer ($n++$ implant) will have doses almost identical to the ones that were used for the RSD1 and RSD2 batches (reported in Table 2.2), the wafer substrate will be epitaxial, and no wafer will have a carbonated gain implant. This approach will allow to isolate free parameters and concentrate the efforts on the new technology.

On the other hand, two distinct sub-batches are planned based on different geometrical layouts and the type of contact between the DC-pads and the $n+$ resistive layer: aluminium only and Ti-TiN. One will be dedicated to a more simplified version of the DC-RSD, employing technologies well known to FBK, with electrical contact with the resistive layer granted by a thin layer of aluminium. The second aims at implementing the strip design with a constant and variable resistance along their length, bringing benefits in the reconstruction phase described in the previous Chapter. Both these batches will undergo the same diode definition, while their production process will diverge with the implantation and depositions that determine the more superficial characteristics.

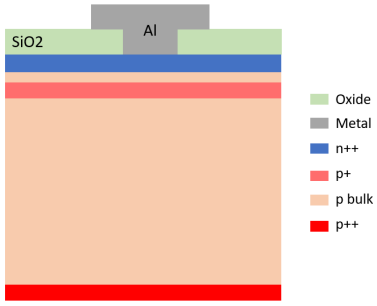

Figure 6.1: Scheme of the electrical contact between pad and resistive layer in the aluminium portion of the DC-RSD production.

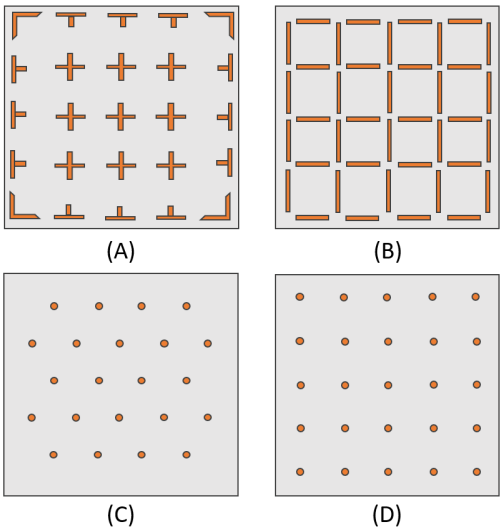

Figure 6.2: Examples of structures that will be implemented in the DC-RSD production with aluminium contacts. Each sensor is meant for studying the optimal pad disposition for charge sharing. See the text for further details on this matter.

6.1.1 Aluminium only contact

The aluminium part of the DC-RSD production is based on a technology which has been employed by FBK on LGAD since they started producing those sensors. The electrical contact between the silicon and read-out pad is provided by a thin film of aluminium deposited inside the $n{+}{+}$ layer through an opening in the oxide coating, as shown in Figure 6.1.

The geometrical layout of the pads should be adapted to this version of the contacts in order to take into consideration the presence of metal with virtually no resistance on the detector surface. In practice, the Al-Si interface has its own non-zero contact resistance, which depends on multiple factors, among which the interface area and the $n{+}{+}$ doping. Currently, preliminary tests are being made internally in FBK to achieve the desired contact resistance over small surfaces of the order of 10 Ω.

In Figure 6.2 are illustrated four possible structures with various metal pads. The (A) layout is very similar to the devices implemented in the

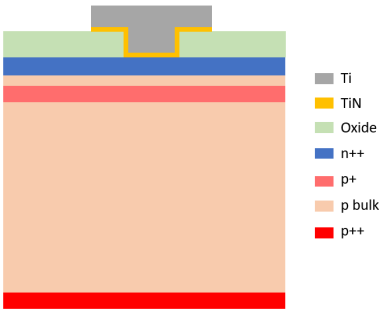

Figure 6.3: Cross section of a Ti-TiN contact with the $n++$ layer of the DC-RSD production.

RSD2 batch and serves the purpose of comparing the charge sharing in AC- and DC-RSDs. In (B) is implemented a different concept based on the dependence of the jitter on the number of channels n employed for the spatial reconstruction as $\sqrt{n}$ (see Section 4.2). With this layout, only two pads would concur in the computation of each coordinate, and the jitter term should play a minor role. The last two devices (C) and (D) are meant to extrapolate the optimal number of pads for the coordinate reconstruction and confirm the jitter dependency and study the signal behaviour with DC-coupled pads if the current is not constricted in a limited space.

6.1.2 Ti-TiN

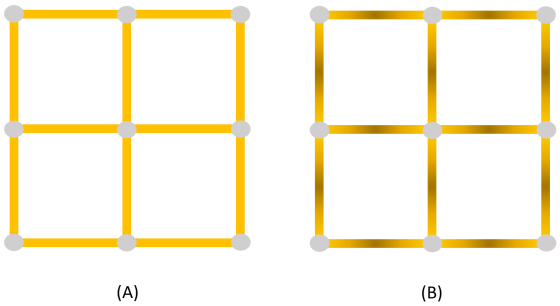

Figure 6.4: Examples of structures that will be implemented in the DC-RSD production with aluminium contacts. Each sensor is meant for studying the optimal pad disposition for charge sharing. See the text for further details on this matter.

The second option consists of a technology well known in micro-electronics and known for its low contact resistance and commonly employed in CMOS contacts [80] and, more recently, solar panels [81]. The interface between the metal and the resistive layer is coated with a very thin layer of Titanium Nitride, a ceramic gold-like material. At the interface with silicon, it mixes with it forming a Silicon Titanium Nitride alloy, electrically conductive and capable of blocking the diffusion of metals that are deposited on it. In fact, a second layer of titanium plus the addition of another metal is added on top of this film (see Figure 6.3) to provide a bonding base for wiring. With

this method, very low contact resistance per square can be achieved, down to some $m\Omega/cm^2$ [82, 83, 84].

Such technology can be exploited to produce devices with the correct resistance of the resistive strips described in the previous chapter and sketched in Figure 6.4. Device (A) possesses strips with constant linear resistance, while in (B) the colour gradient symbolizes the change in resistance along its length. In this layout, variations of each parameter will be implemented, from the pitch in between the metal pads to the width of the strips and, therefore, their resistance.

At FBK, multiple internal short-loop productions are being made to test and qualify the new technology needed to produce this kind of contact with the desired resistance before the actual DC-RSD processing.

6.2 Conclusions

The work presented in this thesis focused on the development of resistive silicon sensors for 4D trackers. These sensors provide promising results in terms of both temporal and spatial resolutions while employing a low channel density thanks to a design based on charge sharing among neighboring readout pads. The Resistive Silicon Detectors (RSD) analyzed in this thesis have been produced at FBK in two productions, RSD1 and RSD2. In both productions, the sensors are designed with an AC-coupled readout. The results obtained with the first batch of RSD, Chapter 2 provided insights on designing the RSD2 production, which employs a redesigned disposition and shape of the readout electrodes. RSD2 devices were tested with a wide array of experimental techniques, explained in Chapter 3. These techniques were developed by considering the special needs of large sensors with a resistive surface. For example, a fully automated data collection system employing a large-area TCT scan associated with 16 channel DAQ system was developed to test the sensors in the laboratory, while at the DESY test-beam site, this DAQ system was adapted to include the information from the tracking system to identify, over a rather large area, the particle impact point, Chapter 4.

Two approaches to the data analysis were followed: one is based on an analytical procedure, while the other is based on Machine Learning algorithms. Both methods deliver a very good spatial resolution, about 4-5 % of the pitch size, for structures pitches varying from 200 µm to 1.3 mm. Comparing the performance of devices with different resistivity, the tests demonstrated that for small pixels, sensors with higher sheet resistivity yield to better resolutions while, conversely, for large pixels, lower sheet resistivity brings better results. The TCT results also show that the temporal resolutions typical of the LGAD devices are maintained in the RSD sensors. Lastly, several test beams were carried out, the description of one of them performed at the DESY II Test Beam facility is reported. The results are in line with what was observed in the laboratory and confirm the validity of the AC-coupled RSD design.

The need to address issues encountered in the reconstruction of AC-coupled RSD data, namely the loss of position resolution due to signal

sharing over too many electrodes, led to developing a new evolution of the RSD design: the DC-coupled RSD. Besides the trivial change in the read-out coupling, from AC to DC, the new design allows extracting the signal current at the read-out electrodes, therefore limiting its spread to far away electrodes. The simulations of these new designs, performed with a fast and innovative hybrid approach that exploits SPICE and Weightfield2, are described in Chapter 5. Thanks to this new tool, a large number of ideas were tested, and the most promising configurations were identified. Subsequently, these limited number of configurations were tested using TCAD-based simulation. This two prongs approach allows therefore limiting the number of the TCAD simulations as each simulation can last up to 24 hours. These studies are the base of the first production at FBK of DC-RSD, described in Section 6.1.

The studies reported in this thesis demonstrate that the RSD technology is a valid candidate for future 4D tracking systems; the results bring the development of a 4D tracking detector one step closer to being usable on a large scale in future high Energy Physics experiments.

Appendices

Appendix A

Test Beam campaigns

In order to explore a more practical application of Resistive Silicon Detectors, an extensive campaign of characterization on particle beams is currently being carried out. In this section of this thesis are described the efforts spent towards finding a proper testing site, the creation of an interface with the instruments provided onsite and the configuration of an experimental setup tailored to the unique attributes of the RSDs.

The beam tests should be performed in facilities with some fundamental qualities to properly inspect the characteristics of the RSDs:

- Being equipped with a particle tracker sufficiently accurate not to dominate the spatial resolution of the system composed by the Device Under Test (DUT) and the tracker itself.
- Provide particles with a momentum high enough to deposit energy inside the detector as a Minimum Ionizing Particle (MIP). High momentum p particles also reduce the multiple scattering due to the interaction with the various components along the beamline, since the angular dispersion $\theta_0 \propto 1/p$.
- The compatibility of the setup described in section 3.4.3 to the equipment provided by the facility to better confront the data acquired in the laboratory with the laser and in situ with the particle beam.

Among the few facilities that present these characteristics, two were preferred: the Deutsches Elektronen-Synchrotron (DESY) and the Super Proton Synchrotron (SPS) Test Beam facilities. Both installations provide micron-level precise trackers with high energy particles, electrons or positrons with momenta up to 6 GeV at DESY and protons with momenta up to 120 GeV at SPS. Being this an evolving and still ongoing effort, in this thesis it is reported the first part of this inquiry, consisting of the tests performed at DESY.

A.1 The DESY Test Beam Facility

The Test Beam facility provided in the DESY campus at Hamburg-Bahrenfel comprises three distinct beam lines providing electrons or positrons with momenta selectable in the range from 1 up to 6 GeV. A detailed description

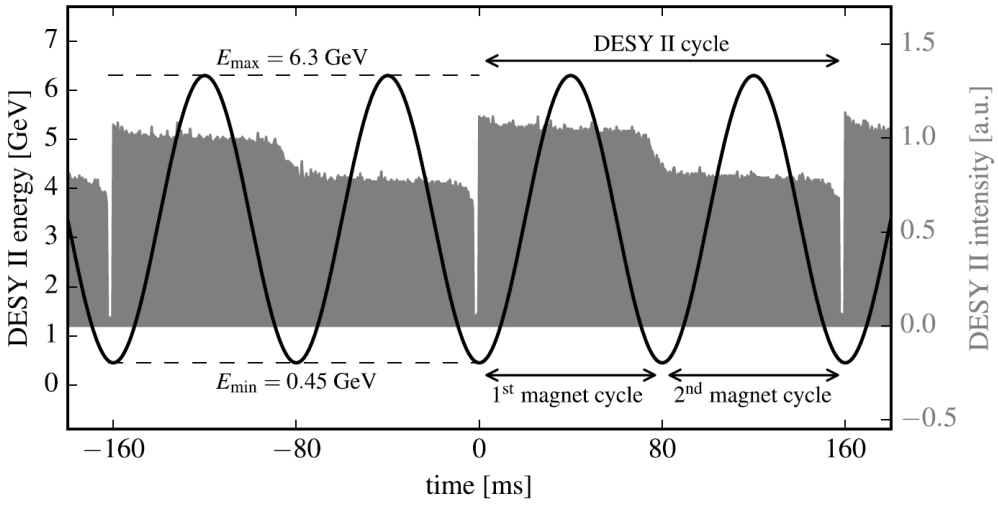

Figure A.1: Depiction of the DESY II sinusoidal beam energy (left y-axis, black) and its beam intensity (right y-axis, gray) as a function of time. The beam intensity during the second magnet cycle tends to be smaller due to losses caused by the deceleration down to E_{min}. This Figure was taken from [71].

of this facility is provided in [71]. The beam generation is based on the extraction of electrons or positrons from the DESY II synchrotron, which stores and accelerates a beam of electrons or positrons with energy up to 7 GeV in bunches with 10^{10} particles each. Each bunch is stored for 160 ms before being dumped, corresponding to two magnet cycles (see Figure A.1 that accelerate the particles from the injection energy $E_{min} = 0.45$ GeV to the typical maximum energy $E_{max} = 0.63$ GeV. Every few minutes, the beam is extracted to be employed in the PETRA III X-ray facility, leaving the DESY II synchrotron empty until the next injection.

A.1.1 Test Beam Areas

A double conversion from the DESY II primary beam generates the beam provided in the Test Beam areas at DESY. First, the electron or positron beam interacts with a carbon fiber target, producing bremsstrahlung photons. These photons then interact with a secondary target from which e^+-e^- pairs are emitted, as visible in Figure A.2, and travel in a high vacuum beam line until they reach a dipole magnet (or two, in the case of T24) employed to filter the neutral particles and to select the electrons (or positrons) momenta and charge, i.e. particle flavour. The beam then runs into a primary collimator unit composed of 100 mm thick tungsten jaws whose position can be controlled by the user and a beam shutter capable of switching off the beam, allowing access to the test beam area safely. Finally, the beam is delivered inside the different test beam areas: T21, T22 and T24. When needed, a secondary lead collimator with various insets can be placed on the beam direction to obtain different shapes and to reduce its transverse dimension further. A set of two scintillators 1x1 cm^2 scintillators act as beam monitors and allow the users to directly measure the particle rate.

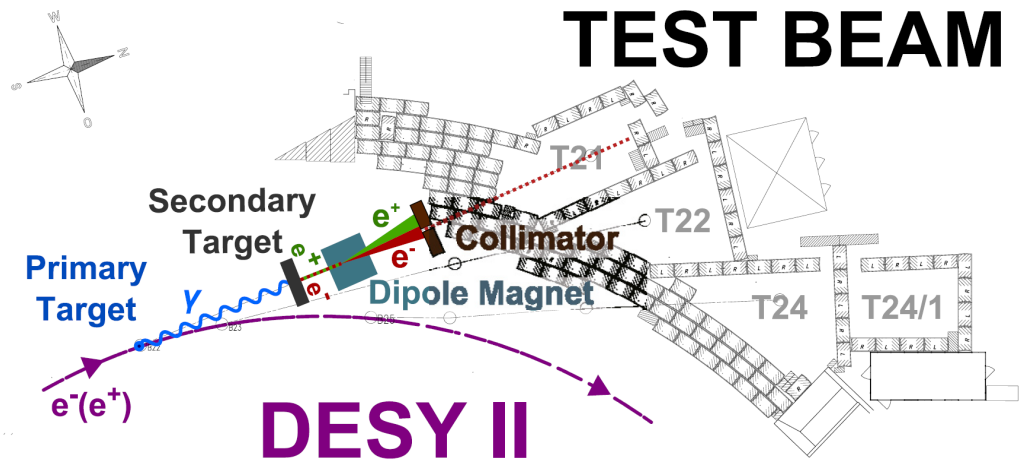

Figure A.2: Schematic representation of the beam generation at the DESY II Test Beam facility. The e^+-e^- particles interact with a primary target generating Bremsstrahlung photons that are converted again into e^+-e^- pairs. One or two dipole magnets (in the case of T21 and T22 or T24, respectively) select the desired momenta and charge of the beam arriving inside the Test Beam Area. The Figure was taken from [71].

Among the many utilities offered inside the test beam areas, the beam telescopes are indeed the most relevant for the RSD inquiry, capable of measuring the positions of the particles with great precision.

A.1.2 Beam Telescopes

Each DESY Test Beam Area is equipped with a silicon pixel telescope able to measure the hit position on the DUT with micrometre-level precision. The two permanently installed EUDET-type Pixel Beam Telescopes can be found in areas T21 and T22, while in T24, an ADENIUM Telescope is provided.

The EUDET telescopes were initially developed within the EUDET project [85] to combine an easy integration of the DUT, precise spatial resolution and suitable event rates [86]. Many EUDET telescopes are deployed worldwide in test beam facilities, such as CERN, SLAC, ELSA and DESY. The two EUDET-type telescopes deployed in the DESY II Test Beam Facility are called DATURA and DURANTA, installed in T21 and T22 respectively. Each telescope consists of two telescope sections composed of three MIMOSA26 monolithic active pixels planes. Each plane is composed of 1152x576 pixels with a pitch size equal to 18.4x18.4 μ^2, resulting in an active area of 21.2x10.6 mm^2 with 115.2 µs integration time. The MIMOSA26 sensors are 50 µm thick and are shielded from environmental light with a Kapton foil with 25 µm thickness on each side. The track resolution obtained with these devices varies with the beam energy, the plane spacing, and the DUT material budget. The best track resolution was estimated to be (1.83 ± 0.03) µm [86] using equidistant 20 mm spacing between the tracker sensors and a 5 GeV particles beam.

The ADENIUM telescope installed in the T24 area was developed under

the AIDA2020, and it consists of six planes of 25 µm-thick ALPIDE Monolithic Active Pixel Sensors (MAPS) [87]. Their good spatial resolution and low material budget are ideal for tracking particles at low momenta, such as the DESY II particle beams. Concerning the MIMOSA26, the ALPIDE sensors have a slightly larger pitch and worse spatial resolution, which are compensated by its larger active area, significantly shorter readout time ($\sim$ 10 µs) and their power-efficient design, resulting in a much simpler mechanical design. A telescope plane comprises a carrier board with the sensor glued and wire-bonded and an opening to minimize the material budget, a bridge board and the main readout board which interfaces with the acquisition system, As for the EUDET-type telescopes, the ADENIUM performances greatly depend on the planes relative positions, the beam energy and the DUT material budget. With a distance of 38 mm between the planes and a beam energy of 5.6 GeV, it was determined a resolution of $\sigma_x = 2.89$ µm and $\sigma_y = 2.84$ µm along the two coordinates.

Table A.1.2 reports the main characteristics of the two types of telescopes available at DESY.

	MIMOSA 26	ALPIDE
Sensor Size	21.2 x 10.6 mm^2	15 x 30 mm^2
Sensor Thickness	50 µm-70 µm	50 µm-70 µm
Pixel Pitch	18.4 x 18.4 µm^2	26.88 x 29.24 µm^2
Frame Readout Time	115.2 µs	10 µs
Detection Efficiency	>99%	>99%

A EUDET Trigger Logic Unit (TLU) [88] provides the trigger to the telescopes generated with four trigger scintillators in coincidence, two in front of the first telescope plane and two behind the last one, and adds timestamp information. The TLU and the DAQ of the telescope operate in a handshake mode so that when a trigger is raised by the TLU the telescope emits a busy signal during the frame readout time.

The data acquisition of all telescopes is performed in the EUDAQ framework, which merges data streams from all components. It is possible to integrate the DUT in the EUDAQ format or to extract valuable parameters from the framework and perform a parallel analysis (see Section 4.7).

Bibliography

[1] Frank Hartmann. *Evolution of Silicon Sensor Technology in Particle Physics*. eng. 2nd ed. 2017. Springer Tracts in Modern Physics, 275. Cham: Springer International Publishing, 2017. ISBN: 3-319-64436-X.

[2] A. Robson et al. "The Compact Linear e^+e^- Collider (CLIC): Accelerator and Detector". In: (2018). arXiv: 1812.07987.

[3] D. Dannheim et al. "Detector Technologies for CLIC". In: *CERN Yellow Reports: Monographs* (2018). DOI: 10.23731/CYRM-2019-001.

[4] M. Aleksa et al. "Calorimeters for the FCC-hh". In: *CERN-FCC-PHYS-2019-0003* (2019). arXiv: 1912.09962.

[5] L. Rossi and et al. "High Luminosity Large Hadron Collider (HL-LHC)". In: *CERN Yellow report 2015-005* (2017), pp. 1–19. DOI: 10.1016/j.phpro.2012.02.423.

[6] Adam W. et al. "Performance studies of the CMS Strip Tracker before installation". In: *JINST* 4 (2009). DOI: 10.1088/1748-0221/4/06/P06009.

[7] ECFA Detector R&D Roadmap Process Group. *The 2021 ECFA detector research and development roadmap*. Tech. rep. Geneva, 2020. DOI: 10.17181/CERN.XDPL.W2EX. URL: https://cds.cern.ch/record/2784893.

[8] N. Cartiglia et al. "4D Tracking: present status and perspectives". In: *Nuclear Instruments and Methods in Physics Research Section A: Accelerators, Spectrometers, Detectors and Associated Equipment* 1040 (2022), p. 167228. DOI: https://doi.org/10.1016/j.nima.2022.167228.

[9] J. Braach et al. "Performance of the FASTPIX Sub-Nanosecond CMOS Pixel Sensor Demonstrator". In: *Instruments* 6 (2022). DOI: https://doi.org/10.3390/instruments6010013.

[10] G. Iacobucci et al. "Efficiency and time resolution of monolithic silicon pixel detectors in SiGe BiCMOS technology". In: *Journal of Instrumentation* 17 (2020). DOI: https://doi.org/10.1088/1748-0221/17/02/P02019.

[11] G. Aglieri Rinella and et al. "The NA62 GigaTracKer: a low mass high intensity beam 4D tracker with 65 ps time resolution on tracks". In: *Journal of Instrumentation* 14.07 (July 2019), P07010–P07010. DOI: 10.1088/1748-0221/14/07/p07010. URL: https://doi.org/10.1088/1748-0221/14/07/p07010.

[12] J. Lange and et al. "Radiation hardness of small-pitch 3D pixel sensors up to a fluence of 3[16]". In: *J. Instrum.* 13 (2018), P09009. DOI: 10.1088/1748-0221/13/09/P09009.

[13] S.I. Parker, C.J. Kenney, and J. Segal. "3D – A proposed new architecture for solid-state radiation detectors". In: *Nucl. Inst. Meth. A* 395 (1997), p. 328. DOI: 10.1016/S0168-9002(97)00694-3.

[14] G. Pellegrini and et al. "Technology developments and first measurements of Low Gain Avalanche Detectors (LGAD) for high energy physics applications". In: *Nucl. Inst. Meth. A* 765 (2014), p. 12.

[15] G. Iacobucci and et al. "Efficiency and time resolution of monolithic silicon pixel detectors in SiGe BiCMOS technology". In: *Journal of Instrumentation* 17.02 (Feb. 2022), P02019. DOI: 10.1088/1748-0221/17/02/p02019. URL: https://doi.org/10.1088/1748-0221/17/02/p02019.

[16] C. Agapopoulou and et al. "ALTIROC 1, a 25 ps time resolution ASIC for the ATLAS High Granularity Timing Detector". In: *2020 IEEE Nuclear Science Symposium and Medical Imaging Conference (NSS/MIC)*. 2020, pp. 1–4. DOI: 10.1109/NSS/MIC42677.2020.9507972.

[17] T. Liu and et al. ""The ETROC Project: Precision Timing ASIC Development for LGAD-based CMS Endcap Timing Layer (ETL) Upgrade"". In: *TWEPP 2019 Topical Workshop on Electronics for Particle Physics*. 2019. URL: https://indico.cern.ch/event/799025/contributions/3486223/attachments/1902297/3140606/ETROC-TWEPP-2019-poster-final.pdf.

[18] G. Paternoster and et al. "Trench-Isolated Low Gain Avalanche Diodes (TI-LGADs)". In: *IEEE Electr. Device L.* 41.6 (2020), p. 884. DOI: 10.1109/LED.2020.2991351.

[19] M. Senger and et al. "Time and space characterization of novel TI-LGAD structures". In: *VCI2022 conference*. 2022. URL: https://indico.cern.ch/event/1044975/contributions/4663649/.

[20] M. Ferrero and et al. "Characterization of Trench-Isolated LGADs before and after irradiation". In: *17th TREDI conference*. 2022. URL: https://indico.cern.ch/event/1096847/contributions/4742364/.

[21] B. Schmidt. "The High-Luminosity upgrade of the LHC:Physics and Technology Challenges for the Accelerator and the Experiments". In: *Journal of Physics: Conference Series* (2016).

[22] F. Siviero. "The Endcap Timing Layer of the CMS experiment: detector development and impact on physics analyses". PhD thesis. Universit degli Studi di Torino, 2022.

[23] CMS Collaboration. "A MIP Timing Detector for the CMS Phase-2 Upgrade". In: *Technical Design Report, CERN-LHCC-2019-003, CMS-TDR-020* (2019).

[24] CMS Collaboration. "Particle-flow reconstruction and global event description with the CMS detector". In: *J. Instrum.* 12.10 (2017), P10003–P10003. DOI: 10.1088/1748-0221/12/10/p10003.

[25] D. Bertolini et al. "Pileup per particle identification". In: *JHEP* 2014.10 (Oct. 2014). DOI: 10.1007/jhep10(2014)059.

[26] S Gundacker et al. "Time of flight positron emission tomography towards 100ps resolution with L(Y)SO: an experimental and theoretical analysis". In: *J. Instrum.* 8.07 (2013), P07014–P07014. DOI: 10.1088/1748-0221/8/07/p07014.

[27] T. Croci et al. "TCAD simulations of non-irradiated and irradiated low-gain avalanche diodes and comparison with measurements". In: *Journal of Instrumentation* 17 (Jan. 2022), p. C01022. DOI: 10.1088/1748-0221/17/01/C01022.

[28] V. Sola et al. "A compensated design of the LGAD gain layer". In: *Nuclear Instruments and Methods in Physics Research Section A: Accelerators, Spectrometers, Detectors and Associated Equipment* 1040 (2022), p. 167232. ISSN: 0168-9002. DOI: https://doi.org/10.1016/j.nima.2022.167232.

[29] H. Bethe and W. Heitler. "On the stopping of fast particles and on the creation of positive electrons". In: *Proc. Royal Soc. London* 146.856 (1934), p. 83. DOI: 10.1098/rspa.1934.0140. URL: https://doi.org/10.1098/rspa.1934.0140.

[30] W. Shockley and W.T. Read, Jr. "Statistics of the recombinations of holes and electrons". In: *Phys. Rev.* 87.5 (1952), pp. 835–842. DOI: 10.1103/PhysRev.87.835.

[31] S. Ramo. "Currents Induced by Electron Motion". In: *IEEE Proceedings of the IRE* 27.9 (1939), p. 584. DOI: 10.1109/JRPROC.1939.228757.

[32] C. Jacoboni et al. "A review of some charge transport properties of silicon". In: *Solid-State Electron.* 20.2 (1977), pp. 77–89. ISSN: 0038-1101. DOI: https://doi.org/10.1016/0038-1101(77)90054-5. URL: http://www.sciencedirect.com/science/article/pii/0038110177900545.

[33] W. Maes, K. De Meyer, and R. Van Overstraeten. "Impact ionization in silicon: A review and update". In: *Solid State Electron.* 33 (1999), p. 705.

[34] F. Cenna and et al. "Weightfield2: A fast simulator for silicon and diamond solid state detector". In: *Nucl. Inst. Meth. A* 796 (2015), p. 149. DOI: https://doi.org/10.1016/j.nima.2015.04.015.

[35] N. Cartiglia and et al. "Issues in the design of Ultra-Fast Silicon Detectors". In: *TREDI2015: 10th "Trento" Workshop on Advanced Silicon Radiation Detectors*. 2015. URL: https://indico.cern.ch/event/351695/contributions/828366.

[36] G. Giacomini and et al. "Development of a technology for the fabrication of Low-Gain Avalanche Diodes at BNL". In: *Nucl. Inst. Meth. A* 934 (2019), p. 52. DOI: 10.1016/j.nima.2019.04.073.

[37] C. De La Taille and et al. "ALTIROC0, a 20 pico-second time resolution ASIC for the ATLAS High Granularity Timing Detector (HGTD)". In: *PoS Proc. Sci.* TWEPP-17 (2018), p. 006. DOI: 10.22323/1.313.0006.

[38] A. Vasilescu and G. Lindström. *Displacement damage in silicon, online compilation*. https://rd50.web.cern.ch/NIEL/. 2000.

[39] M. Ferrero and et al. *An Introduction to Ultra-Fast Silicon Detectors*. CRC Press, 2021. DOI: 10.1201/9781003131946.

[40] M. Mandurrino and et al. "TCAD simulation of silicon detectors: A validation tool for the development of LGAD". In: *30th RD50 Workshop*. 2017. URL: https://indico.cern.ch/event/637212/contributions/2608617/.

[41] *LTspice official website*. URL: http://www.linear.com/LTspice.

[42] M. Mandurrino and et al. "Analysis and numerical design of Resistive AC-Coupled Silicon Detectors (RSD) for 4D particle tracking". In: *Nucl. Inst. Meth. A* 959 (2020), p. 163479. DOI: https://doi.org/10.1016/j.nima.2020.163479.

[43] RD53 Collaboration. "RD Collaboration Proposal: Development of pixel readout integrated circuit for extreme rate and radiation". In: *CERN-LHCC-2013-008, LHCC-P-006* (2013). URL: http://cds.cern.ch/record/1553467.

[44] M. Mandurrino and et al. *High performance picosecond- and micron-level 4D particle tracking with 100% fill-factor Resistive AC-Coupled Silicon Detectors (RSD)*. 2020. arXiv: 2003.04838 [physics.ins-det].

[45] M. Tornago and et al. "Resistive AC-Coupled Silicon Detectors: principles of operation and first results from a combined analysis of beam test and laser data". In: *Nucl. Inst. Meth. A* 1003 (2021). arXiv: 2007.09528, p. 165319. ISSN: 0168-9002. DOI: https://doi.org/10.1016/j.nima.2021.165319. URL: https://www.sciencedirect.com/science/article/pii/S016890022100303X.

[46] M. Mandurrino and et al. "Demonstration of 200-, 100-, and 50- μm Pitch Resistive AC-Coupled Silicon Detectors (RSD) With 100% Fill-Factor for 4D Particle Tracking". In: *IEEE Electr. Device L.* 40.11 (2019), p. 1780. DOI: 10.1109/LED.2019.2943242.

[47] F. Siviero and et al. "First application of machine learning algorithms to the position reconstruction in Resistive Silicon Detectors". In: *Journal of Instrumentation* 16.03 (Mar. 2021), P03019. DOI: 10.1088/1748-0221/16/03/p03019. URL: https://doi.org/10.1088/1748-0221/16/03/p03019.

[48] R. Heller. *The Fermilab Test Beam Silicon Telescope upgrade*. 2022. URL: https://indico.cern.ch/event/1058977/contributions/4865292/.

[49] A. Apresyan and et al. "Measurements of an AC-LGAD strip sensor with a 120 GeV proton beam". In: *J. Instrum.* 15 (Sept. 2020), P09038.

[50] M. Tornago et al. "Silicon sensors with resistive read-out: Machine Learning techniques for ultimate spatial resolution". In: *Nuclear Instruments and Methods in Physics Research Section A: Accelerators, Spectrometers, Detectors and Associated Equipment* 1047 (2023), p. 167816. DOI: https://doi.org/10.1016/j.nima.2022.167816.

[51] *Multi-Output Regressor*. URL: https://scikit-learn.org/stable/modules/generatedsklearn.multioutput.MultiOutputRegressor.html.

[52] J. H. Friedman. "Greedy Function Approximation: A Gradient Boosting Machine". In: *The Annals of Statistics* 29 (2001), pp. 1189–1232.

[53] M. Mandurrino and et al. *The second production of RSD (AC-LGAD) at FBK*. 2021. DOI: 10.48550/ARXIV.2111.14235. URL: https://arxiv.org/abs/2111.14235.

[54] G. Kramberger. "Advanced Transient Current Technique Systems". In: *Proceedings of Science (Vertex2014* 032 (2014). DOI: 10.22323/1.227.0032..

[55] http://particulars.si.

[56] *Teledyne LeCroy HDO940 specifications*. URL: https://teledynelecroy.com/oscilloscope/waverunner-9000-oscilloscopes/waverunner-9404.

[57] *CAEN DT1471LET HV supply specifications*. URL: https://www.caen.it/products/dt1471et/.

[58] V. Sola et al. *Observation characterisation of the charge screening effect in LGAD*. 2022. URL: https://indico.cern.ch/event/1157463/contributions/4922792/attachments/2468102/4233730/vs-Qscreening-40thRD50.pdf.

[59] ROOT, Data Analysis Framework. https://root.cern.ch.

[60] E. Curras. *Gain suppression mechanism observed in Low Gain Avalanche Detectors*. 2022. URL: https://indico.cern.ch/event/983068/contributions/4223231/.

[61] *CAEN DT5742 16+1 channels Digitizer specifications*. URL: https://www.caen.it/products/dt5742/.

[62] *UFSD_DigiDAQ*. F. Miserocchi is the original author of the suite, but its github branch is now deprecated. URL: https://github.com/LucaMenzio/UFSD_DigiDAQ.

[63] *CAEN WaveDump digitizer readout application manuals*. URL: https://www.caen.it/products/caen-wavedump/.

[64] Jonathan Bortfeldt et al. "Timing performance of a Micro-Channel-Plate Photomultiplier Tube". In: *Nuclear Instruments and Methods in Physics Research Section A Accelerators Spectrometers Detectors and Associated Equipment* 960 (Apr. 2020), p. 5. DOI: 10.1016/j.nima.2020.163592.

[65] *Corrivreckan gitlab project page*. Accessed on April 2023. 2023. URL: https://gitlab.cern.ch/corryvreckan/corryvreckan.

[66] H. Wagner et al. "On the dynamic two-dimensional charge diffusion of the interpolating readout structure employed in the MicroCAT detector". In: *NIM A* 482 (2002). DOI: 10.1016/S0168-9002(01)01368-7.

[67] H.F.-W. Sadrozinski, A. Seiden, and N. Cartiglia. "4D Tracking with Ultra-Fast Silicon Detectors". In: *Rep. Prog. Phys.* 81 (2017), p. 026101. DOI: 10.1088/1361-6633/aa94d3.

[68] R. Arcidiacono and et al. "High-Precision 4D Tracking with Large Pixels using Thin Resistive Silicon Detectors". In: *Nucl. Inst. Meth. A* 978 (Nov. 2022). DOI: 10.48550/arXiv.2211.13809.

[69] S. Siegel et al. "Simple charge division readouts for imaging scintillator arrays using a multi-channel PMT". In: *IEEE Transactions on Nuclear Science* 43.3 (1996), pp. 1634–1641. DOI: 10.1109/23.507162.

[70] F. Siviero and et al. "First experimental results of the spatial resolution of RSD pad arrays read-out with a 16-ch board". In: *VCI2022 conference*. 2022. URL: https://indico.cern.ch/event/1044975/contributions/4663645/.

[71] R. Diener et al. "The DESY II test beam facility". In: *Nuclear Instruments and Methods in Physics Research Section A: Accelerators, Spectrometers, Detectors and Associated Equipment* 922 (2019), pp. 265–286. ISSN: 0168-9002. DOI: https://doi.org/10.1016/j.nima.2018.11.133.

[72] Dominik Dannheim et al. "Corryvreckan: A Modular 4D Track Reconstruction and Analysis Software for Test Beam Data". In: *JINST* 16.03 (2021), P03008. DOI: 10.1088/1748-0221/16/03/P03008. arXiv: 2011.12730 [physics.ins-det].

[73] Yi Liu et al. *ADENIUM – A demonstrator for a next-generation beam telescope at DESY*. 2023. arXiv: 2301.05909 [physics.ins-det].

[74] *Error function in ROOT*. Accessed on April 2023. URL: https://root.cern.ch/doc/v608/group__SpecFunc.html.

[75] F. Cenna. "Design and Test of Sensors and Front-End Electronics for Fast Timing in High Energy Physics". PhD thesis. Università degli Studi di Torino, 2018.

[76] F. Siviero and et al. "Optimization of the Gain Layer Design of Ultra-Fast Silicon Detectors". In: *https://arxiv.org/abs/2112.00561.* (2022). DOI: 10.48550/arXiv.2112.00561.

[77] N. Cartiglia et al. *Spatial and temporal resolutions of sensors belonging to the second FBK RSD production*. 2022. URL: https://indico.cern.ch/event/1096847/contributions/4742361/.

[78] L. Menzio. *DC-coupled resistive silicon detectors for 4-D tracking*. 2022. URL: https://indico.cern.ch/event/1096847/contributions/4743695/.

[79] T. Croci et al. "Development and test of innovative Low-Gain Avalanche Diodes for particle tracking in 4 dimensions". In: *Nuclear Instruments and Methods in Physics Research Section A: Accelerators, Spectrometers, Detectors and Associated Equipment* 1047 (2023), p. 167815. ISSN: 0168-9002. DOI: https://doi.org/10.1016/j.nima.2022.167815.

[80] Hao Yu. "Advanced Metal Semiconductor Contacts for 14nm CMOS Technology and Beyond". PhD thesis. Sept. 2019.

[81] "Dual-Function Electron-Conductive, Hole-Blocking Titanium Nitride Contacts for Efficient Silicon Solar Cells". In: *Joule* 3.5 (2019), pp. 1314–1327. ISSN: 2542-4351. DOI: https://doi.org/10.1016/j.joule.2019.03.008.

[82] Kikuo Tominaga, Hideaki Adachi, and Kiyotaka Wasa. "6 - Functional Thin Films". In: *Handbook of Sputtering Technology (Second Edition)*. Ed. by Kiyotaka Wasa, Isaku Kanno, and Hidetoshi Kotera. Second Edition. Oxford: William Andrew Publishing, 2012, pp. 361–520. ISBN: 978-1-4377-3483-6. DOI: https://doi.org/10.1016/B978-1-4377-3483-6.00006-1.

[83] R.S. Okojie et al. "Electrical characterization of annealed Ti/TiN/Pt contacts on N-type 6H-SiC epilayer". In: *IEEE Transactions on Electron Devices* 46.2 (1999), pp. 269–274. DOI: 10.1109/16.740888.

[84] J Hu et al. "Electrical properties of Ti/TiN films prepared by chemical vapor deposition and their applications in submicron structures as contact and barrier materials". In: *Thin Solid Films* 308-309 (1997), pp. 589–593. ISSN: 0040-6090. DOI: https://doi.org/10.1016/S0040-6090(97)00477-X.

[85] *Homepage of the EUDET project*. 2023. URL: https://www.eudet.org/.

[86] Hendrik Jansen et al. "Performance of the EUDET-type beam telescopes". In: *EPJ Techniques and Instrumentation* 3 (Mar. 2016). DOI: 10.1140/epjti/s40485-016-0033-2.

[87] M. Mager. "ALPIDE, the Monolithic Active Pixel Sensor for the ALICE ITS upgrade". In: *Nuclear Instruments and Methods in Physics Research Section A: Accelerators, Spectrometers, Detectors and Associated Equipment* 824 (2016). Frontier Detectors for Frontier Physics: Proceedings of the 13th Pisa Meeting on Advanced Detectors, pp. 434–438. ISSN: 0168-9002. DOI: https://doi.org/10.1016/j.nima.2015.09.057.

[88] David Cussans. "Description of the JRA1 Trigger Logic Unit (TLU), v0.2c". In: 2009.

List of Figures